IMPROVING CAPABILITIES OF PORE-SCALE MODELING OF MULTIPHASE FLOW FOR GEOLOGICAL STORAGE OF CO_2

BY

AMIR HOSSEIN KOHANPUR

DISSERTATION

Submitted in partial fulfillment of the requirements
for the degree of Doctor of Philosophy in Civil Engineering
in the Graduate College of the
University of Illinois at Urbana-Champaign, 2020

Urbana, Illinois

Doctoral Committee:

Professor Albert Valocchi, Chair and Director of Research
Professor Charles Werth
Assistant Professor Jennifer Druhan
Assistant Professor Roman Makhnenko
Assistant Professor Pejman Tahmasebi, University of Wyoming

Abstract

This dissertation presents a computational modeling framework to address current challenges in pore-scale modeling of two-phase flow with applications to sequestration of carbon dioxide (CO_2) in deep saline geological formations. These formations are widely available and have relatively high storage capacity to host injected CO_2 for long-term as a practical solution to reduce CO_2 emissions from power plants. Due to the expense and complexity of experimental investigations, computational approaches have been developed to understand the physics of CO_2-brine flow at the pore-scale. The dissertation considers both direct numerical simulation on real rock geometry measured by X-ray micro-CT scans, as well as pore-network (PN) models which simplify the pore space into interconnected idealized shapes. Both approaches are challenged in applications to large heterogeneous cores.

A heterogeneous Mt. Simon sandstone sample is characterized in terms of morphology and CO_2-brine flow properties. 3D rock images are investigated to assess the REV size and heterogeneity. Three distinct simulation approaches are applied to simulate the displacement of brine by CO_2: PN modeling on the extracted network, and the lattice-Boltzmann (LB) method and the finite-volume method using OpenFOAM (OF) on the rock geometry. The relative permeabilities are computed and compared using different measurement choices: the steady-state approach for LB, unsteady approach for OF, and quasi-static approach for PN. All approaches are in close agreement with one another. The accuracy, computational efficiency, and the effect of grid resolution are also compared. A novel pore-network stitching method (PNSM) is developed that combines the inherent simplicity of PN modeling with statistical network generation to characterize the heterogeneity of cores. The method overcomes technical limits on sample size during X-ray scanning and computational limits on network extraction algorithms. The workflow is validated on various types of rock samples and applied on large

domain problems based on pore structure and CO_2-brine flow properties. In each sample, multiple realizations are generated and the average results are compared with properties from defined reference PNs. A new set of pore-level flow models in PN modeling are proposed to improve the prediction of residual trapping of CO_2. This is important for assessing the long-term storage capacity and safety of geological sequestration. LB simulations are carried out on several PN configurations to investigate pore-body filling and snap-off events that are simplified in PN modeling. The threshold local capillary pressure is evaluated and modified equations are defined. The modified model is incorporated into a quasi-static PN solver and applied to Berea and Mt. Simon sandstone samples to obtain relative permeabilities and residual trapping of CO_2 after a drainage-imbibition cycle. The modified model predicts residual trapped CO_2 closer to experimental data than the conventional model.

These studies together enable the current generation of PN models to be more accurate and applicable in practice. The PNSM enables study of large heterogeneous cores. The use of direct numerical simulation to study multiphase flow physics in PN configurations enables modification of rules implemented in PN models to improve accuracy of predicted residual trapped CO_2.

To my parents, Mahin & Mohammad Reza.
For their unconditional love and support.

Acknowledgments

First and foremost, I would like to express my sincere gratitude to my esteemed advisor Prof. Albert Valocchi for giving me the opportunity to work with him, for the continuous support of my study and research, and for his patience, motivation, and immense knowledge. His guidance helped me in all the time of research and writing of this dissertation.

Besides my advisor, I would like to thank the rest of my dissertation committee: Prof. Charles Werth, Prof. Jennifer Druhan, Prof. Roman Makhnenko, and Prof. Pejman Tahmasebi for their insightful comments and encouragement which incented me to widen my research from various perspectives.

I greatly appreciate the guidance from and interaction with our former post-doctoral researchers in the UIUC, Dr. Yu Chen and Dr. Arash Aghaei. They shared their knowledge and experience with me, and I learned a lot from them during this project.

I would like to extend my appreciation to my collaborators, Dr. Mahsa Rahromostaqim and Prof. Muhammad Sahimi, at the USC for their contributions to the effort for my research. It was a pleasure to work with them on this project.

I was lucky to be in touch with great colleagues in different institutions during my research. I thank them all for their generous support and contribution: Dr. Dustin Crandall, Laura Dalton, and John Tudek from NETL, Prof. Edward Mehnert and Dr. Jared Freiburg from ISGS, and Prof. Dorthe Wildenschild and Dr. Anna Herring from OSU.

Above all, I would like to thank my lovely family, my parents and sister and brothers, for their love, encouragement, and support throughout my life.

The financial support was primarily provided by the Center for Geologic Storage of CO_2, an Energy Frontier Research Center funded by the U.S. Department of Energy under Award number DE-SC0C12504. The research was also supported by the International Institute for Carbon-Neutral Energy Research (WPI- I^2CNER) based at Kyushu University, Japan.

Table of Contents

Chapter 1

Prologue

1.1 Introduction

Physics of two-phase flows in porous media plays an important role in many applications such as carbon dioxide (CO_2) sequestration in deep saline reservoirs, recovery of oil from hydrocarbon reservoirs, transport of non-aqueous phase liquid contaminants, and water infiltration into soil. Understanding the underlying physics at different length scales is vital to deal with current societal needs and issues in managing water resources, providing energy, and combating climate change.

The ongoing increase of anthropogenic CO_2 emission in the atmosphere has played a major role in climate change (Friedlingstein and Solomon 2005; Metz et al. 2005; Nordbotten and Celia 2011). The main source of this atmospheric CO_2 is combustion of fossil fuels to generate electricity in thermal power plants. A practical solution among available technologies to mitigate the CO_2 emission is CO_2 capture and storage (CCS). The process of CCS is associated with separation and compression of CO_2 from energy industries, transporting it to storage locations, and keeping it isolated for a very long-term period. Captured CO_2 can be stored in large onshore and offshore geological formations such as depleted hydrocarbon reservoirs and deep saline geological formations (Metz et al. 2005).

1.1.1 Geological storage of carbon dioxide

A comprehensive study of geological storage of CO_2 should encompass economic feasibility, site selection, risk assessment, environmental impact, safety aspects, monitoring and verification, in addition to perspectives on retention time, physical leakage, brine displacement, and microseismicity (Metz

et al. 2005). Deep saline formations are widely available and have relatively high storage capacity, so they are important target reservoirs to study in more depth. As an example, up to 65% of the CO_2 produced in power plant of the United States can be injected into deep saline aquifers (Shukla et al. 2010). When captured and compressed CO_2 enters a reservoir saturated with brine, the interaction of these fluids with each other and the host rock at different scales (molecular-scale, pore-scale, continuum-scale, and field-scale) controls the long-term behavior of the system, specifically the fate and distribution of CO_2 plume.

During the active injection period, the supercritical CO_2 displaces the native brine phase, i.e., drainage process while imbibition of brine into CO_2 plume occurs in post injection period. In general, this system can be studied from chemical, mechanical, hydrogeological, and petrophysical points of view where each of those requires specific governing equations and constitutive equations. For instance, the continuum-scale CO_2-brine flow can be modeled with Darcy's law and mass balance for each phase as governing equations along with macroscopic capillary pressure and relative permeability characteristic curves as constitutive relations (Celia et al. 1995).

1.1.2 Pore-scale modeling of two-phase flow

The physics of two-phase flow of CO_2-brine system in natural rocks at the scale of pores controls fundamental behavior of flow and transport. Analytical, experimental, and computational approaches can be used in pore-scale modeling. Analytical solutions are usually limited to simplified problems and conditions. While experimental approaches can be more realistic, they are usually difficult to implement, time-consuming, expensive, and have uncertainties in measurements (Joekar-Niasar and Hassanizadeh 2012). Computational approaches are generally less expensive than experiments and have more flexibility in implementation and adjusting parameters. Advances in modeling of flow in porous media, as well as development of efficient computer simulation, together with increasing computer power, have made it possible to model flow at core-scale and even larger length scales. In addition, numerical simulation of flow at field-scale requires inputs such as the relative permeability and capillary pressure curves at the scale of the grid

blocks, which can be obtained by pore-scale modeling (Celia et al. 1995). Pore-scale processes and geometry of pore structure determine the continuum scale constitutive curves which affect significantly the characteristics of the process at larger scales, including injection and storage of CO_2 in large-scale rock formations (Juanes et al. 2006; Pruess and Garcia 2002).

With recent advances in instrumentation and X-ray computed tomography (CT) imaging, one can directly obtain detailed three-dimensional (3D) geometry of rock and its pore structure with high resolution images (Flannery et al. 1987; Dunsmuir et al. 1991; Wildenschild and Sheppard 2013; Andrä et al. 2013a; Andrä et al. 2013b). Such images are inputs of pore-scale models which can be categorized as either direct or simplified models, based on the manner in which they represent the geometry of the void space of porous media. In direct models, flow and transport equations are solved directly on the exact geometry of pore space obtained from the CT images. Some examples of direct numerical simulation (DNS) methods are lattice-Boltzmann (LB) methods (Boek and Venturoli 2010; Ramstad et al. 2012) and finite-volume (FV) methods (Ferrari and Lunati 2013; Raeini et al. 2014). The main challenge in using DNS methods is computational costs due to limitations on the size of the domain that is relevant to the grids resolution of simulation.

On the other hand, a popular simplified model is pore-network (PN) modeling (Fatt et al. 1956; Sahimi 2011; Blunt 2017) which simplifies the pore space by dividing it into two categories of pore elements: pore-bodies (larger pores for storage of fluids) and pore-throats (narrower channels for flow of fluids). A PN can be either generated from statistics of the pore space or extracted directly from the 3D image of rock where irregular surfaces and edges of the pore space are abstracted down to simpler geometrical units. There are different PN extraction algorithms in the literature such as medial axis (Lindquist et al. 1996), watershed (Gostick 2017), and maximal ball (MB) algorithms (Silin and Patzek 2006;Dong and Blunt 2009). Defining a PN requires geometrical (location, size, and shape of pore elements) and topological (connections between pore elements) information of the pore space.

PN flow models then use some assumptions and approximations to the governing equations on the entire PN, e.g., Hagen-Poiseuille equation for flow in pore-throats. These flow models are generally classified further as quasi-static and dynamic models. Quasi-static models predict static positions of

interfaces at equilibrium states by imposing capillary pressure, but do not involve viscous and gravity forces, so they are limited to capillary dominated systems (Valvatne and Blunt 2004). Dynamic models predict dynamic effects by imposing flow rate and includes capillary, viscous, and gravity forces, but they are more complicated to implement and computationally expensive (Joekar-Niasar and Hassanizadeh 2012).

Such approximations to geometry and physics make PN models more capable of simulating a representative elementary volume (REV) of porous medium with less computational effort compare to DNS methods to predict macroscopic properties. Therefore, they can provide characteristic curves such as relative permeability, capillary pressure, residual trapping, and hysteretic curves which are important in CCS. As an example, a quasi-static PN modeling of CO_2-brine flow can be initialized with the PN fully saturated with brine. By incremental increase of macroscopic capillary pressure, CO_2 invades pore elements gradually based on increasing threshold local capillary pressure. This cycle continues until stopped or no more CO_2 can occupy pore elements and is called drainage cycle since the wetting phase saturation is decreasing. On the hand, imbibition cycle is when the wetting phase saturation is increasing in the porous medium. Since imbibition cycle follows drainage cycle, the end point of drainage cycle is the start point of imbibition cycle. The end point of imbibition cycle is when all CO_2 in the the porous medium is trapped or immobile which is called residual trapped CO_2.

1.1.3 Heterogeneity and size

Although PN modeling based on CT images has been applied to different types of porous media, it has been mainly applied on a relatively small volume of an entire core. Current tools face important limitations for attaining a large representative PN of heterogeneous domains. There are both (1) technical limits and (2) computational limits:

- Technical limits: There are technical limits on the size of the core that can be scanned to discern void space well. This is rooted in the trade-off of size and resolution and reflected in both the scanning time and size of produced images (Bultreys et al. 2015). For instance, typical sandstones require few microns (about 2–5 μm) of resolution in CT

images to be used in pore-scale modeling while typical scans are not larger than $1000^3 - 2000^3$ voxels with the current micro-CT scanners (Blunt 2017).

- Computational limits: Current PN extraction algorithms are not computationally able to provide a large PN covering all heterogeneities at the core-scale. These algorithms generally scan the entire voxelized pore space and the current codes are written as serial codes. Therefore, their performance is limited in terms of both computational memory and speed that results a limit on the size of their input. For example, current MB network extraction codes cannot attain PNs beyond sizes more than roughly $1500^3 - 2000^3$ voxels.

There are different studies that have addressed some of the challenges noted above by different strategies including multiscale frameworks and domain decomposition approaches in addition to exploiting growing computational capabilities in using current tools.

One common motivation in conducting multiscale studies comes from the practice of investigation of core-scale images (resolution of about 10–30 μm) of different heterogeneous rocks in terms of spatial variability that shows a wide range of heterogeneities. While such images can reveal some details of the rock such as connectivity of larger pores, they cannot be directly used in pore-scale modeling tools due to lack of enough precision and failure in capturing small channels and pores which are below the resolution scale. However, these images are still able to cover a large domain of the core thereby allowing study of the heterogeneity and spatial variation of the rock properties. They can be used along with pore-scale images in a multiscale framework to study rock heterogeneity, as has been addressed in some studies to be demonstrated below.

Chu et al. (2013) developed a multiscale method with the form of heterogeneous multiscale method that couples PN models with continuum models to predict pressure and track the macroscopic front, although their work was limited to simpler PN models. In a PN study, Jiang et al. (2013) combined coarse-scale and fine-scale pore elements to develop a multiscale PN by stochastic generator. This work could cover three-level PNs from different resolutions but mainly addressed micropores. In another multiscale work, Bultreys et al. (2015) developed a dual PN model that incorporates

microporosity via adding micro-links to traditional PN models to address the small-scale heterogeneities. While their approach results a great number of pore elements in the constructed PN, it was mainly designed for modeling micropores of heterogeneous samples.

Some other studies have bridged pore-scale models to core-scale in order to incorporate heterogeneities. In a pore-to-core PN modeling work, Aghaei and Piri (2015) studied a long Berea sandstone core to attain a large PN and modeled capillary and viscosity effects with the aid of parallel computing. This work was notable in terms of the prediction of two-phase flow properties and the size of studied sample, but the type of rock was relatively homogeneous and the process of connecting sample pieces was sample specific. In a recent pore-to-core PN modeling study, Zahasky et al. (2019) characterized centimeter-scale Bentheimer sandstone cores by studying heterogeneity in capillary pressure and relative permeability with the aid of an extensive multiple resolution imaging. In addition, Jackson et al. (2019) used multi-scale experimental and modeling approaches to study two large Bentheimer sandstone cores. Although both works were notable in terms of addressing heterogeneity and size of the domain, they rely on full micro-CT images of an entire core with a fine resolution which may not always be readily available.

Therefore, there is still a need for pore-to-core upscaling approaches that can accurately represent the 3D complex pore structure and heterogeneity of real media with efficient computational tools and incorporate information from multiple scales.

1.1.4 Residual trapping

Trapping of non-wetting phase as residual saturation is an important feature in two-phase flow through natural rocks. In a CO_2-brine flow system, the CO_2 can be trapped by four main mechanisms: physical (stratigraphic and structural), solubility, mineral, and residual trapping (Andrew et al. 2014). These mechanisms can occur simultaneously but with different time scales. Mineral precipitation usually has the longest time scale followed by residual trapping and dissolution, respectively. On the other hand, physical trapping has the shortest time scale (Metz et al. 2005). Residual trapping is mainly due to capillary forces and interface movement, i.e., capillary trapping. The

majority of trapping happens when brine is invading the pore space after the initial CO_2 injection, i.e., imbibition process due to migration of the CO_2 plume or injection of chase brine (Qi et al. 2009; Gershenzon et al. 2017). Thus, in addition to capillary pressure and relative permeability curves, one is also interested in predicting residual trapped CO_2 at the end of drainage-imbibition cycle in pore-scale modeling of CO_2-brine flow.

There are several studies in the literature that focus on the amount of residual trapped CO_2 and end points in drainage and imbibition processes using experimental or computational methodologies. Land et al. (1968) introduced an empirical relation of residual trapping of non-wetting phase of a two-phase flow system that relates initial and residual saturations known as Land's initial-residual trapping model. Andrew et al. (2014) studied various natural rocks by core flooding experiments and reported that significant amount of CO_2 can be stored by capillary trapping. As an example, they found about 30% CO_2 residual saturation on two sandstone samples at the end of imbibition cycle. Levine et al. (2014) conducted experiment of CO_2 injection into brine-saturated synthetic and natural porous media to measure drainage end point relative permeability and saturation. Most of reported saturation values of this study were in range $S_{nw} = 0.60 - 0.70$ for drainage end point. Perrin and Benson (2010) measured relative permeabilities of CO_2 and brine on a heterogeneous core from an actual storage reservoir and obtained a drainage end point of $S_{nw} = 0.56$. Jiang and Tsuji (2015) studied the effect of interfacial tension on residual CO_2 clusters using LB simulation on a sandstone and characterized residual CO_2 cluster distribution.

Although conventional quasi-static PN modeling has been used in some CO_2-brine flow studies, e.g., by Rasmusson et al. (2018), it is mainly developed and used based on oil-water flow systems and its properties during drainage process. It can fail to capture the residual trapping of CO_2 after imbibition, especially when no drainage end point information is available. As an example, quasi-static PN simulations using Valvatne and Blunt (2004) flow solver on a Mt. Simon sandstone sample from a pilot CO_2 injection site shows approximately 70% trapped CO_2 at the end of drainage-imbibition cycle, which is far greater than typical counterpart experimental and DNS results on sandstones (about 30–40%) in the literature. Since the residual trapping is mainly due to capillary forces and interface movement, the source of inaccuracies is in the defined pore-level flow rules and pre-solved equations

of imbibition events of PN modeling that describe the interface shape and movement prior trapping.

Thus, there is a need to improve current imbibition pore-level flow models of CO_2-brine flow for better understanding and predicting residual trapping of CO_2 and other resulting properties such as relative permeabilities.

1.2 Research objectives

The aim of this dissertation is use of different approaches of pore-scale modeling and improve capabilities of current PN modeling from three perspectives to address challenges in modeling of CO_2-brine flow through heterogeneous rocks used in CCS:

- There are different computational approaches in pore-scale modeling but mostly applied to oil-water flow system on homogeneous rock samples and without a comprehensive REV analysis in the literature. These computational approaches can be applied on CT scans of heterogeneous rock samples from CO_2 storage sites that are noteworthy of being studied and characterized. A comparative and extensive analysis is conducted to characterize the rock images and implemented CO_2-brine flow simulation to obtain relative permeabilities (Chapter 2).

- The challenge of existing multiscale heterogeneity in cores coming from storage sites in addition to limitations on current CT imaging technologies and PN extraction tools. There is a need for an upscaling approach that is capable of coming up with a representative large PN model of a core. A novel pore-network stitching method (PNSM) is proposed as an upscaling solution to address this issue (Chapter 3).

- The challenge of inaccuracy of quasi-static PN models, although computationally efficient, in predicting residual trapped CO_2 at the end of a drainage-imbibition cycle. Modified pore-level flow models during imbibition pore-level events of PN modeling are proposed to address this challenge (Chapter 4).

The motivation for using and comparing different pore-scale modeling approaches in Chapter 2 is to address challenges noted above for modeling

CO_2-brine flow in a Mt. Simon sandstone sample. The goal is to characterize the heterogeneous sample used in a CO_2 injection project and apply different simulation approaches to assess their capabilities in terms of prediction of relative permeabilities with different measurement approaches and their computational efficiency.

The motivation for developing PNSM in Chapter 3 comes from investigation of available core-scale scans of various rock samples at different scales. As an example, grayscale images with resolution of about 10–20 microns reveal a wide range of size distribution of pores across a core. Such images cannot be directly used in pore-scale modeling due to lack of precision in identifying narrow channels. However, they cover a large size of the core thereby allowing study of the heterogeneity of the sample. Some regions of interest of the cores can be imaged with increased resolution to reveal more details of pore space needed for pore-scale modeling of flow. The goal of PNSM workflow is to take these images as inputs, extract their PNs, generate new pore elements in terms of PN layers and volumes, stitch all PN pieces together, and come up with a large representative PN, as an output, of the heterogeneous core.

The motivation for proposing modified pore-level flow models in PN modeling in Chapter 4 comes from the discrepancy between reported experimental values of trapped CO_2 and predicted ones from quasi-static PN modeling at the end of drainage-imbibition cycle. Since the capillary forces are mainly controlling the interface movement and filling of pores in CO_2-brine flow system, one should investigate threshold local capillary pressure relations in different pore elements which determines the order of competing pore-level events during imbibition process. Different scenarios of displacement events can be studied using DNS on geometric PN configurations to propose modified relations with new parameters and factors. The proposed modifications can then be incorporated in a quasi-static PN flow solver to evaluate residual trapped CO_2 and relative permeabilities and compare them with experimental measurements.

1.3 Outline

The organization of the rest of this dissertation is as follows. In Chapter 2, a heterogeneous sandstone used in CCS is characterized and studied in-depth with three distinct computational approaches — LB method, FV method, and PN modeling — to evaluate its drainage evolution and relative permeability curves of CO_2-brine flow. Chapter 3 introduces a novel PNSM to provide a large-enough representative PN for a heterogeneous core where conventional pore-scale modeling approaches are not computationally capable of representing. In Chapter 4, pore-level events of PN modeling of CO_2-brine flow during imbibition are investigated by applying LB simulation on some geometric PN configurations. A new set of equations are proposed and tested for the threshold local capillary pressure of pore-body filling and snap-ff events to assess residual trapping of CO_2. At the beginning of each of Chapters 2, 3, 4, the full title of the chapter and its extended abstract are provided. Finally, Chapter 5 provides conclusions of the dissertation along with suggestions for the future work.

Chapter 2

Comparison

Two-phase flow of CO_2-brine in a heterogeneous sandstone: Characterization of the rock and comparison of the lattice-Boltzmann, pore-network, and direct numerical simulation methods

Understanding the physics of two-phase flow of CO_2 and brine in porous geological formations is essential to sequestration of carbon dioxide in deep saline reservoirs, as well as the older problem of enhanced oil recovery from hydrocarbon reservoirs by CO_2 injection. A pilot CO_2 injection in Decatur, Illinois, was undertaken, with the injection zone being the highly saline and heterogeneous Mt. Simon sandstone, in order to better understand the feasibility of full-scale sequestration process. This chapter reports the results of an extensive study of the morphology of the sandstone and its heterogeneity, and simulation of single-phase and two-phase flow of CO_2 and brine in the formation's three-dimensional images. As we demonstrate by extensive analysis, the formation is much more heterogeneous than the typical sandstone, such as Berea sandstone. In addition to characterizing the morphology of the sandstone and computing its important flow characteristics, an important goal of the study is to compare the accuracy and computational efficiency of three distinct simulation approaches, namely, the lattice-Boltzmann (LB) approach, direct numerical simulation (DNS) of the governing equations of fluid flow that uses the finite-volume method coupled with the OpenFOAM simulator, and pore-network (PN) simulation. After validating the simulators by comparing the computed relative permeabilities that they produce for Berea sandstone, we simulate displacement of brine by CO_2 at low and relatively high capillary numbers, and compute the relative permeabilities and other quantities of interest. We demonstrate that all the three methods provide consistent relative permeability-saturation functions that are in close agreement with one another. However, although the LB and DNS both produce

similar relative permeabilities, the DNS approach is computationally more efficient because it simulates drainage by only a single set of computations over the entire saturation range, whereas the LB simulation requires separate simulation for each set saturation. Thus, the question of what method to use for simulating such flow processes at the scale of core plugs should mainly be addressed based on the computational time that one can afford and the computational resources that one has access to. Another important question addressed is the effect of the resolution of the computational grids or lattices used, particularly when one uses the LB method with voxelized images of porous media. We show that, unlike many claims in the past, one may need many lattice units per voxel in order to obtain reliable, lattice-independent results.

This chapter is published in the journal of *Advances in Water Resources* in collaboration with colleagues at the University of Southern California (Kohanpur et al. 2020). The author of this dissertation performed data acquisition from Energy Data eXchange (EDX), processing all raw grayscale micro-CT images, image analysis of pore space properties of all subsamples, constructing PN models, and running all PN and LB simulations with post-processing of their results in addition to post-processing saturation distribution of OpenFOAM simulations. The in-house LB code was originally developed by Chen et al. (2018). A similar comparative study of PN and LB simulations of CO_2-brine flow with these tools was reported by us (Kohanpur et al. 2016). Moreover, this LB code was part of a comprehensive study of comparison of several pore-scale models by Zhao et al. (2019).

2.1 Introduction

The physics of two-phase flows in porous media is of utmost importance to many problems of practical interest, such as CO_2 sequestration in deep saline reservoirs, recovery of oil from hydrocarbon reservoirs, transport of non-aqueous-phase liquid contaminants in aquifers, and infiltration of rainfall into soil. Understanding and predicting the properties of such flow processes at various length scales are vital to addressing the problem of global warming, as well as managing water resources, and energy production.

There is increasing incentive for studying two-phase flow of CO_2 and

brine in porous media, due to societal interest in geological sequestration of CO_2. The drastic increase in the amount of CO_2 in the atmosphere plays the most important role in global climate change (Friedlingstein and Solomon 2005; Metz et al. 2005; Nordbotten and Celia 2011). The main source of the atmospheric CO_2 is combustion of fossil fuels for producing electricity in power plants. Among the various approaches that have been suggested for mitigating the problem, CO_2 capture and storage (CCS) is believed to be a viable solution (Nordbotten and Celia 2011). The CCS is a process associated with separating CO_2 from the other gases that are produced by power plants and other sources, compressing and transporting it to storage locations, and keeping it sequestered in onshore or offshore geological formations for very long times (Metz et al. 2005). As an example, the United States can inject up to 65% of the CO_2 produced by power plants deep into saline aquifers (Shukla et al. 2010). Since such a sequestration process appears to have great potential, understanding the behavior of flow of brine and CO_2 in deep porous formations is vital (Juanes et al. 2006; Pruess and Garcia 2002) to its successful implementation, and should accompany any comprehensive study of geological storage of CO_2 that includes its economic feasibility, site selection, risk assessment, environmental impact, safety aspects, monitoring and verification, in addition to perspectives on retention time, physical leakage, brine displacement, and microseismicity (Metz et al. 2005).

The Illinois State Geological Survey carried out a pilot injection study to better understand the feasibility of full-scale CCS. The study site is in Decatur, Illinois, and the injection zone is the highly saline Mt. Simon sandstone (Finley 2014). Thus, one goal of the present study is to analyze two-phase flow of CO_2 and brine in Mt. Simon sandstone and, more generally, in natural rock. The phenomenon may be studied at various length scales, including molecular, core, and field scales by experiments and computer simulation. Experiments are, of course, quite useful, but can be difficult to implement, as they are time-consuming and expensive (Joekar-Niasar and Hassanizadeh 2012). At the molecular scale, the interaction between water and water-CO_2 and mixed layer clay was recently studied (Rahromostaqim and Sahimi 2018; Rahromostaqim and Sahimi 2019).

Advances in modeling of porous media, as well as development of efficient computer simulation, together with increasing computer powers, have made it possible to model and study in detail two-phase flow of brine and CO_2

at core plug and larger length scales. Compared to experiments, the computational approaches have the advantages of being generally less expensive and more flexible in implementing and changing parameters, flow and displacement mechanisms, and studying various mechanisms of displacements. At the same time, numerical simulation of flow of brine and CO_2 at field scale requires such inputs as the relative permeabilities and capillary pressure as functions of the saturation at the scale of the grid blocks, which can be obtained by experiments, or by pore-scale modeling.

Pore-scale modeling (Celia et al. 1995) can provide the required input data for field-scale modeling, provided that one takes into account the effect of the morphology of the core-scale porous media and the various pore-scale mechanisms of fluid displacements. This is because pore-scale flow affects significantly the characteristics of the process at larger scales, including injection and storage of CO_2 in depleted reservoirs and other types of large-scale porous formations (Juanes et al. 2006; Pruess and Garcia 2002; Raeini et al. 2014).

With advances in instrumentation, it has become possible to obtain three-dimensional (3D) images of porous media with high resolution by, for example, X-ray computed tomography (CT) (Blunt et al. 2013). At pore-scale, detailed 3D geometry of rock and its void space can be captured by direct imaging using nondestructive X-ray microtomography (Dunsmuir et al. 1991; Flannery et al. 1987). Various rock properties, such as the permeability, have been computed with the aid of micro-CT images (Arns et al. 2002; Øren and Bakke 2002; Ramstad et al. 2010; Krevor et al. 2012; Bakhshian et al. 2018). Thus, one can directly simulate two-phase flows in the images, which renders as unnecessary developing models of the pore space. Image-based methods are, however, computationally expensive, although recent advances in high-performance computing, as well as a new method that smoothens the image without changing its properties using curvelet transformations (Aljasmi and Sahimi 2020), are making use of such methods increasingly common. The methods that are used for simulating fluid flow in the images are either based on directly solving the governing equations for fluid flow, i.e., the Stokes' equation using the finite-volume method (Ferrari and Lunati 2013; Huang et al. 2005; Rabbani et al. 2017), or based on the lattice-Boltzmann (LB) method (Boek and Venturoli 2010; Ferreol and Rothman 1995; Pan et al. 2004; Porter et al. 2009; Ramstad et al. 2012; Rothman 1990). The LB

method has been demonstrated to be well-suited for high-performance parallel computing in the complex geometry of porous media (Ahrenholz et al. 2008; Chen et al. 2018; Ramstad et al. 2012; Tölke et al. 2006). In addition, advances in method based on the volume of fluids, especially the new developments of surface force formulation, have made it possible to efficiently model two-phase flow by the finite-volume method at lower capillary numbers (Gueyffier et al. 1999).

Another approach is based on pore-network models (PNMs) (Sahimi 2011; Blunt et al. 2013) in which the pore space is simplified to a network of interconnected pore-bodies and pore-throats. While the PNMs are computationally very efficient and inexpensive, they still involve some assumptions and approximations, such as the definition of what constitutes a pore-body or pore-throat, how to assign effective sizes to them, etc. (Ramstad et al. 2012; Joekar-Niasar and Hassanizadeh 2012). Therefore, a detailed comparison between the results of the PNM computations with those obtained by the other two aforementioned methods will shed much light on its advantages and limitations.

The goal of this chapter is twofold. One is computing the drainage relative permeability functions for CO_2 and brine during injection of the former into a sample of Mt. Simon sandstone. This is not a trivial problem as Mt. Simon sandstone is much more heterogeneous than typical sandstones studied in the past, such as the Berea sandstone. Moreover, the viscosity ratio of the two fluids are much higher, about 10 times larger, than of that the typical oil-water systems. The two challenges lead to computational difficulties that require careful choices of the input parameters, discretization, and boundary conditions. The second goal is evaluating the performance of the LB method and PNMs by comparing the relative permeabilities computed by them with those obtained through the direct numerical simulation of the fluid flow in the image of the sandstone. In addition, we also study the effect of the capillary number, i.e., the effect of flow, on the results.

The organization of the rest of this chapter is as follows. In the next section the porous formation whose flow properties will be computed is described. Section 2.3 provides brief description of the three distinct computational approaches that we have utilized in our work. The validation of the computational methods is described in Section 2.4, while the main results of the chapter are presented and discussed in Section 2.5. In Section 2.6

we discuss the significance of the resolution of the lattices used in the LB simulations. The main results are summarized in the last section.

2.2 Mt. Simon sandstone

The sample porous medium is from Mt. Simon sandstone at a depth of 6700 feet. The formation is located at verification well number 2 of a study site in Decatur, Illinois where, as mentioned earlier, Illinois State Geological Survey carried out a pilot injection study to better understand the feasibility of full-scale CCS (Finley 2014). A core plug from the formation was scanned by micro-CT imaging technique at the National Energy Technology Laboratory (NETL) of the U.S. Department of Energy, which produced a series of gray-scale scans. Table 2.1 presents the information of a cubic sample from the core plug. A series of image processing steps were taken in Fiji (Schindelin et al. 2012) to filter and smooth images in order to distinguish void space from the solid grains via a thresholding algorithm. The outcome was a segmented 1200^3 voxels sample with porosity of 27.1% and voxel size of 2.80 μm, i.e., a 3.363 mm^3 sample.

Table 2.1: Rock source and properties.

Rock type	Mt. Simon sandstone
Depth (feet)	6700
Scans resolution (μm)	2.80
Images size (voxels)	1200^3
Sample size (mm^3)	3.36^3
Porosity (%)	27.1

We took eight equal-size subsamples (each of size 500^3 voxels) from the center of the main sample to study its geometrical, topological, and flow properties. Table 2.2 presents a list of the subsamples with their corresponding porosity. Fig. 2.1 presents both a high-resolution cross section of the original sample and a 3D representation of a 500^3 voxels subsample S2. One slice of this subsample in both gray-scale and segmented format is presented in Fig. 2.2. Table 2.3 presents the important properties of subsample S2.

Table 2.2: Porosity of eight subsamples of Mt. Simon sandstone.

Subsamples name	Porosity
S1	0.258
S2	0.263
S3	0.272
S4	0.274
S5	0.287
S6	0.274
S7	0.283
S8	0.293

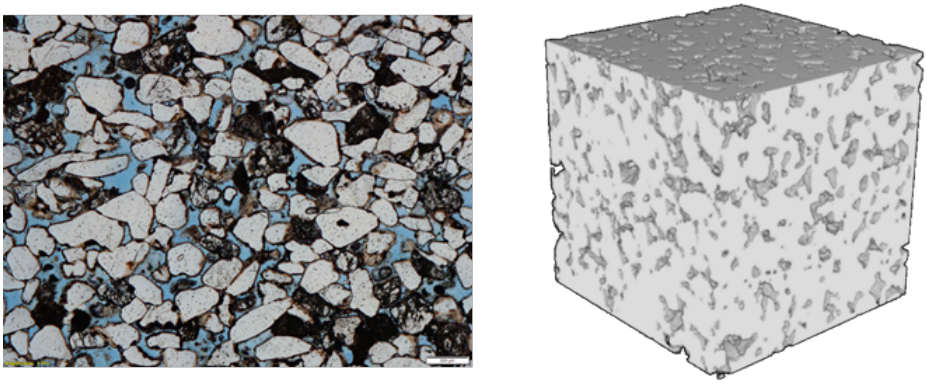

Figure 2.1: Thin-section scan of Mt. Simon sandstone at a depth of 6700 feet, and a 500^3 subsample S2 of the formation selected for the two-phase flow simulation.

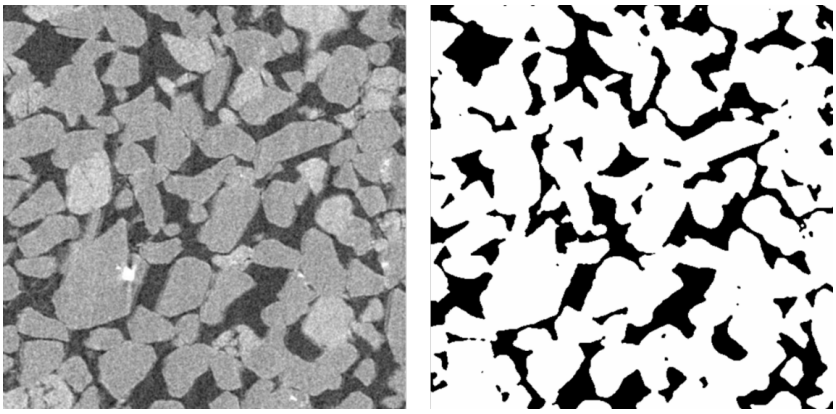

Figure 2.2: Gray-scale (left) and segmented (right) formats of the 300th slice (out of 500 slices) of the selected Mt. Simon sandstone subsample S2.

Table 2.3: Properties of the selected Mt. Simon sandstone subsample S2. The permeabilities are in mD.

Sample size (voxels)	$500 \times 500 \times 500$
Sample size (mm^3)	$1.4 \times 1.4 \times 1.4$
Porosity (%)	26.3
Permeability by the LB simulation	4278
Permeability by the DNS	4370
Permeability by the PNM	4201

2.2.1 Construction of the pore-network

To characterize the heterogeneity of Mt. Simon sandstone, as well as carrying out single- and two-phase flow simulations, we extracted from the images the equivalent PNMs of the eight sandstone subsamples. To do so, we used the maximal ball (MB) algorithm (Dong and Blunt 2009) that searches the entire voxelized pore space in order to identify the largest possible spheres in the porous medium. The algorithm was developed originally by Silin and Patzek (2006) and was extended and improved by Al-Kharusi and Blunt (2007), Dong and Blunt (2009), Arand and Hesser (2017), and Raeini et al. (2017). In the algorithm the input is the voxelized binarized geometry of the porous medium in which the solid and pore phases are stored as 1 and 0, respectively. All the zero voxels are scanned and the largest possible voxelized sphere in the pore space for each of them is determined. The resulting voxelized sphere for each pore voxel is taken as the MB. In practice, many MBs are inside the larger MBs and, therefore, should be removed.

The resulting MBs are sorted and clustered based on their size that helps identifying the ancestor MBs — the local maximums based on the size — and a chain of the MBs that are from one ancestor to another one (Dong and Blunt 2009). Each chain is segmented such that it represents a configuration of two pore-bodies and their connecting pore-throat. Finally, by counting voxels of each element, pore-body or pore-throat, various geometrical features, such as the location, radius, volume, length, and shape factor are calculated and stored. The pore-throat length is defined as the difference between the total pore-throat length and the lengths of the neighboring pore-bodies. The pore-body length is defined as a function of its radius and the total pore-throat length is defined as center-to-center Euclidean distance between two neighboring pore-bodies (Dong and Blunt 2009).

The shape factor G summarizes all the irregularities of the geometry of the pore-bodies and pore-throats by, $G = VL/A^2$, where A is surface area, and V is volume of the voxelized element. L is defined as twice the distance between the center of the ancestor MB and the farthest voxel in that MB (Dong and Blunt 2009). The shape factor is a key quantity that helps assigning familiar geometries, such as circles, squares, and triangles, to the cross sections of the pore-bodies and pore-throats in the PNM flow solvers (Patzek and Silin 2000; Patzek and Kristensen 2001).

Fig. 2.3 presents the resulting PNM for sample S2 of Mt. Simon sandstone that we generated using the algorithm, as well as the size distributions of its pore-bodies and pore-throats. The ratio of the median pore-throat length and the radius is about 16.7. Table 2.4 presents the data for the connectivity of all the eight samples in terms of the average coordination number of their resulting PNMs. The connectivity density of the samples, i.e., connectivity per unit volume, is on the order of 2×10^{-5} [pixel^{-3}], while the ratio of their pore-throat length and radii is similar to that of sample S2.

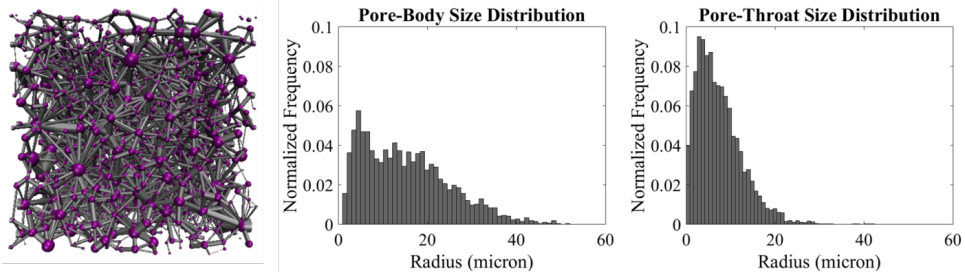

Figure 2.3: The PNM of Mt. Simon sandstone and its pore-body and pore-throat size distributions.

Table 2.4: The connectivity and anisotropy of the eight subsamples.

Subsamples name	Average coordination number	Degree of anisotropy
S1	4.77	0.23
S2	4.85	0.25
S3	4.90	0.19
S4	4.73	0.18
S5	5.24	0.19
S6	5.02	0.18
S7	4.78	0.25
S8	5.11	0.22

Also shown in Table 2.4 is the degree of anisotropy (DA) of all the eight

samples. The DA is a measure of how highly oriented the pore structure of a medium is within a volume (Harrigan and Mann 1984; Odgaard and Gundersen 1993; Odgaard 1997; Toriwaki and Yonekura 2002). We used the BoneJ plugin in Fiji, the image processing package, to calculate the DA of the void space of the eight samples. The method is based on the mean intercept length (MIL) method by which a large number of equal-length vectors originating from a random point within the pore space are drawn and an intercept is counted for each vector when it hits a boundary. The MIL is the vector length divided by the number of boundary hits. A cloud of points is formed where each point represents the vector times its MIL, and then an ellipsoid is fitted to the cloud. The anisotropy tensor is then constructed, and the eigenvalues and eigenvectors related to the lengths and orientations of the ellipsoid's axes are computed (Odgaard 1997). The DA is defined as:

$$DA = 1 - \frac{\text{smallesteigenvalue}}{\text{largesteigenvalue}} \tag{2.1}$$

The algorithm is stochastic and, therefore, new random points with the same vectors yield new MIL counts. The DA must be updated until either the minimum number of sampling points is reached or the coefficient of variation of DA becomes smaller than a threshold. As Table 2.4 indicates, the samples are slightly anisotropic. Thus, we ignore it in the flow calculations.

2.2.2 Analysis of the heterogeneity

We carried extensive analysis of the morphology of the selected sample of Mt. Simon sandstone in order to characterize the severity of its heterogeneity. This was accomplished by analyzing the 3D image of sample S2, extracting its equivalent PN, and comparing the results to those of a sample Berea sandstone, which is a fairly homogeneous porous medium and whose properties are presented in Table 2.5. In the study of the heterogeneity via image analysis, we took fifteen equal-size subsamples, each 1/8 of the original sample, eight of which were from the corners, six from the sides, and one at the center. We then computed the porosity and degree of anisotropy DA of the subsamples. The results are presented in Fig. 2.4.

To quantify the variability across the subsamples, we computed the co-

Table 2.5: Berea Sandstone characteristics.

Rock type	Berea sandstone
Scans resolution (μm)	5.34
Images size (voxels)	400^3
Sample size (mm^3)	2.14^3
Porosity (%)	19.6

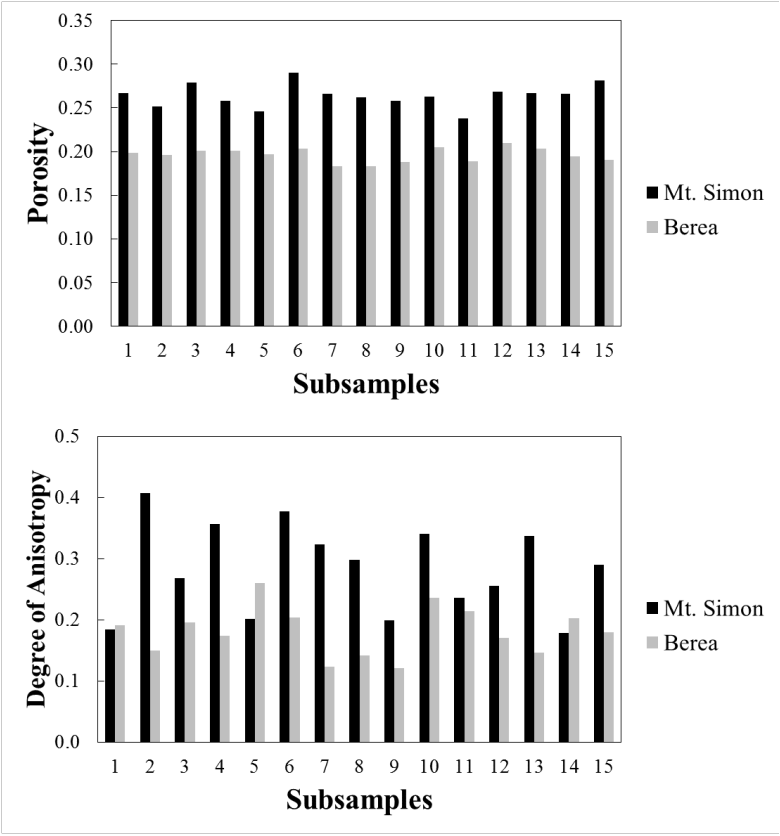

Figure 2.4: Porosity and degree of anisotropy of 15 subsamples from the Mt. Simon sandstone sample S2 and their comparison with those of the Berea sandstone sample.

efficient of variation (CV) of each property for each sample. The results are presented in Table 2.6, according to which the CVs of the porosity and the DA from the Mt. Simon sandstone are larger than those for the Berea sandstone sample, hence indicating that the former has more variability is more heterogeneous.

Table 2.6: Comparison of the coefficient of variation (CV) of the properties of the Mt. Simon sandstone sample S2 and the Berea sandstone sample.

Sample	CV, Porosity	CV, DA
Berea	0.039	0.214
Mt. Simon	0.049	0.250

In analyzing the heterogeneity of Mt. Simon sandstone using the PN, we used a stochastic approach whereby a calculation box with a size 1/8 of the PN extracted from the original sample was selected randomly. Then, the average coordination number Z of the pore-bodies inside the calculation box was calculated, since Z quantifies the connectivity of the pore space well. The results for 100 realizations of the Mt. Simon sandstone sample S2, and their comparison with those for the Berea sandstone sample are presented in Fig. 2.5. According to the data, the CV of the average coordination numbers is 0.054 for the Mt. Simon PN, but 0.025 for the Berea PN. Therefore, the Mt. Simon sandstone sample S2 encompasses more variability in its pore connectivity relative to the Berea sandstone sample and, thus, it is more heterogeneous.

2.2.3 Determining the size of the representative elementary volume

A careful study was undertaken in order to determine the size of the representative elementary volume (REV) for the flow studies. It turned out that a size of 500^3 voxels was large enough to represent the average flow properties. Fig. 2.6 presents three computed properties of the sample versus its linear size, calculated by Fiji, while Fig. 2.7 shows the variation of the absolute permeability computed by the LB simulation in order to identify the size of the REV. The variation of the computed properties with the sample size becomes negligible at a size of about 300^3 voxels, thus justifying the choice of simulation sizes larger than the identified size.

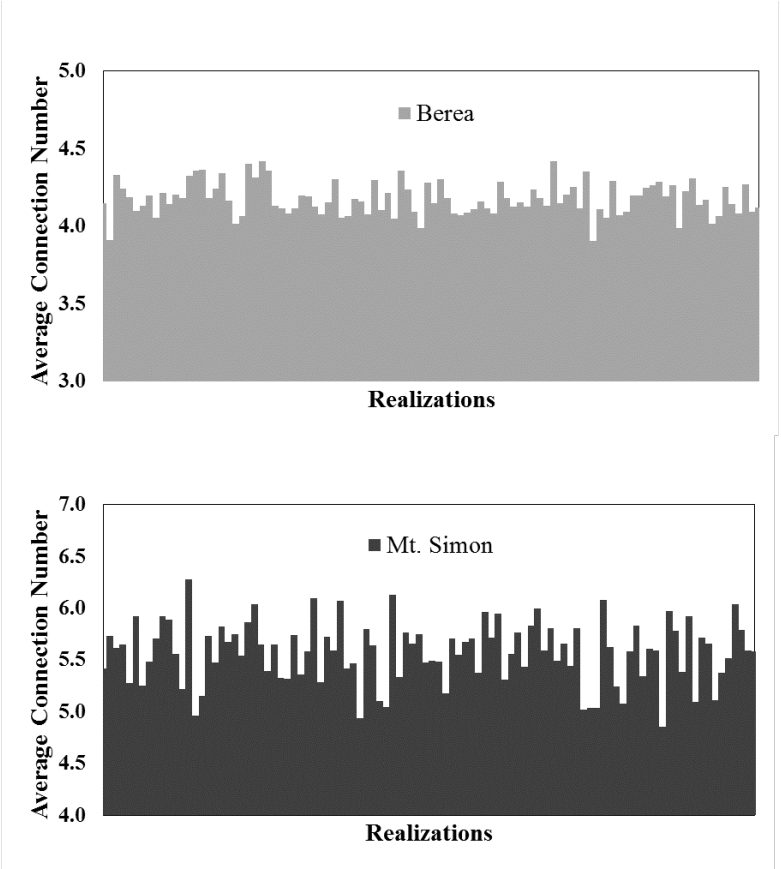

Figure 2.5: Statistics of the average coordination numbers of over 100 realizations of the pore-network of the Mt. Simon sandstone sample S2, and the corresponding Berea sandstone sample.

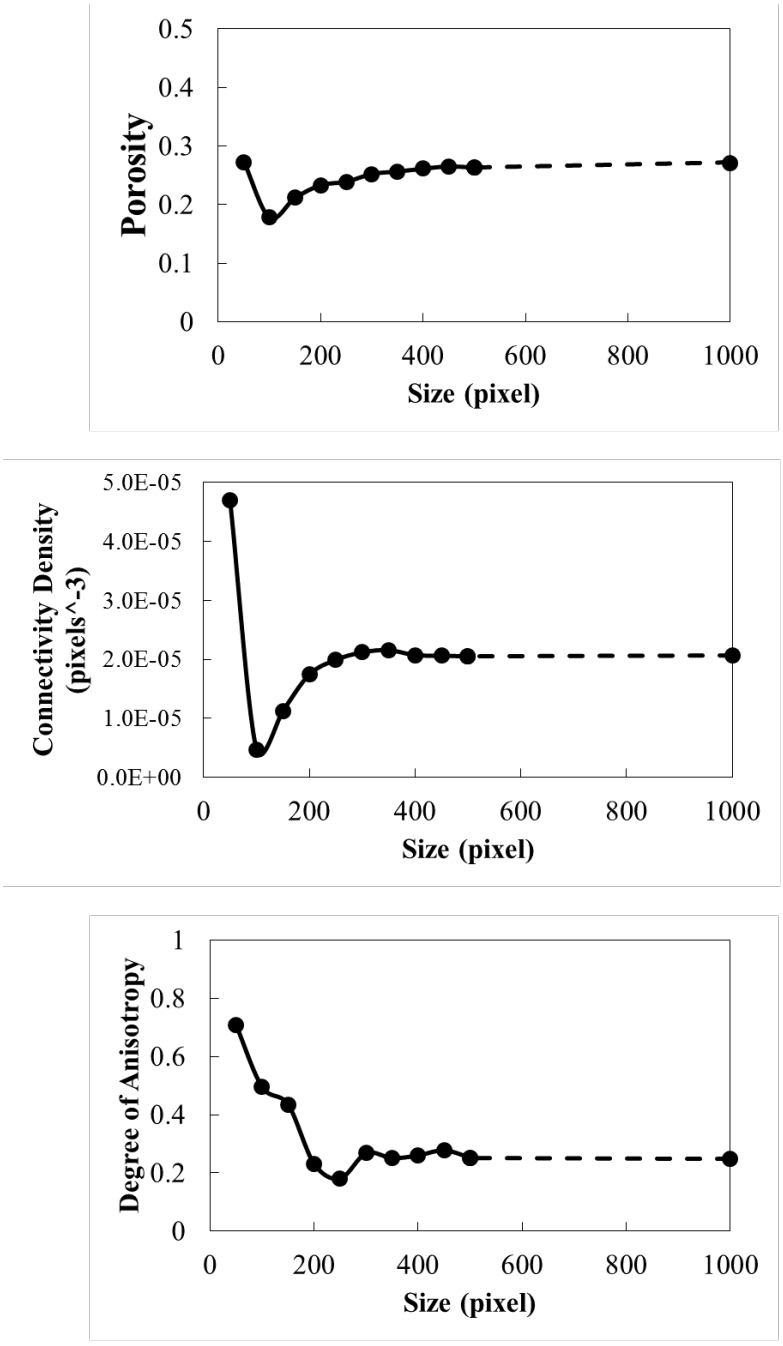

Figure 2.6: Sample-size dependence of three properties of the subsample S2 of Mt. Simon sandstone in order to identify the size of the REV.

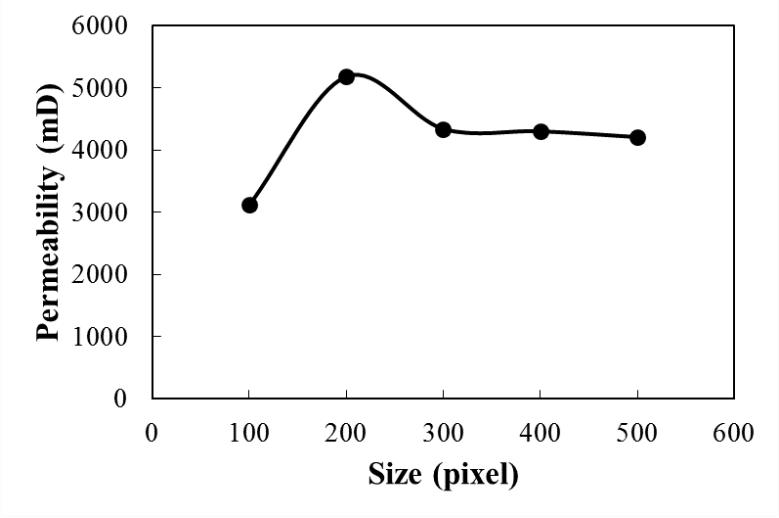

Figure 2.7: Sample-size dependence of absolute permeability, computed by the LB simulation, of subsample S2 of Mt. Simon sandstone.

Using the three computational approaches described in the next section, we also carried out single-phase flow simulation with the eight subsamples employing the three aforementioned approaches, namely, the LB method, direct numerical simulation of Stokes' flow using OpenFOAM, and PN calculations, in order to evaluate the absolute permeability of each of the eight samples. The results will be discussed shortly. For now, it suffices to say that they indicate that the original sample is highly heterogeneous since different subsamples from different locations have different average properties, while they are also representative of a REV. Thus, as mentioned earlier, to study two-phase flows, we selected subsample S2 in Table 2.2, whose characteristics are presented in Table 2.3.

2.3 Computational approaches

As mentioned earlier, we have carried out extensive simulations of fluid flow using three distinct computational methods, the details of each are as follows.

2.3.1 The lattice-Boltzmann method

As is well known, the LB method is based on streaming, collision and relaxation of a set of fluid particle distribution functions (PDF) on a lattice. The no-slip boundary conditions on solid surfaces are implemented by simply switching the directions of the particles on the surface nodes, the so-called bounce-back scheme. There are several LB schemes for simulating multiphase flows (Huang et al. 2015; Liu et al. 2016). Among them, the color-fluid model (Grunau et al. 1993; Gunstensen et al. 1991) is capable of producing a relatively sharp interface between completely immiscible fluids, which is why it has been widely adopted (Ahrenholz et al. 2008; Jiang and Tsuji 2017). In addition, it can deal with high viscosity ratios due to its independent control of the surface tension and viscosity (Chen et al. 2018). In the present work, we use a variant of the multiple relaxation time (MRT) color-fluid LB simulator (Tölke 2002; Tölke et al. 2006; Chen et al. 2018).

In the model, each phase has its own set of PDFs and the discrete Boltzmann's equation is solved for each fluid phase. In our in-house LB code, we consider two sets of the D3Q19 PDFs, i.e., a 3D model with 19 velocities, representing the two fluid phases, referred to as the fluids r and b, which follow the collision-streaming procedure for the PDF:

$$f_i^s\left(x+e_i\Delta t, t+\Delta t\right) = f_i^s\left(x,t\right) + \Omega_i^{s(3)}\left\{\Omega_i^{s(1)} + \Omega_i^{s(2)}\right\}, s = r, b \qquad (2.2)$$

where $\Omega_i^{s(1)}$ is the standard LB collision operator, $\Omega_i^{s(2)}$ is the perturbation step that generates the surface tension effect, and $\Omega_i^{s(3)}$ is the recoloring step that separates the two fluids. The collision operators $\Omega_i^{s(1)}$ and $\Omega_i^{s(2)}$ are constructed under the MRT framework that increases stability and accuracy of the model (Lallemand and Luo 2000; Tölke et al. 2006; Chen et al. 2018; d'Humieres 2002). More details of our in-house code are given by Chen et al. (2018). The macroscopic quantities, such as fluid velocity and pressure, are computed by calculating the moments of the PDF. Since the outputs produced by the LB simulation are defined in terms of lattice units, they must be converted to physical units (Ramstad et al. 2012; Sukop 2006).

In the present work, we simulate a method of measuring the relative permeabilities known as the steady-state method. In this method a prede-

fined fractional flow of both fluid phases is injected into the pore space at constant flow rates, while the pressure drop across the sample is constant. Steady state is reached when the downstream and upstream fractional flows are equal. More details about the steady-state measurement are given by Honarpour et al. (1986). In the LB model, the predefined fractional flow is implemented as an initial randomly distributed saturation that will also be the target saturation. We mirror the input geometry and impose periodic boundary conditions along the flow direction as well, in order to allow both fluid phases enter and exit the model smoothly. A body force is applied to each fluid phase to achieve the same pressure drop and avoid capillary-end effects. To ensure that steady state has been reached, various quantities, such as the flow rates, should be monitored in order to check whether they converge to steady-state values, which are then used for the relative permeability calculation at the set target saturation. A similar method of measuring relative permeabilities was described by Ramstad et al. (2012).

2.3.2 Direct numerical simulation

The second computational method that we employed was direct numerical simulation (DNS) using the OpenFOAM open source for both single-phase and two-phase fluid flow. The simulator uses finite-volume discretization and solves the continuity and momentum equations — the Stokes equations — in the pore space. We used an unstructured mesh with grid size of 2^3 and 1 voxels in the pore volumes and throat, and corner points between the solid boundaries, respectively, meaning that the grid blocks that are used in the throats and the corners are half the size in each direction of those used in the pores, employing a modified OpenFOAM mesh generator (Raeini 2013). The total number of grid blocks used to discretize the image volume was 10,815,820. For each capillary number, the simulations employed 300 processors in parallel. Unlike the LB method, the finite-volume simulations are run under unsteady-state conditions, and the results are measured in a dynamic drainage simulation. More details about the method and its implementations are given in the two phase flow solver of OpenFOAM (interFOAM) (Ubbink 1997). As usual, Darcy's law and its generalization to two-phase flow, are assumed.

There are various methods for upscaling the microscopic dynamic and capillary pressures to the Darcy-scale pressure, but it is not clear which method averages the microscopic pressure most accurately. Raeini et al. (2014) analyzed five methods in a steady-state incompressible single-phase flow calculation to obtain the Darcy-scale pressure drop. Among all the methods the velocity-weighted average of the viscous forces, as well as the velocity- weighted average of the pore-scale pressure gradient, matched the experimental results most closely. The same equations with some modifications can be used to calculate the macroscopic pressure drop in two-phase flow. In the DNS simulations, the velocity-weighted average of the viscous forces was employed in order to calculate the total macroscopic pressure drop (ΔP_α) in each phase:

$$\Delta P_\alpha = -\frac{1}{Q_\alpha} \int u \cdot [\nabla \cdot (\mu \nabla u)] \, \mathrm{d}V_\alpha \tag{2.3}$$

$$\mu = \beta \mu_1 + (1 - \beta)\mu_2 \tag{2.4}$$

where α may be either the wetting or non-wetting phase, Q_α is the flow rate of phase α, u is the velocity vector, and V_α is the portion of flow volume filled with phase α. In Eq. (2.4) μ_1 and μ_2 are viscosities of the two fluids, and β is the volume fraction of fluid 1 in each grid cell. More details on upscaling of pore-scale forces are given by Raeini et al. (2014).

Various methods have been developed for including the interfacial tension in Eulerian grids. They include the continuous surface stress (CSS) (Gueyffier et al. 1999), continuous surface force (CSF), sharp surface force (SSF) (Francois et al. 2006), and filtered surface force (FSF) (Raeini et al. 2012). The main problem with the CSF is the spurious velocity in the flow field, which, to some extent, is controlled in the SSF method. Controlling the sharpness of the capillary pressure in the SSF method is accomplished by defining a sharpened indicator function. In the FSF method the indicator is modified to have a smoother capillary force compared to the SSF approach for the interface motion. This modification compresses the transition area of the capillary pressure. With this implementation, the issue with the non-physical velocities that may arise is resolved, and the capillary pressure transition area is only one grid block. Therefore, the FSF formulation is used for the complex geometry used in this study.

2.3.3 Pore-network model

The PNM simulation of drainage — displacement of brine by CO_2 — was carried out under the quasi-static condition, which corresponds to low capillary number. It uses an invasion percolation (IP) algorithm (Wilkinson and Willemsen 1983; Wilkinson and Willemsen, 1983; for the most efficient algorithm to simulate the IP see Sheppard et al. 1999 and Knackstedt et al. 2000). All the pore elements were initially saturated with the wetting phase. Pore elements become occupied by injecting non-wetting phase through piston-like displacement and based on the Young-Laplace equation that connects the pressure in the two phases at the interface between them. The complete procedure that we used is described by Valvatne and Blunt (2004), and need not be repeated here. All the pore-bodies and pore-throats were assumed to triangular cross sections.

In all three approaches the usual generalized Darcy's law for multiphase flows,

$$V_\alpha = -\frac{k_{r,\alpha}(S_\alpha)}{\mu_\alpha}\frac{\Delta P_\alpha}{\Delta x} \tag{2.5}$$

was used to compute the relative permeabilities, where $k_{r,\alpha}$ is the relative permeability of phase α, S_α is its saturation, and v_α is its corresponding Darcy velocity, which is proportional to total flow rate passing through the medium. The relative permeability is generally a function of the phase saturation, wettability, and the structure of the pore space. The competition between the capillary and viscous forces influences the displacement of one fluid by the second one, which is expressed by the capillary number Ca:

$$Ca = \frac{\mu\,(Q_{tot}/A)}{\sigma} \tag{2.6}$$

where Q_{tot} refer to the total flowrate of phases, μ is effective viscosity, A is the cross-sectional area, and σ is the surface tension.

2.4 Test of the accuracy of the numerical approaches

We tested our computational methods with an oil-water system in a water-wet Berea sandstone sample. The sample, having the data listed in Table 2.5, has been extensively studied and used in the literature (Raeini

et al. 2014; Ramstad et al. 2012; Valvatne and Blunt 2004) and is considered a benchmark. We compare the calculated relative permeabilities of the oil-water system during drainage with the experimental data (Oak et al. 1990) in Fig. 2.8. Table 2.7 presents the properties of the two-phase flow system. The LB results for the water relative permeabilities are slightly larger than the experimental data but, as we discuss below, this is due to the resolution of the lattice used in the simulation. As the resolution increases, the agreement between the LB results and the data improves significantly. The agreement between the DNS results and the data is excellent.

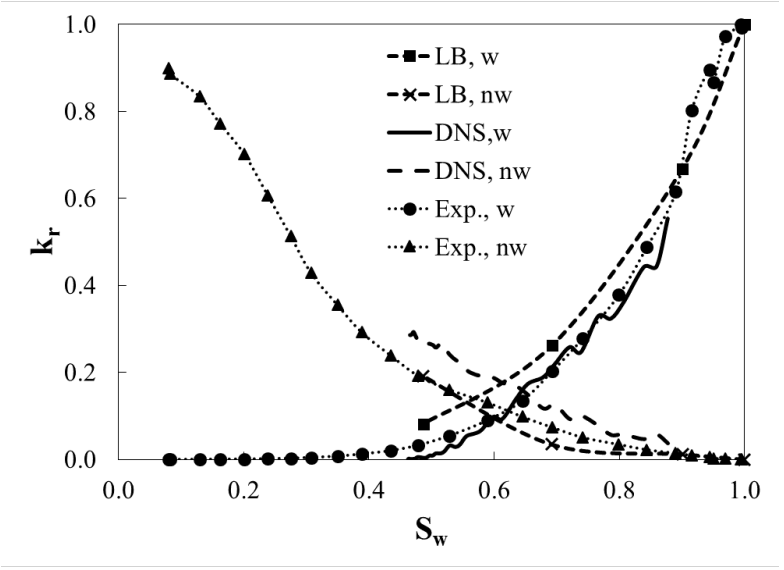

Figure 2.8: Drainage relative permeabilities of the oil-water pair in a Berea Sandstone sample with contact angle of 125^o, capillary number of 5×10^{-5}, and viscosity ratio of 1.32.

Table 2.7: Properties of CO_2-brine pair for the LB simulation and DNS.

Properties	Value
Contact angle (°)	125 (water-wet)
Interfacial tension (mN/m)	30.0
Water density (Kg/m^3)	1000
Oil density (Kg/m^3)	1000
Water viscosity ($Pa \cdot s$)	1.05×10^{-3}
Oil viscosity ($Pa \cdot s$)	1.39×10^{-3}
Viscosity ratio	1.32
Capillary number	5×10^{-5}

The results from the DNS and LB methods are reported up to the water

saturation of about 45% ($S_w = 0.45$) where water permeability becomes negligible. We did not further continue the simulations due to the limited computational resources.

2.5 Results and discussion

After validating our computational methods with the experimental data, we carried out extensive simulation of both single- and two-phase flow in the image of Mt. Simon sandstone. In what follows we present and discuss results.

2.5.1 Single-phase flow

As pointed out earlier, the size of the REV for the single-phase simulations with the eight subsamples was 500^3 voxels. Using the DNS, we computed the single-phase permeability for an image size of 500^3 and resized subsamples of size 250^3 voxels (with the same physical size, i.e., 1.43 mm^3, but with a coarser image resolution of 5.6 μm) with the upstream and downstream pressures of 5 Pa and 0 Pa. The fluid density and viscosity were set to be the same as those of brine, $\mu = 0.0011$ $Pa.s$ and $\rho = 1100$ $kg/m3$. Fig. 2.9 shows the original mesh, and the pressure distribution of the subsample S5 with 500^3 voxels.

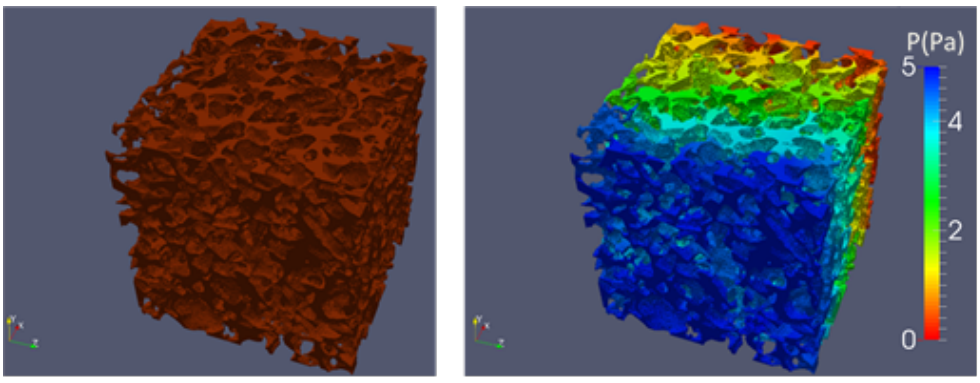

Figure 2.9: The 3D pore volume of the subsample S5 (left) and the pressure distribution in the volume at the end of the simulation (right).

The same properties were used in the LB method to calculate the absolute permeabilities for both sizes. However, due to the low computational cost of

simulation of single-phase flow with the PNM, no resizing was needed, and the simulations were performed only with the original 500^3 voxels samples. The main purpose of carrying out the LB and DNS simulations on the resized subsamples was reducing the size of the input geometry of our two-phase flow simulations that reduces significantly the computational costs for both methods. The absolute permeabilities of the eight subsamples, calculated by the DNS, LB and PNM, are reported in Table 2.8.

Table 2.8: Comparison of the absolute permeability of the eight subsamples computed by the PNM, LB and DNS methods. The results obtained by the LB and DNS methods are for two sample sizes of 250^3 and 500^3 that have resolutions of 5.6 and 2.8 μm, respectively.

Subsamples	Porosity	Permeability (mD)				
		PNM (500^3)	LB (250^3)	LB (500^3)	DNS (250^3)	DNS (500^3)
S1	0.258	3843	3883	3638	4147	3971
S2	0.263	4201	4211	4278	4530	4370
S3	0.272	5037	5053	4818	4555	4376
S4	0.274	5283	5746	5772	5521	5344
S5	0.287	6055	5666	5397	6721	6418
S6	0.274	5884	4830	4614	5085	4860
S7	0.283	6784	5182	5106	8186	7879
S8	0.293	8112	6645	6558	7907	7595

A few features of Table 2.8 are worth pointing out. (i) The absolute permeabilities computed by the DNS and LB for the original 5003 subsamples are quite close to that of the resized 250^3 subsamples. This indicates that the resizing process honors the connectivity of the sample well. The small increase in the permeabilities of the resized 250^3 subsamples is due to the interpolation of the voxelized geometry during downsizing that removes minor irregularities in narrow pores and, thus, reduces flow resistance. However, this does not change the overall connectivity of the sample, and the resulting permeabilities are still in good agreement. As an example, the absolute permeability of subsample S2 changes from 4278 mD to 4211 mD (computed by the LB simulation) after resizing, while its porosity remains almost unchanged. Therefore, the resized 250^3 subsamples were considered as a good-enough approximation of the original 500^3 subsamples, and were used in two-phase flow simulations. (ii) The permeabilities computed by the LB simulations agree with those computed by the DNS for the 500^3 images;

the difference between the two sets of results is about 10% or less in most cases. This is also encouraging. (iii) A comparison of all the computed absolute permeabilities of all the eight subsamples indicates that the original Mt. Simon sandstone is indeed heterogeneous.

2.5.2 Two-phase flow

We used both the LB method and DNS, in addition to the quasi-static PN computations, to carry out simulation of drainage for the CO_2-brine pair in the Mt. Simon sandstone sample S2 and evaluate the drainage relative permeabilities for two capillary numbers Ca. Table 2.8 presents the properties of the CO_2-brine system used in the simulations.

Table 2.9: Properties of CO_2-brine two-phase flow system for LB simulation and DNS.

Properties	Value
Contact angle (°)	180 (brine-wet)
Interfacial tension (mN/m)	30.0
Brine density (Kg/m^3)	1100
CO_2 density (Kg/m^3)	1100
Brine kin. viscosity (m^2/s)	1×10^{-6}
CO_2 kin. viscosity (m^2/s)	1×10^{-7}
Capillary number	1×10^{-4} and 3×10^{-5}
Viscosity ratio	10

We first carried out simulation of drainage with specified injection velocity (or flow rate) at the inlet and pressure boundary condition at the outlet to capture the invasion pattern of Properties of CO_2-brine two-phase flow system for LB simulation and DNS. through the initially brine-saturated sample. In addition, initially, the first 8% of the grid blocks were filled with the non-wetting phase. At the low capillary number, the average inlet fluid velocity was 0.014 m/s, while for the high capillary number the inlet velocity was set at 0.0465 m/s. Fig. 2.10 shows the results produced by the LB simulation, where the CO_2 front was injected into the sample from the left at an average wetting-phase saturation of $S_w = 0.50$, indicating a fingering pattern and very heterogeneous spatial distribution of CO_2 in the pore space.

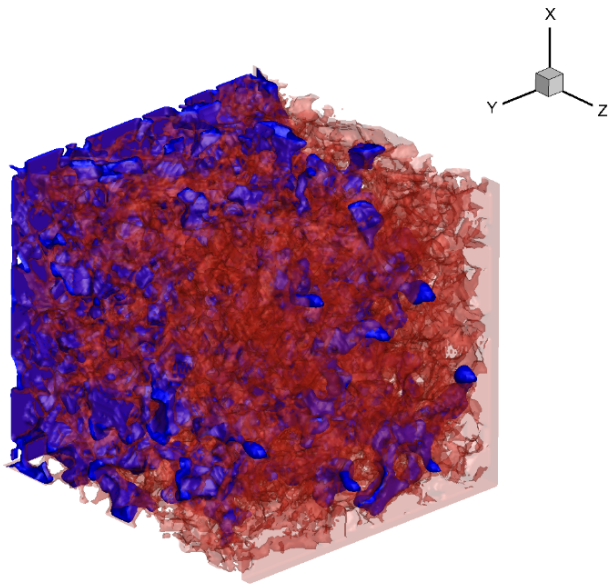

Figure 2.10: CO_2 invasion pattern (blue) computed by the LB simulation for capillary number $Ca = 10^{-4}$ at brine saturation $S_w = 0.50$. Brine is shown in red and rock is not shown.

In order to have a quantitative comparison and consistency check of the results produced by the LB and DNS methods, we compare the dependence of the CO_2 saturation on the distance from the inlet along the direction of macroscopic flow. The results are shown in Fig. 2.11 where CO_2 saturation represents an average taken over the cross-sectional area. The results produced by the two methods follow one another very closely. In addition, we computed the change in the brine saturation in the sample volume over time for the two Ca numbers. The results, shown in Fig. 2.12, indicate again that the two simulation methods provide consistent and closely-agreeing results. This gave us confidence that a comparison between the relative permeabilities produced by the two methods, as well as those produced by the PNM, is viable and meaningful.

Fig. 2.13 compares the spatial distributions of CO_2, injected from left side, and brine for two capillary numbers produced by the DNS, when the latter has reached its residual saturation. Consistent with what is known for the oil-water pairs in porous media, the displacement pattern at high capillary number is more uniform, better connected and piston-like with a lower residual saturation for the brine phase, than that obtained with the lower

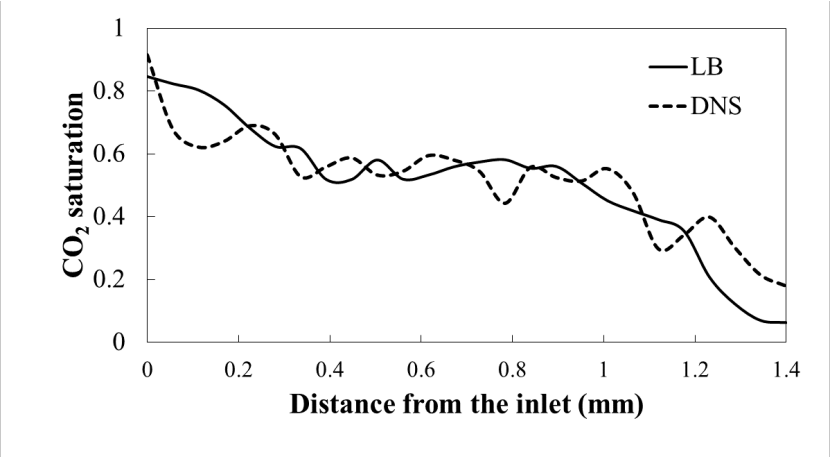

Figure 2.11: Comparison of the computed CO_2 saturation for capillary number $Ca = 1 \times 10^{-4}$ and its dependence on the distance from the inlet at brine saturation $S_w = 0.50$ during drainage.

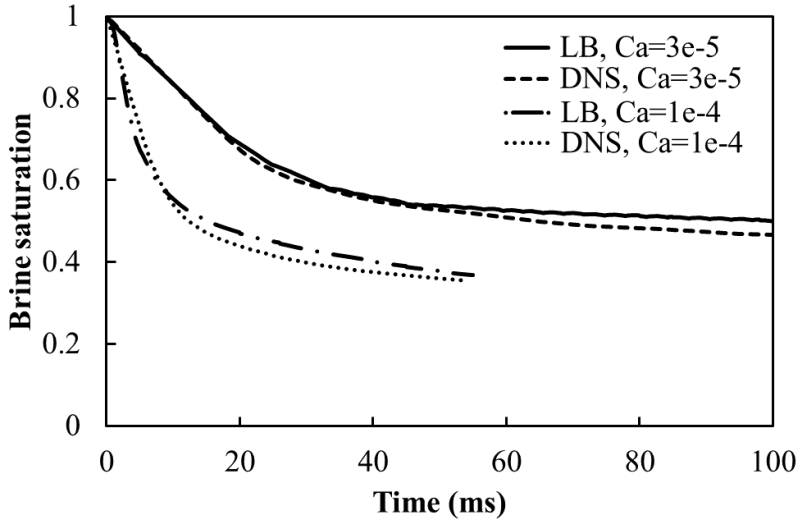

Figure 2.12: Time-dependence of the computed brine saturation obtained by the LB simulation (continuous curves) and the DNS (dashed curves) during drainage.

capillary number that exhibits fingering pattern with a fractal structure. Perhaps, this can be seen better if we consider a side view of the displacement patterns, shown in Fig. 2.14, which are consistent with those shown in Fig. 2.13. Thus, depending on the heterogeneity of the pore space, at lower capillary numbers the capillary fingering effect can be strongly dominant. In that case, there can be some fluctuations in the relative permeabilities, unlike the smoother-varying values for high capillary numbers. It may also indicate that obtaining smoothly-varying relative permeabilities for low capillary numbers entails using larger REVs. Note that at the end of the simulations, the calculated brine residual saturations for the high and low capillary number are 0.30 and 0.50, reached at times 54 ms and 122 ms, respectively.

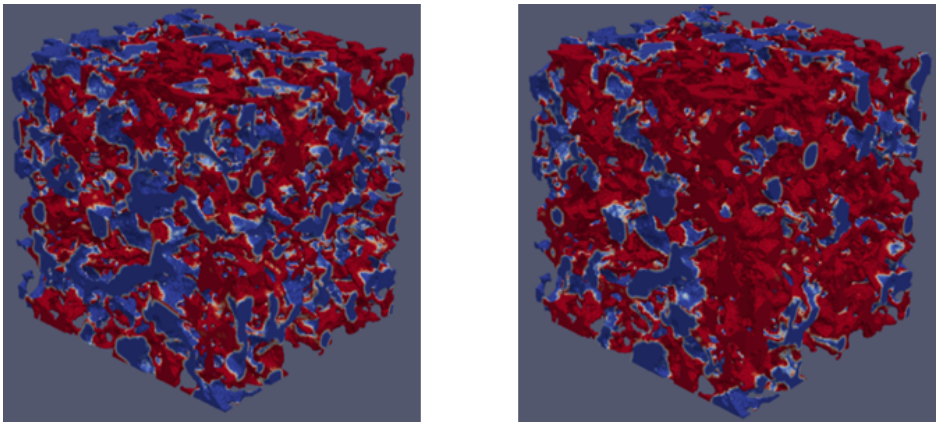

Figure 2.13: 3D representation of the brine residual saturation (red) for $Ca = 1 \times 10^{-4}$ (left) and $Ca = 3 \times 10^{-5}$ (right) capillary numbers. The residual brine saturations are $S_w = 0.30$ and 0.50, respectively, reached at times 54 ms and 122 ms.

In Fig. 2.15, we compare the computed relative permeabilities of the CO_2-brine pair for the lower capillary number that we simulated. All the relative permeabilities computed by the three methods are in good agreement with each other, although the methodologies are completely different. Fig. 2.16 compares the relative permeabilities computed by the LB method and the DNS for the higher capillary number. In this case too, the results are in agreement with each other. Since our PNM simulator is designed for quasi-static displacement by an IP-like algorithm, it could not be used for simulating an arbitrary value of the capillary number when the magnitude of the viscous forces is competitive with the capillary forces. In such case, one must use a dynamic PN simulator (Joekar-Niasar and Hassanizadeh 2012).

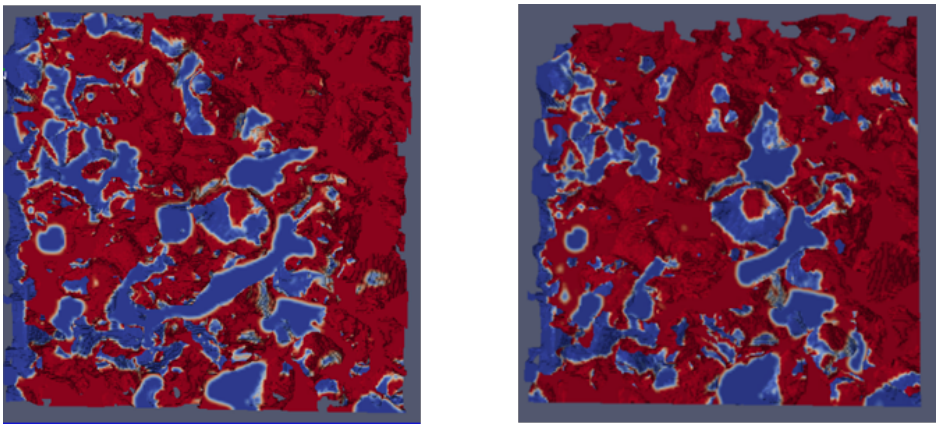

Figure 2.14: Side view (inlet on the left and outlet on the right side of each image) of the distribution of the brine (red) and CO_2 in the pore space for $Ca = 1 \times 10^{-4}$ (left) and $Ca = 3 \times 10^{-5}$ (right) at brine saturation, $S_w = 0.475$.

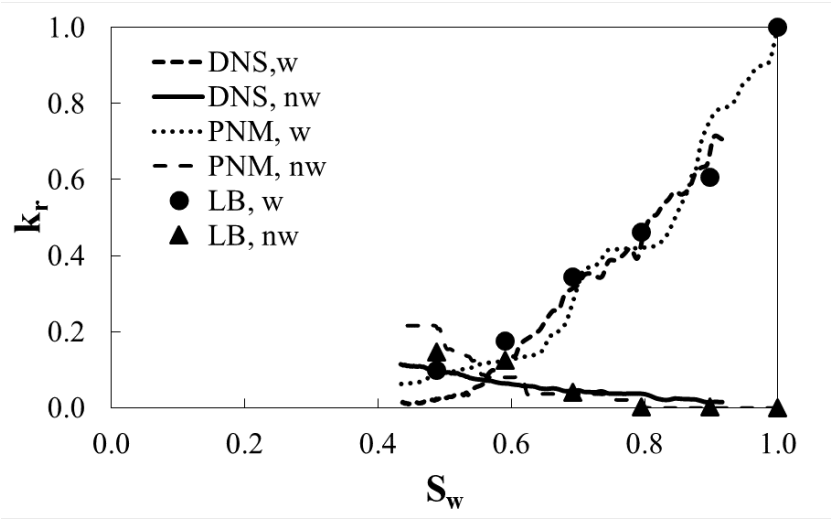

Figure 2.15: CO_2-brine relative permeability curves in low capillary number, $Ca = 3 \times 10^{-5}$.

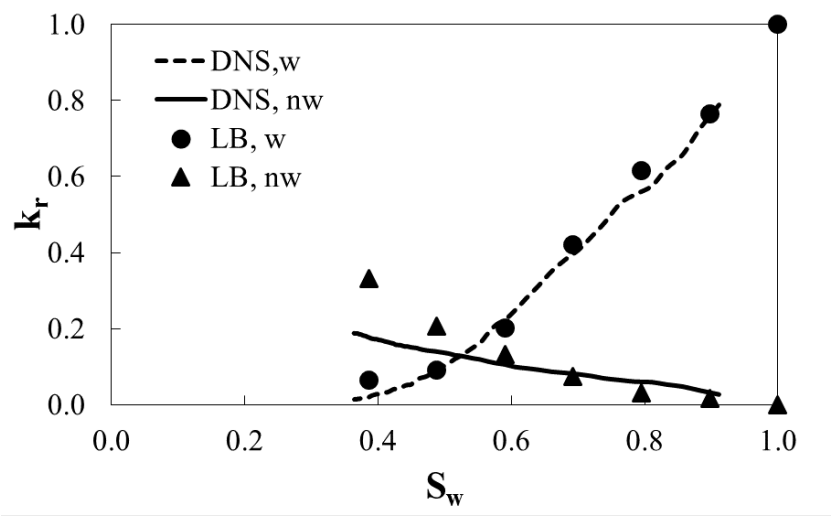

Figure 2.16: CO_2-brine relative permeability curves for high capillary number, $Ca = 1 \times 10^{-4}$.

It should be pointed out that, to compute the relative permeabilities by the LB simulator for each brine saturation, a separate simulation should be carried out, whereas they are computed by one complete simulation when the OpenFOAM poreFOAM package (Raeini et al. 2014) is used in the DNS, as it simulates the entire process, from the beginning of injection of CO_2 to reaching the brine residual saturation. But, if the goal is to compute the quantities of interest for a single saturation, then the LB method is more efficient. The LB method has, however, a problem with spurious velocity, which is resolved in the DNS simulator that we employ in this study by using the FSF approach, instead of the CSF method (see the earlier discussions) to account for the interfacial forces. Note also that the PNM simulation, particularly for low capillary numbers, does not require high-performance computational resources. Thus, it is still a reliable method for low Ca number systems, if the PN used is accurate representation of the pore structure.

2.6 The importance of resolution of the computational grid

An important point should, however, be emphasized. If the LB simulation is used with an image of a porous medium, one must make sure that the resolution of the lattice used is high enough; that is, the results must be

independent of the resolution. For example, in the calculations that we carried out, it was not enough to have one lattice unit per voxel and, thus, the lattice with higher resolutions was needed. Fig. 2.17 compares the results computed by the LB simulation obtained with two lattice resolutions for two Ca numbers. In the low-resolution simulation, one lattice unit was defined for each void space voxel, whereas eight lattice units were utilized for each voxel of the input geometry in the high-resolution simulation. Fig. 2.17 indicates that only when high-resolution lattices are used, do the LB results converge to those obtained by the DNS.

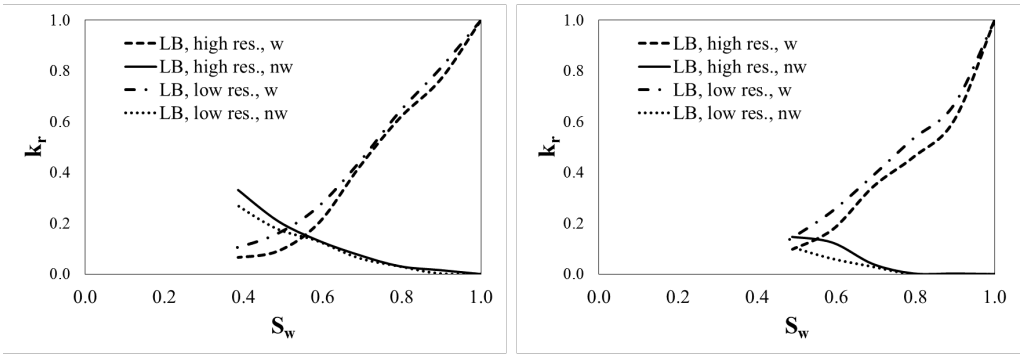

Figure 2.17: Effect of resolution of lattice in LB simulation on the resulting CO_2-brine relative permeability curves for $Ca = 1 \times 10^{-4}$ (right) and $Ca = 3 \times 10^{-5}$ (left).

2.7 Summary and conclusions

In order to study two-phase flow of CO_2-brine in the three-dimensional image of a heterogeneous porous medium, the Mt. Simon sandstone, we first carried out a detailed quantitative study of the pore structure on several subsamples from the rock. Then, we used three distinct computational approaches, namely, the lattice-Boltzmann method, direct numerical simulation of the Navier–Stokes equations, and a pore-network model extracted from the image. The main process simulated was drainage, displacement of brine by CO_2. The relative permeabilities of the two fluids for two capillary numbers were computed and compared. Provided that the computational grid in the DNS and the lattice used in the LB simulation have high-enough resolution, the computed relative permeabilities agree very closely. The DNS

approach requires, however, a single drainage simulation to compute the relative permeabilities over the entire intended range of saturation, whereas the LB approach needs a separate steady-state simulation for each saturation and, therefore, it requires more computational resources. In addition, the difference in the results produced by the DNS and LB may be due to the different formulations used for the capillary forces parallel to the interfaces. The FSF formulation used in the DNS method eliminates non-physical velocities, whereas the CSF formulation employed in the LB simulation results in nonphysical currents, especially in complex geometries. The relative permeabilities computed by the PNM at a low capillary number also agree with those obtained by the LB simulation and the DNS, although the PNM does not need any high-performance computational resources.

Therefore, the question of which method to use for such simulations should be addressed based mainly on the computational time that they need, and the computational resources that one has access too. In addition, one should carefully examine the effect of the resolution of the lattice used in the LB simulation. Improving the interfacial surface formulation in the LB simulation is expected to improve its accuracy, leading to much closer agreement with the results obtained by the DNS method.

Chapter 3

Upscaling

Pore-network stitching method: A pore-to-core upscaling approach for multiphase flow

Pore-network modeling is a widely used predictive tool for pore-scale studies in various applications that deal with multiphase flow in heterogeneous natural rocks. Despite recent improvements to enable pore-network modeling on simplified pore geometry extracted from rock core images and its computational efficiency compared to direct numerical simulation methods, there are still limitations to modeling a large representative pore-network for heterogeneous cores. These are due to the technical limits on sample size to discern void space during X-ray scanning and computational limits on pore-network extraction algorithms. Thus, there is a need for pore-scale modeling approaches that have the natural advantages of pore-network modeling and can overcome these limitations, thereby enabling better representation of heterogeneity of the 3D complex pore structure and enhancing the accuracy of prediction of macroscopic properties. This chapter addresses these issues with a workflow that includes a novel pore-network stitching method to provide large-enough representative pore-network for a core. This workflow uses micro-CT images of heterogeneous reservoir rock cores at different resolutions to characterize the pore structure in order to select few signature parts of the core and extract their equivalent pore-network models. The space between these signature pore-networks is filled by using their statistics to generate realizations of pore-networks which are then connected together using a deterministic layered stitching method. The output of this workflow is a large pore-network that can be used in any flow and transport solver. We validate all steps of this method on different types of natural rocks based on single-phase and two-phase flow properties such as drainage relative permeability curves of carbon dioxide and brine flow. Then, we apply the stochastic workflow on two large domain problems, connecting distant pore-networks and

modeling a heterogeneous core. We generate multiple realizations and compare the average results with properties from a defined reference pore-network for each problem. We demonstrate that signature parts of a heterogeneous core, which are a small portion of its entire volume, are sufficient inputs for the developed pore-network stitching method to construct a representative pore-network and predict flow properties. This chapter is published in the journal of *Transport in Porous Media* (Kohanpur and Valocchi 2020a).

3.1 Introduction

The physics of two-phase flows in heterogeneous natural rocks is relevant to many applications of multiphase flows in porous media such as geological sequestration of carbon dioxide (CO_2), displacements in oil recovery, and contaminant transport. Pore-scale modeling is essential in understanding fundamental phenomena necessary for prediction of macroscopic properties used in field-scale simulation tools. As an example, relative permeability and capillary pressure curves are important inputs of field-scale models to predict long-term displacement of oil or trapping of CO_2 in reservoirs. Although these properties can be estimated from core-scale experiments, these laboratory experiments are difficult to implement, time-consuming, expensive, and have uncertainties in measurements (Joekar-Niasar and Hassanizadeh 2012). Prediction of macroscopic flow and transport properties of rocks based on pore-scale physics has been a focus of many studies (Blunt et al. 2013). Pore-scale models are generally less expensive than experiments and have more flexibility in implementing and changing parameters.

With recent advances in instrumentation and X-ray computed tomography (CT) imaging, one can directly obtain detailed three-dimensional (3D) geometry of rock and its pore structure with high resolution images (Flannery et al. 1987; Dunsmuir et al. 1991; Wildenschild and Sheppard 2013; Andrä et al. 2013a; Andrä et al. 2013b). Such images are inputs of pore-scale models which can be categorized as either direct or simplified models, based on the manner in which they represent the geometry of the void space of porous media. In direct models, multiphase flow and transport equations are solved directly on the exact geometry of pore space obtained from the CT images. Some examples of direct numerical simulation (DNS) methods are

lattice-Boltzmann methods (Boek and Venturoli 2010; Ramstad et al. 2012), finite volume methods (Ferrari and Lunati 2013; Raeini et al. 2014), level set methods (Prodanović and Bryant 2006), etc. The main challenges in using DNS methods are limitations on the size of the domain that is relevant to the grids resolution of simulation and limitations on computational efficiency.

On the other hand, a popular simplified model is pore-network (PN) modeling (Fatt et al. 1956; Sahimi 2011; Blunt 2017) which simplifies the pore space by dividing it into two categories of pore elements: pore-bodies (larger elements for storage of fluids) and pore-throats (narrower elements for flow of fluids). A PN can be either generated from statistics of the pore space, such as pore size distribution, or extracted directly from the 3D image of rock where irregular surfaces and edges of the pore space are abstracted down to simpler geometrical units. There are different PN extraction algorithms in the literature such as medial axis (Lindquist et al. 1996), watershed (Gostick 2017), and maximal ball (MB) algorithms (Silin and Patzek 2006;Dong and Blunt 2009). Defining a PN requires geometrical (location, size, and shape of pore elements) and topological (connections between pore elements) information of the pore space. PN flow models then use some assumptions and approximations to the governing equations on the entire PN e.g., Hagen-Poiseuille equation for flow in pore-throats. More details can be found in Valvatne and Blunt (2004) and Joekar-Niasar and Hassanizadeh (2012). These approximations to geometry and physics make PN models more capable of simulating a representative elementary volume (REV) with less computational effort compare to DNS methods to predict macroscopic properties.

Although PN modeling based on CT images has been applied to different types of porous media, it has been mainly applied on a relatively small volume of an entire core. Current tools face important limitations for attaining a large representative PN of heterogeneous domains. There are both (1) technical limits and (2) computational limits:

- Technical limits: There are technical limits on the size of the core that can be scanned to discern void space well. This is rooted in the trade-off of size and resolution and reflected in both the scanning time and size of produced images (Bultreys et al. 2015). For instance, typical sandstones require few microns (about 2 to 5 μm) of resolution in CT images to be used in pore-scale modeling while typical scans are not

larger than $1000^3 - 2000^3$ voxels with the current micro-CT scanners (Blunt 2017).

- Computational limits: Current PN extraction algorithms are not computationally able to provide a large PN covering all heterogeneities at the core-scale. These algorithms generally scan the entire voxelized pore space and the current codes are written as serial codes. Therefore, their performance is limited in terms of both computational memory and speed that results a limit on the size of their input. For example, current MB network extraction codes cannot attain PNs beyond sizes more than roughly $1500^3 - 2000^3$ voxels.

There are different studies that have addressed some of the challenges noted above by different strategies including multiscale frameworks and domain decomposition approaches in addition to exploiting growing computational capabilities in using current tools.

One common motivation in conducting multiscale studies comes from the practice of investigation of core-scale images (resolution of about $10-30\ \mu m$) of different heterogeneous rocks in terms of spatial variability that shows a wide range of heterogeneities. While such images can reveal some details of the rock such as connectivity of larger pores, they cannot be directly used in pore-scale modeling tools due to lack of enough precision and failure in capturing small channels and pores which are in sub-resolution. However, these images are still able to cover a large domain of the core thereby allowing study of the heterogeneity and spatial variation of the rock properties. They can be used along with pore-scale images in a multiscale framework to study rock heterogeneity that has been addressed in some studies.

Chu et al. (2013) developed a multiscale algorithm with the form of heterogeneous multiscale method that couples PN models with continuum models to predict pressure and track the macroscopic front, although their work was limited to simpler PN models and did not address pore-scale heterogneities. In a PN study, Jiang et al. (2013) combined coarse-scale and fine-scale pore elements to develop a multiscale PN by their stochastic generator for vuggy carbonate rocks. Although this work could cover three-level PNs from different resolutions, it mainly addressed micropores and its accuracy in prediction of two-phase flow properties was not assessed. This approach was continued by Pak et al. (2016) later where they developed an

effective PN integration process to select number and length-scale of input PNs by utilizing experimental pore-throat size distribution. While this approach could combine information from different resolutions to construct a multiscale PNs, it required imaging and PN extraction at all scales and its capability in relative permeability prediction was not studied either. In another multiscale work, Bultreys et al. (2015) developed a dual PN model that incorporates microporosity via adding micro-links to traditional PN models to address the small-scale heterogeneities. While their approach results a great number of pore elements in the constructed PN, it was mainly designed for modeling micropores of heterogeneous samples.

Some other studies have used domain decomposition to deal with the challenges of modeling in large domain problems. Balhoff et al. (2007) used a domain decomposition approach using mortar spaces in which a pore-scale model can be coupled with an adjacent model (pore-scale or continuum) by a 2D finite-element space (Balhoff et al. 2007; Balhoff et al. 2008). The objective of using mortar coupling was to model a more realistic boundary conditions for different neighboring pore-scale models rather than to provide a large representative volume that includes heterogeneities. In another mortar space study, Sun et al. (2012) used a domain decomposition method to upscale absolute permeability on heterogeneous PN models. Also, Mehmani and Balhoff (2014) used a hybrid method for parallel modeling of linear and nonlinear flow across scales in large domains that enhanced the computational efficiency of mortar domain decomposition. These studies successfully bridged the pore-scale to continuum-scale but were mainly validated based on single-phase flow properties and did not involve core-scale heterogeneities. In a different domain decomposition study, Rabbani et al. (2019) connected extracted PNs of subdomains by generating pore-throats between subdomains with different decomposition strategies. While their approach was successful in reducing computational demands of PN extraction, it was mainly focused on PN properties and absolute permeability of homogeneous samples. In a large domain study, Da Wang et al. (2019) used dual grid domain decomposition on a large rock sample with the aid of high performance computing but the work was limited to absolute permeability evaluation.

In a pore-to-core PN modeling work, Aghaei and Piri (2015) studied a long Berea sandstone core to attain a large PN and model capillary and viscosity effects with the aid of heavy parallelization based on domain de-

composition scheme. While this work was notable in terms of the accuracy of prediction of two-phase flow properties and the size of studied sample, the type of rock was relatively homogeneous and the process of connecting sample pieces were specific to that very studied sample. Varloteaux et al. (2013) developed a method to upscale reactive transport from pore to core to reservoir scale. A key part of their workflow is generating a spatially periodic PN from extracted PNs from micro-CT images. They accomplished this by using 3D Delaunay triangulation to add new links to boundary pore-bodies of a homogeneous Fontainebleau sandstone PN and assigned geometric properties of links randomly from statistics inside the PN. While this approach bears some relation to the layered stitching of the method we develop here, its main purpose is to modify connectivity at the boundaries of PN rather than construction of large heterogeneous PNs, which is the aim of our developed method presented here. In a recent pore-to-core PN modeling study, Zahasky et al. (2019) characterized centimeter-scale Bentheimer sandstone cores by studying heterogeneity in capillary pressure and relative permeability with the aid of an extensive multiple resolution imaging. In addition, Jackson et al. (2019) used multiscale experimental and modeling approaches to study two large Bentheimer sandstone cores. Although these works were notable in terms of providing a unique data set and addressing heterogeneity and size of the domain, they rely on full micro-CT images of an entire core with a fine resolution which may not always be readily available and requires relatively large computer storage.

Therefore, there is still a need for pore-to-core upscaling approaches that can accurately represent the 3D complex pore structure and heterogeneity of real media with efficient computational demands and incorporate information from multiple scales. Herein, we introduce a novel pore-network stitching method [1](PNSM) to provide large-enough representative PN for a core that encompasses a larger scale of heterogeneities than is possible using conventional PN modeling and other pore-scale modeling approaches while it is still computationally efficient. Some highlights of this method were originally presented in Kohanpur and Valocchi (2018) and Kohanpur and Valocchi (2019).

The organization of the rest of this chapter is as follows. Section 3.2

[1]The source code is available at: github.com/amirkohanpur/pn-stitcher

will explain the overall workflow, steps, and tools used in the PNSM. In Section 3.3, the main steps of this method, layered stitching and volumetric stitching, are validated for computing flow properties on different types of rock samples. The main application of the PNSM for larger domains is presented in Section 3.4 where spatially separated PNs are connected together and a large heterogeneous sample is modeled from the information of its signature parts. We compare single-phase and two-phase flow properties of a stitched PN with properties from a defined reference PN for each study. Finally, the conclusions are summarized in Section 3.5 and the developed software of PNSM is explained in Section 3.6.

3.2 Method

As mentioned earlier, the motivation for developing the PNSM comes from investigation of core-scale images of heterogeneous rocks that can represent an entire cross section of a core along its length. For example, Fig. 3.1 shows a cross section of a heterogeneous Mt. Simon sandstone core with a diameter of 2 inches at a depth of 7034 feet. The formation is located at verification well number 2 of Illinois Basin-Decatur Project (Finley 2014) where Illinois State Geological Survey carried out a pilot CO_2 injection study. The core plug from the formation was scanned by industrial CT scanning at the National Energy Technology Laboratory (NETL) of the U.S. Department of Energy. The marked red boxes in Fig. 3.1 are some distinct regions or heterogeneities of the core that characterize the overall variability. In general, these regions can be found in 3D images of the core at different depths but here we use this 2D image to explain steps taken in the workflow more intuitively.

The first step is to examine the entire coarse resolution scans of the core to find unique size and shape of solid grains and local pore structure in different locations and identify heterogeneities. Assessment and integration of multiple scales of 2D and 3D micro-CT images can be used to investigate geometry, connectivity, and heterogeneity of pore space (Long et al. 2013). This procedure might be tedious and subjective but it is an important step in the workflow. It can be doubled-checked by applying a fast evaluation of pore size distribution on multiple 2D images (Münch and Holzer 2008) from

different selected depths where larger pores can still be identified in coarse resolution images and most heterogeneities can be captured. The outcome of this analysis is identification of selected locations of the core that are unique in terms of pore size and structure that are defined as signature parts, as shown with red boxes in Fig. 3.1. The hypothesis is that these signature parts, which might or might not be adjacent, are sufficient to represent the heterogeneity of the core.

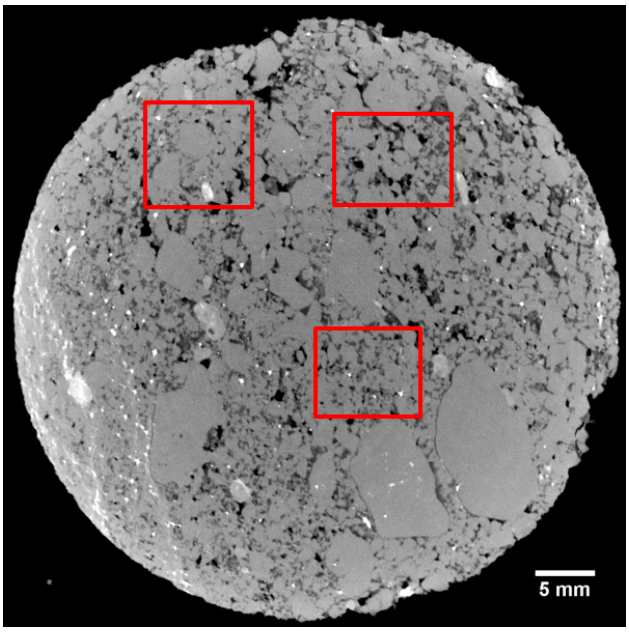

Figure 3.1: A coarse-scale scan of a Mt. Simon sandstone sample at a depth of 7034 feet from the Illinois Basin Decatur Project.

As depicted in Fig. 3.2, the next step after identifying signature parts is to obtain their fine resolution scans, 3D micro-CT images, in order to characterize their pore structure. These micro-CT images are used as inputs to a PN extraction tool that obtains the PNs for each signature volume. These extracted PNs also include key statistics of the pore space such as pore size distribution and connectivity. Tahmasebi and Kamrava (2018) has also proposed a similar approach of integrating information from coarse and fine resolution images in which they construct a multiscale PN by adding stochastically generated micro-PNs to extracted macro-PNs. In this workflow, we use the PN extraction code based on MB algorithm from Dong and Blunt (2009). The algorithm was originally introduced by Silin and Patzek (2006) where the entire 3D voxelized pore space is searched to find the largest

possible spheres, and subsequently, was extended and modified in later works such as Al-Kharusi and Blunt (2007), Dong and Blunt (2009), and Raeini et al. (2017). The Dong and Blunt (2009) PN extraction code can provide inherit randomness of pores and channels in real rocks with a wide range of connection number for pore-bodies. On the other hand, the currently available code is not computationally parallelized and is limited by the size of input rock images. It tends to result too many small pore-throats around the voxel size of images (Dong 2008). In addition, the cut-off between pore-bodies and pore-throats is arbitrary (Blunt 2017) and its pore-throats on the inflow and outflow boundaries are generated randomly rather than being derived from rock images. Despite these shortcomings and limitations, it is used extensively in the literature and has successfully characterized various rocks and predicted their flow properties. The code writes its outputs that is, the information specifying the extracted PN, in StatOil format (Sochi 2007), a commonly used data structure that is also used elsewhere in the PNSM workflow.

The input of this algorithm is the voxelized binarized (solid as one and pore as zero) geometry of the rock where all the zero voxels are scanned. The largest possible voxelized sphere for each pore voxel is determined and taken as the MB. In practice, most of MBs are removed since they are completely inside the larger MBs. The resulting MBs are sorted and clustered based on their volume that helps identifying the ancestor MBs and a chain of the MBs that are from one ancestor to another one. Each chain is segmented as a configuration of two pore-bodies and their connecting pore-throat (Dong and Blunt 2009). The extracted PN is defined when all pore-bodies and pore-throats are identified in the entire volume of zero voxels.

Finally, the algorithm assigns indices to pore-bodies and pore-throats separately that is used for storing topological information, i.e., connections between pore elements. In addition, geometrical information of pore elements are stored including the location, radius, volume, length, total length, and shape factor. The shape factor is a metric of irregularities of the pore space in pore elements and defined as $G = VL/A^2$, where A is surface area, V is volume of the voxelized element, and L is twice the distance between the center of the ancestor MB and the farthest voxel in that MB (Dong and Blunt 2009). The shape factor is also a key quantity that helps assigning familiar geometries (such as circles, squares, and triangles) to the cross sections of

the pore elements to be used in the PN flow models (Patzek and Silin 2000). We use statistics of geometrical and topological information of pore elements in the signature PNs in this workflow.

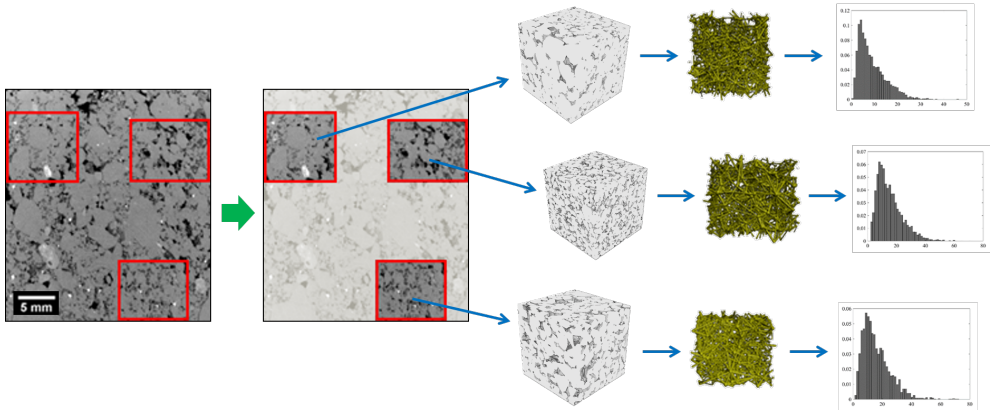

Figure 3.2: Signature parts of the core are selected and their corresponding micro-CT scans, extracted pore-networks, and statistics are derived.

Since the space between signature PNs in the core can be relatively large and cannot be directly extracted, the next important step of the workflow is to fill the space between signature PNs by new defined pore elements. We accomplish this by using statistics of the signature PNs and a stochastic algorithm to generate new PNs in the empty regions of the domain. We then develop a new PN stitching algorithm to link adjacent PNs. The final result of the workflow are multiple realizations of a large PN for the entire core volume that represents the heterogeneity identified in the different signature parts. Fig. 3.3 summarizes the path from signature parts of the core to generate new pore elements in the empty region of the domain and construct a large PN as the output that includes both extracted and generated pore elements.

We explain the two main tasks, namely, defining a layer of pore elements linking neighboring PNs and generating an entire PN in empty regions of the domain in Sections 3.2.1 and 3.2.2, respectively.

3.2.1 Layered stitching

The goal in layered stitching is to connect two neighboring PNs by a layer of pore elements that can be in the direction of flow (longitudinal) or

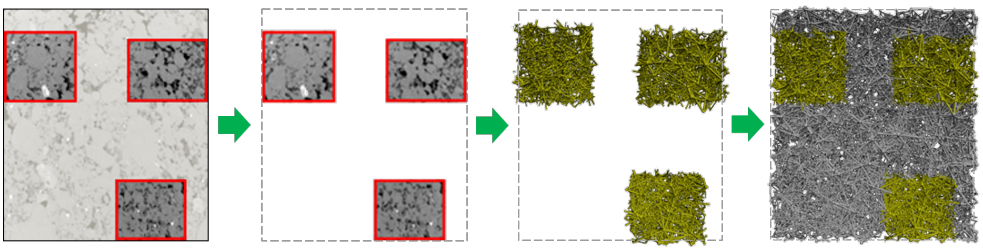

Figure 3.3: Signature pore-networks of the core are used to generate new pore elements in the empty region of the domain and construct a large stitched pore-network.

transverse directions to the flow (lateral). A layer of pore elements signifies that the thickness of layer is in the range of average pore-throat length as opposed to an entire volume of PN. This step is functionally similar to domain decomposition approach using mortar spaces, since the purpose is to connect two adjacent PNs. We will explain the details by considering longitudinal stitching of left and right PNs together, as shown Fig. 3.4, where the flow direction is from left to right in the flow model.

Initially, the algorithm reads in all information of the left and right PNs, represented in yellow in Fig. 3.4, including: index, location, radius, length, shape factor, volume, connectivity, and inlet and outlet status of all pore-bodies and pore-throats. The next step is to remove outlet pore-throats of left PN and inlet pore-throats of right PN based on the flow direction assumption. This affects the inlet and outlet status of corresponding pore-bodies in those locations. The stitching layer includes interconnected pore-bodies and pore-throats which are connected to the left and right PNs, as represented in green in Fig. 3.4. The thickness of the stitching layer is based on the summation of average pore-throat length of both PNs. Pore-bodies in the stitching layer are defined first where their centers are initially located on a regular 2D lattice pattern proportional to dimensions of the cross section and followed by a random perturbation in 3D space. To assign the number of pore-bodies in the stitching layer, density of pore-bodies (number of elements per the box volume) for each PN is calculated and their arithmetic mean is computed. Then, by multiplying this average density by the thickness and area of the the stitching layer, one can obtain the corresponding number of pore-bodies in the stitching layer. In this way, it is guaranteed that no two pore-bodies intersect and they are not too close to each other, otherwise it could yield

extremely short pore-throats in the vicinity of the stitching layer which is not realistic and may affect the resulting flow through the layer.

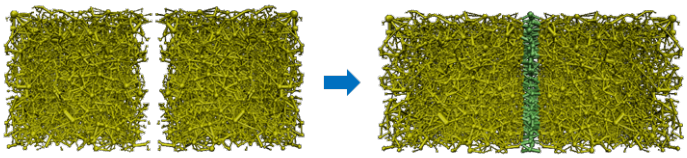

Figure 3.4: Layered stitching of two adjacent pore-networks by generating a layer of pore elements.

In the next step, the generated pore-bodies of the stitching layer need to get connected to each other and nearby pore-bodies in both PNs, i.e., generating pore-throats of the stitching layer. To do so, initially all possible connections up to mean pore-throat length plus two standard deviations are generated. This is a defined limit to ensure generating enough pore-throats based on the available pore-throat length information in both PNs. Then, we remove some connections randomly to achieve a determined number of pore-throats in the stitching layer which is the arithmetic mean of density of pore-throats from both PNs. This mean value involves both the number of pore-throats and the volume of PNs to reduce redundant generated pore-throats in the stitching layer. However, it is also important to investigate the average connection number of the final stitched PN and compare it with the arithmetic mean of the original PNs. The importance of average connection number of a PN and its effect on flow properties have been demonstrated in many studies (Fenwick and Blunt 1998; Raoof and Hassanizadeh 2010). Therefore, a further step of adding or eliminating some pore-throats in the stitching layer is applied to get the average connection number within a threshold of the arithmetic mean of left and right PNs. The random elimination procedure to attain a certain connection number is also used in other PN modeling studies, such as Raoof et al. (2013) and Varloteaux et al. (2013). These criteria and averages are employed in the stitching layer to achieve a smooth transition between left and right PNs in terms of connectivity and length of pore-throats. While other averaging formula can also be used, we will demonstrate the layered stitching with this approach on different rock samples in the next section.

After defining number and location of pore elements and their connections

in the stitching layer, their corresponding radius, shape factor, and volume need to be determined. To do so, we add distributions of left and right PNs for each property by combining their histograms and fitting a proper distribution function such as normal, log-normal, and Weibull distributions. These distributions are also used in other PN modeling works such as Valvatne (2003). While we can choose different combinations of these distributions and evaluate the best one based on final resulting flow properties, we assign default distributions for each property in the workflow coming from studying a wide range extracted PNs from different types of rock. Based on our analysis, the Weibull distribution is a better candidate for radius and volume and normal distribution for shape factor of pore elements in most of studied cases, so these are the default distributions in our developed code.

The explained procedure is applicable when the defined layer of pore elements is normal to the main flow direction. On the other hand, a similar strategy can be applied when the two neighboring PNs are stitched together in the lateral direction which is parallel to the main flow direction. In such case, we define the stitching layer with just generated pore-throats coming from average statistics of both PNs and no pore-bodies are generated in the lateral direction. In this way, we mark all pore-bodies of both PNs in the vicinity of stitching layer (e.g., within the 10% of lateral length) and generate all possible connections. Then, we apply a similar removal approach to achieve a determined number of pore-throats in the stitching layer based on considering arithmetic mean of density of pore-throats and average connection number of both PNs. The radius, shape factor, and volume of these generated pore-throats are also determined by fitting a proper distribution function as discussed for longitudinal layered stitching.

Thus, the size and connectivity of the layer of pore elements in longitudinal and lateral directions are influenced by the statistics of the two adjacent PNs. We implement the stitching layer as a deterministic approach to reduce complexity, albeit a smooth connection between adjacent PNs should be achieved and tested in terms of resulting flow properties. In Sections 3.3.1 and 3.3.2, both longitudinal and lateral stitching procedures are validated on several samples, respectively.

3.2.2 Volumetric stitching

If the signature PNs are not neighbors in the domain, which is usually the case, layered stitching would not be sufficient to connect them and another way of generating pore elements in the empty volume of the domain is needed that we call volumetric stitching. We use PN generators to have similar box-size PNs and place them in empty spaces including the vicinity of signature PNs as shown in Fig. 3.5. This approach allows using available PN generators in the literature, such as the stochastic network generator developed by Idowu and Blunt (2010), which we have used in this workflow.

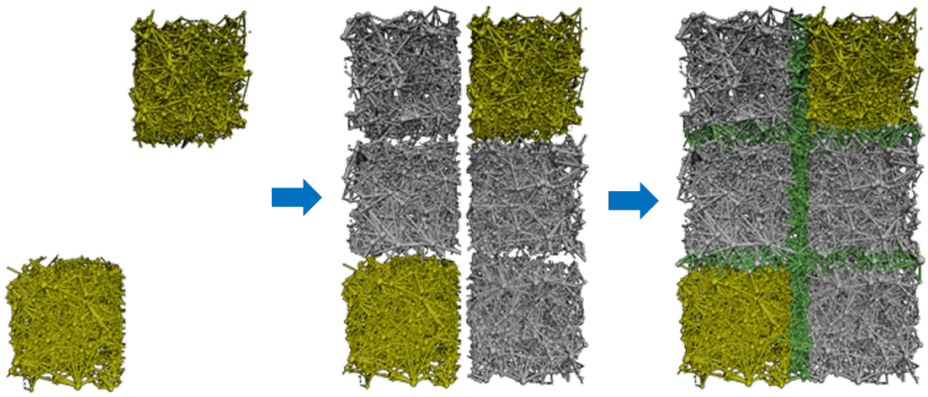

Figure 3.5: Volumetric stitching of two distant pore-networks by generating pore elements in the empty region and linking all pore-networks by layered stitching.

This generator utilizes detailed statistics of pore elements as input data and results a generated PN in the same format as an extracted PN from MB algorithm. To be more specific, the required input data are distributions of pore-body radius and volume, connection number, pore-throat radius and volume, pore-throat length, and pore-throat total length along with their associated indices. The generator assigns locations of all pore-bodies randomly first and, then it reconciles pore-throat lengths and connection numbers to generate pore-throats between pore-bodies. Thus, the resulting locations of pore-elements and statistics of pore-throats are stochastic and varies across realizations. As a result, the output is a stochastic generated PN and sufficient number of realizations must be generated for any analysis. More details can be found in Idowu and Blunt (2010).

We tested this generator on various PNs coming from different rocks and observed that it sometimes fails to keep the connectivity of source statistics in the generated PN, and therefore, underestimates permeability. To fix this issue, we have added a modifier after generating PNs to check the weighted average connection number (a metric that describes size and connectivity of PN together) and adjust the pore-throat size distribution. In this way, some of the generated realizations are rejected if their weighted average connection number is not within the 10% of the weighted average connection number of source data. Fig. 3.6 shows an example of pore-throat size distribution of an accepted realization of generated PN compared with the original PN from a Mt. Simon sandstone sample that its statistics are used as the source data.

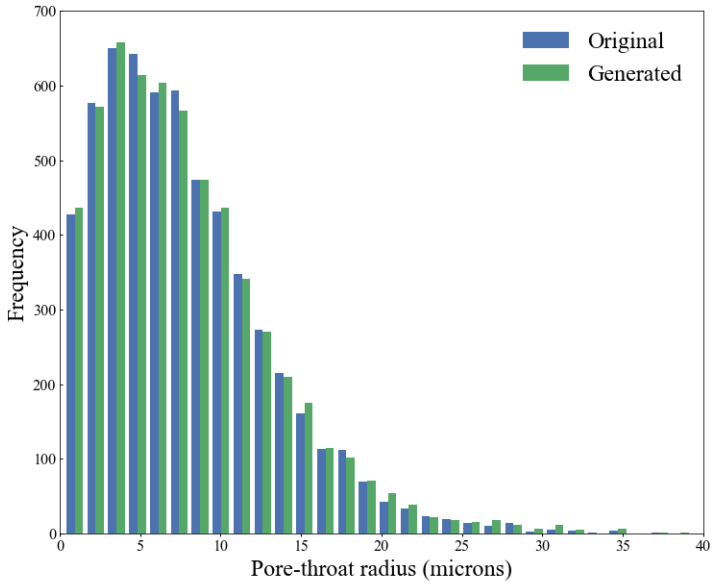

Figure 3.6: Comparison of pore-throat size distribution of a generated pore-network with its original pore-network from a Mt. Simon sandstone sample.

The explained selective approach in PN generation leads to better realizations of generated PNs for filling the empty regions of the domain. The statistics of the generated PNs should be derived from those of nearby signature parts. One such approach would be to use parameters (e.g., mean, variance) of derived fitting distributions. We accomplish this by concatenating the pore element lists (pore-body radius and volume, connection number, pore-throat

radius and volume, pore-throat length, and pore-throat total length) for all signature PNs with a weight for each based on their relative center-to-center distance to the generated PN, i.e., the closer to a signature PN, the more it is influenced by its statistics. The advantage of this way is twofold. First, we can easily honor the intrinsic correlation among geometrical properties of a pore element such as radius, length, volume, etc. by picking them as a set as opposed to considering separate distributions and then matching correlations. This leads to having more realistic pore elements. Second, we can relate the weighted average to all signature PNs of the entire domain simultaneously and thus, the footprint of their statistics can be found in every single generated PN of the domain.

Once all empty spaces are filled with generated PNs, we use the layered stitching in longitudinal and lateral directions to connect all PNs together as shown in Fig. 3.5. Therefore, the stochastic PN generation is coupled with layered stitching to create a large stitching volume to implement volumetric stitching and connect signature PNs that might be in distant locations in the core. It should be emphasized that the combination of stochastic PN generation and deterministic layered stitching results a stochastic process for volumetric stitching.

An important challenge in the described workflow that happens in most of steps is to sort and relate indices of pore-bodies and pore-throats. This is because each of the signature and stitching PNs has its own order indices of pore-bodies and pore-throats initially but they need to to be modified and reordered by any removal and addition of pore elements. The goal of having a final unified PN requires having one single set of indices for all elements in the final stitched PN. Moreover, the connection number of pore-bodies can change with any removal and addition of pore-throats and pore-bodies; that requires updating and matching indices in the connectivity information of the final unified PN as well.

In summary, the introduced steps together form a workflow to deal with large domain problems that starts with identifying signature parts and having their 3D images. PN extraction is used, and the resulting statistics are used in layered stitching and PN generation to fill empty spaces of the domain. The outcome is that all signature and generated pore elements interconnected in a large unified PN that can be used in flow simulation and other PN applications.

3.3 Validation

In order to validate the introduced PNSM and its specific steps of stitching explained in Section 3.2, various test cases of flow simulations are carried out on different types of rocks. For this validation, six cubic rock samples (four sandstones and two carbonates) are chosen from different studies in the literature; the samples are listed in Table 3.1 with their size, image resolution, porosity, and a chosen label.

Table 3.1: Selected samples for validating steps of the pore-network stitching method

Sample	Label	Porosity	Res. (μm)	Size (mm^3)	Study
Berea sandstone	BR	0.208	3.20	1.28^3	Jiang and Tsuji (2014)
Bentheimer sandstone	BN	0.188	3.18	1.59^3	Herring et al. (2016)
Mt. Simon sandstone	MH	0.261	2.80	1.40^3	Kohanpur et al. (2020)
Mt. Simon sandstone	ML	0.097	1.95	1.56^3	Tahmasebi et al. (2017)
C1 carbonate	C1	0.233	2.85	1.14^3	Dong and Blunt (2009)
C2 carbonate	C2	0.168	5.35	2.14^3	Dong and Blunt (2009)

We carry out single-phase and two-phase flow simulations for different steps of the PNSM on these six samples. As our original motivation was to study geological storage of CO_2, the CO_2-brine flow system (see Table 3.2 for the properties) is used for the two-phase flow simulations, and we use a quasi-static PN flow solver (Valvatne and Blunt 2004) to study its capillary-dominated physics. In each validation study, the stitched PN is compared with a similar-size reference PN that is constructed by connecting 3D image of the original sample to its mirrored geometry along the intended stitching direction.

For single-phase flow properties, we report absolute permeability of all six samples here. For two-phase properties, we just report the results from the Mt. Simon sample (MH) here which its raw and segmented 3D images are available at Kohanpur et al. (2019). This sample has a fairly high porosity and is more heterogeneous with respect to typical well-studied sandstones in

Table 3.2: Properties of CO_2-brine flow system in pore-network two-phase flow simulations

Properties	Value	Unit
Interfacial tension	30	mN/m
Contact angle	25	$^\circ$
Brine density	280	$kg/m3$
CO_2 density	992	$kg/m3$
Brine viscosity	0.550	cp
CO_2 viscosity	0.023	cp

the literature such as Berea and Bentheimer. Since the sample is from the reservoir that has been used in a pilot CO_2 sequestration project in Illinois (Finley 2014), its CO_2-brine flow properties are extensively studied recently by different numerical pore-scale models (Kohanpur et al. 2020). We use subsample S2 from that study, labeled MH in Table 3.1 and shown in Fig. 3.7, to validate each step of the PNSM. The full results on other samples of Table 3.1 are available in Appendix A of this dissertation and reported in Kohanpur and Valocchi (2020b).

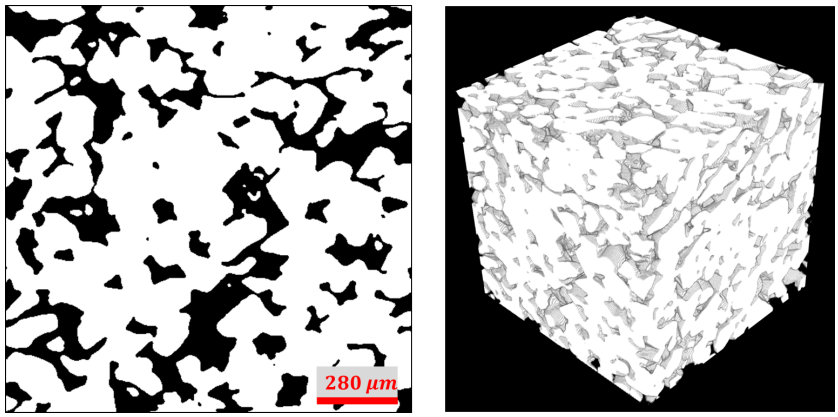

Figure 3.7: The Mt. Simon sandstone sample: (left) the segmented image of the first slice of the stack and (right) the 3D reconstructed geometry of the rock.

3.3.1 Longitudinal layered stitching

In order to validate the layered stitching in longitudinal direction (along the main flow direction), the original sample is considered as the left sample and its 3D image is mirrored longitudinally to obtain the right sample. Con-

necting left and right samples in the voxelized domain forms the extended sample as shown in Fig. 3.8. By applying PN extraction algorithm on 3D images of these samples, one can get left, right, and extended PNs as depicted in Fig. 3.8.

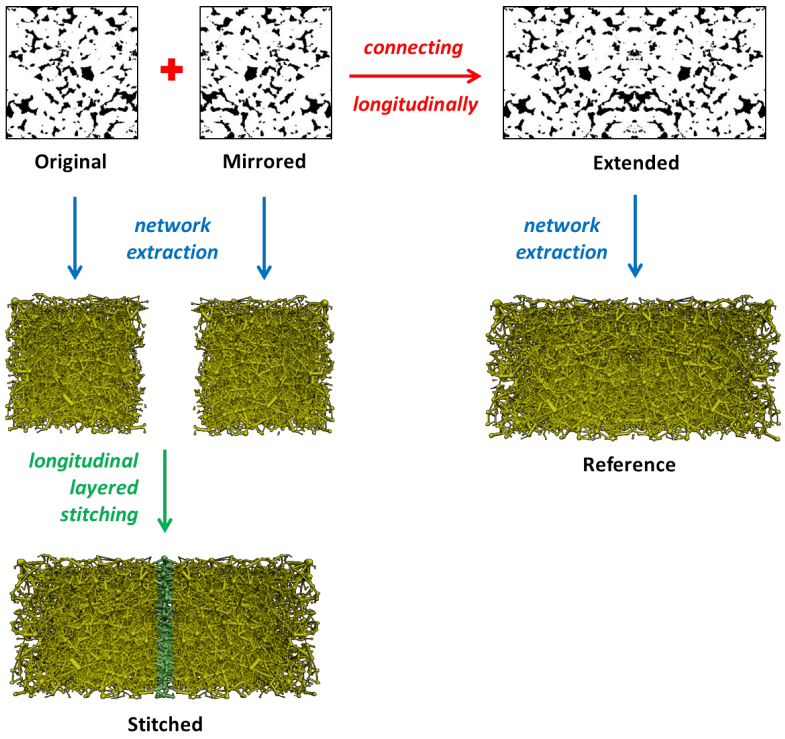

Figure 3.8: Longitudinal layered stitching of a Mt. Simon sandstone sample to its mirrored geometry and its corresponding reference sample.

While the extended PN is used as the reference PN, left and right PNs are stitched together using the longitudinal layered stitching described in Section 3.2.1. The stitched and reference PNs are then used as input PNs of the quasi-static PN flow solver (Valvatne and Blunt 2004) with the same input properties to be compared.

The predicted absolute permeability of all samples are compared in Fig. 3.9 where horizontal and vertical axes refers to predicted absolute permeability of the reference and stitched PNs, respectively. All samples have results that are quite close to the diagonal line, thus providing confidence in the longitudinal stitching algorithm across a variety of rock types. Regarding two-phase flow properties, Fig. 3.10 shows excellent agreement for drainage relative permeability curves between the stitched and reference PNs of sample MH.

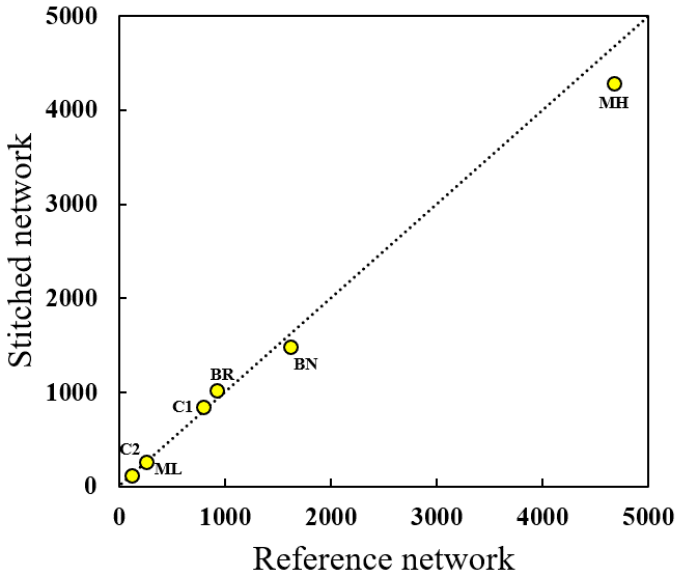

Figure 3.9: Comparison of absolute permeability of reference pore-network with the resulting stitched pore-network via longitudinal layered stitching for all six selected samples.

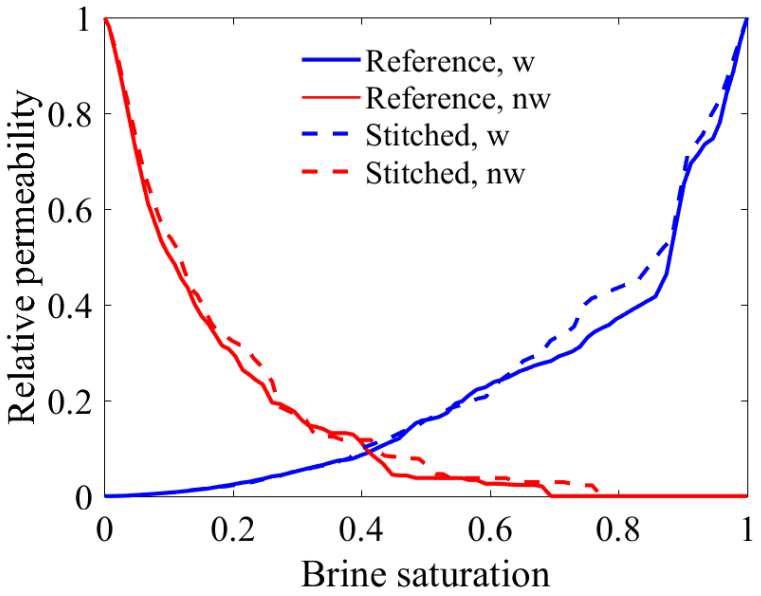

Figure 3.10: Comparison of relative permeability curves of the stitched pore-network from the Mt. Simon sandstone sample (MH) via longitudinal layered stitching with its reference pore-network.

3.3.2 Lateral layered stitching

As explained in Section 3.2, stitching in the lateral direction is implemented slightly differently from that in the longitudinal direction, adding only pore-throats between PNs. For this validation, the 3D image of the original sample is mirrored laterally and connected to itself to obtain a laterally extended sample as shown in Fig. 3.11. The PN extraction algorithm is applied on all these pieces to get original, mirrored, and reference PNs as depicted in Fig. 3.11.

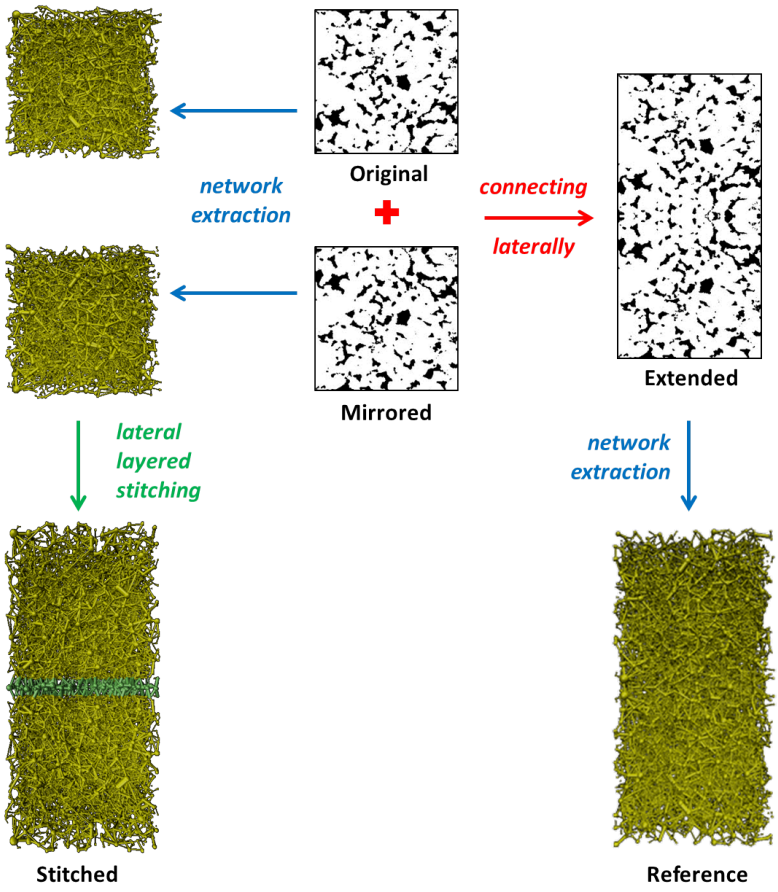

Figure 3.11: Lateral layered stitching of a Mt. Simon sandstone sample to its mirrored geometry and its corresponding reference sample.

The original and mirrored PNs are stitched via lateral layered stitching explained in Section 3.2.1 to be compared with the reference PN based on flow properties. The predicted absolute permeability of all samples are compared in Fig. 3.12. The results are all close to the diagonal line again, which means a good accuracy of lateral layered stitching across these six samples.

Fig. 3.13 presents the comparison of drainage relative permeability curves of stitched and reference PNs from sample MH that shows excellent agreement.

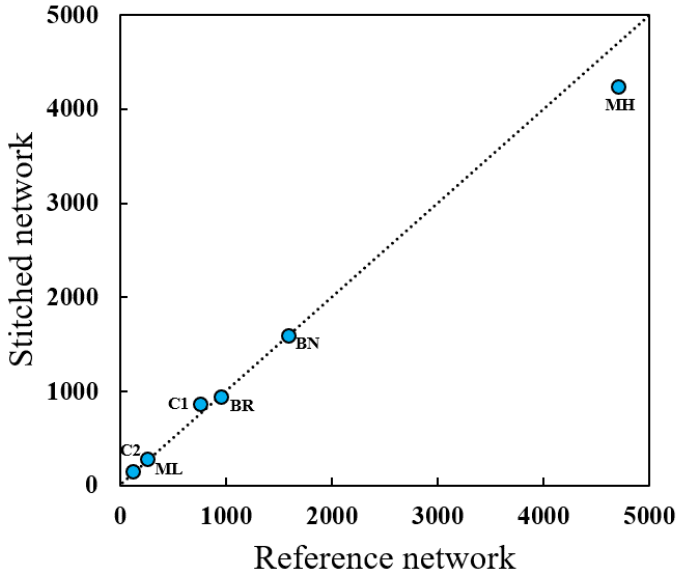

Figure 3.12: Comparison of absolute permeability of reference pore-network with the resulting stitched pore-network via lateral layered stitching for all six selected samples.

Although longitudinal and lateral layered stitching are contributing a small fraction of pore elements in the final stitched PN, the quality of defining new pore elements from the statistics is crucial in terms of connectivity and the resulting flow properties of the stitched PN.

3.3.3 Volumetric stitching

After ensuring that layered stitching works smoothly in both longitudinal and lateral directions, it is also necessary to investigate the performance of volumetric stitching where an entirely new PN and stitching layers are generated in the domain. As discussed in Section 3.2 because the utilized PN generator is a stochastic tool, the volumetric stitching is also stochastic tool, and this needs to be reflected in the evaluation of properties. Fig. 3.14 shows the defined problem to evaluate flow properties of the stitched PN via volumetric stitching. The extended geometry along the main flow direction can still be used as the reference PN while the mirrored sample is replaced

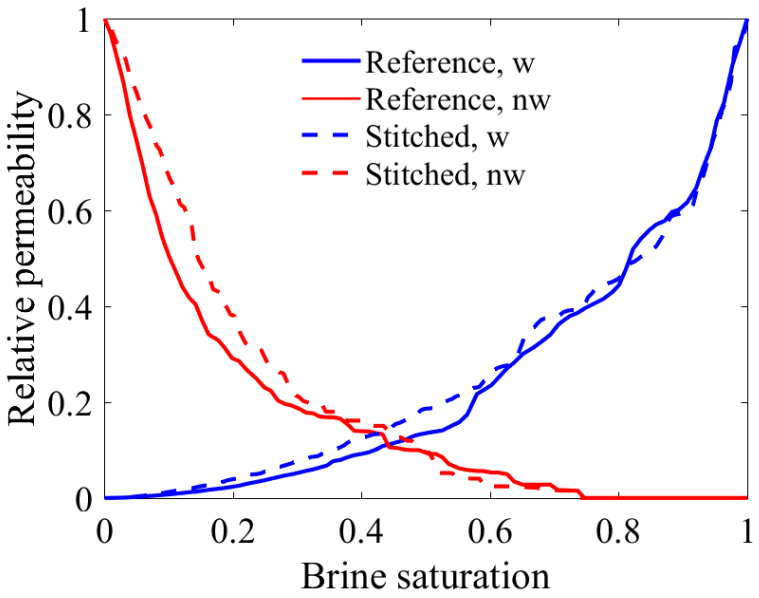

Figure 3.13: Comparison of relative permeability curves of the stitched pore-network from the Mt. Simon sandstone sample (MH) via lateral layered stitching with its reference pore-network.

by a generated PN. Then, longitudinal layered stitching is applied to link the original and generated PNs to obtain one realization of the stitched PN via volumetric stitching.

We have carried out volumetric stitching with 10 realizations on each sample listed in Table 3.1. Fig. 3.15 shows the arithmetic mean and range of the resulting permeability of each sample compared with its reference PN. Since the approach is stochastic, it is possible that some realizations will be outliers in terms of computed flow properties. However, the mean over the 10 realizations is close to the diagonal line, showing good agreement with the reference PN.

To assess the resulting relative permeability curves, we compare the mean of realizations with the reference PN curves. We have obtained this by taking the arithmetic mean at each saturation point. Figs. 3.16 and 3.17 show drainage relative permeability of CO_2 and brine, respectively, for 10 realizations along with their mean compared with the reference curve. The predicted relative permeability of both phases show good agreement between stitched PN and reference PN curves. Relative permeability curves from other samples are reported in Appendix A.

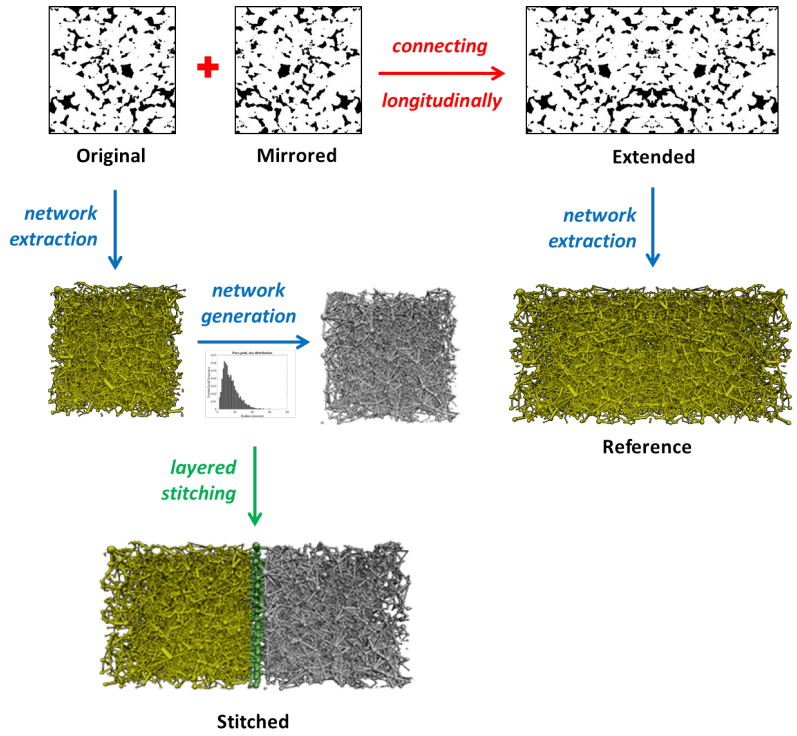

Figure 3.14: Lateral layered stitching of a Mt. Simon sandstone sample to its mirrored geometry and its corresponding reference sample.

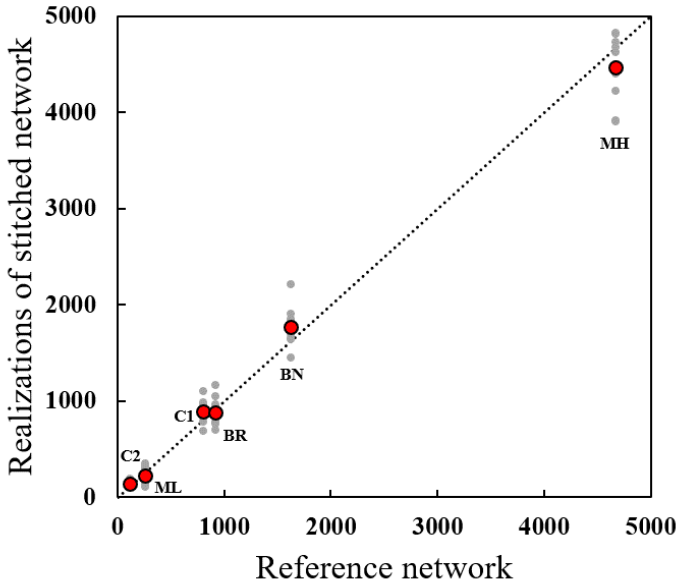

Figure 3.15: Comparison of absolute permeability of reference pore-network with the resulting realizations of stitched pore-network and their mean via volumetric stitching for all six selected samples.

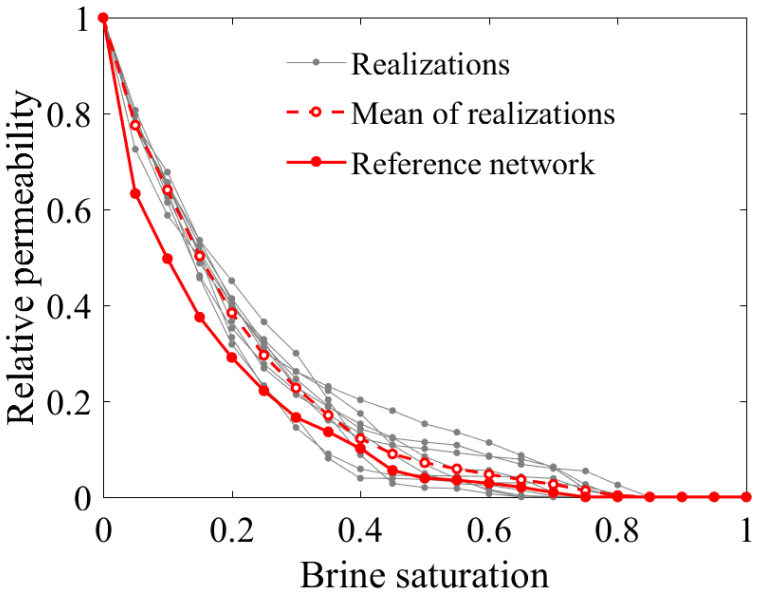

Figure 3.16: Comparison of CO_2 relative permeability of 10 realizations of stitched pore-networks from the Mt. Simon sandstone (MH) sample via volumetric stitching with their reference pore-network.

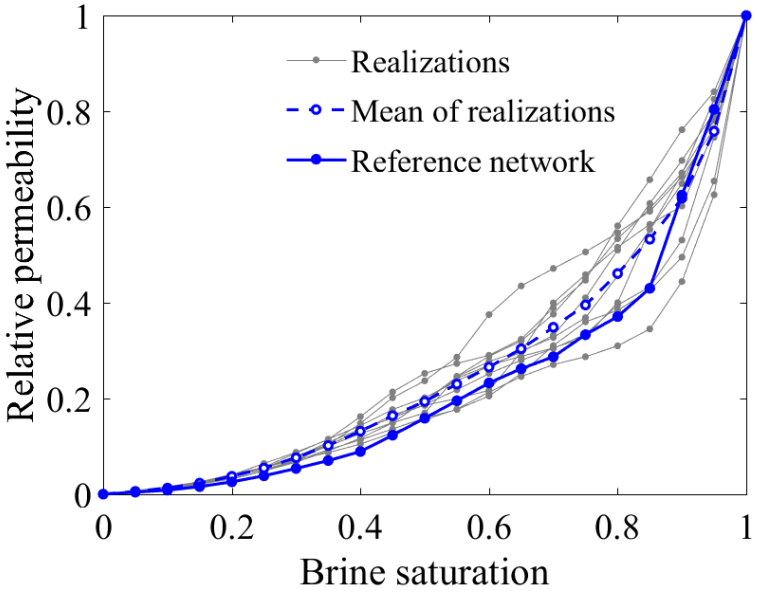

Figure 3.17: Comparison of brine relative permeability of 10 realizations of stitched pore-networks from the Mt. Simon sandstone (MH) sample via volumetric stitching with their reference pore-network.

It should be emphasized that this stochastic approach is feasible because PN generation and stitching are computationally efficient and quasi-static PN solver is a also fast predictive tool.

3.4 Results and discussion

In this section, we use the PNSM on two different defined problems with large domains relative to conventional pore-scale studies. The first problem considers two distant samples in the flow direction with different properties where the space between them is filled with new pore elements based on combined statistics of their PNs. The second problem is for a large heterogeneous 3D sample where three small signature parts are used to construct a large representative PN and compute flow properties. The focus of the first problem is to combine different PN statistics to generate an average PN in the empty space in between, which are stitched to original PNs. On the other hand, the focus of the second problem is to deal with different pieces of a large sample and the choice of signature parts as inputs of PNSM. However, the ultimate goal of both problems is to obtain a large unified PN that is used in a flow solver to compute upscaled flow properties. We have defined these two problems in a fashion to be able to have a reference PN to compare predicted properties; however, the PNSM can certainly be applied on larger sizes as well for which it is not feasible to extract a single PN.

3.4.1 Connecting distant pore-networks

In order to investigate the quality of combining statistics of different PNs and a resulting average statistics, a Mt. Simon sandstone core with the size of $1200 \times 400 \times 400$ voxels and resolution of 2.80 μm is divided into three pieces (left, middle, and right) of 400^3 voxels having porosity 0.255, 0.233, 0.238, and absolute permeability 3784 mD, 2935 mD, 2598 mD, respectively from left to right (obtained by PN flow modeling). In the defined problem, the middle piece is removed and the left and right pieces are considered as signature parts of the PNSM. The goal is to combine the information from extracted PN from left and right pieces and to generate a middle PN that connect the two original PNs. Fig. 3.18 shows the steps taken to obtain the

final stitched PN from the two original PNs at left and right corners of the core.

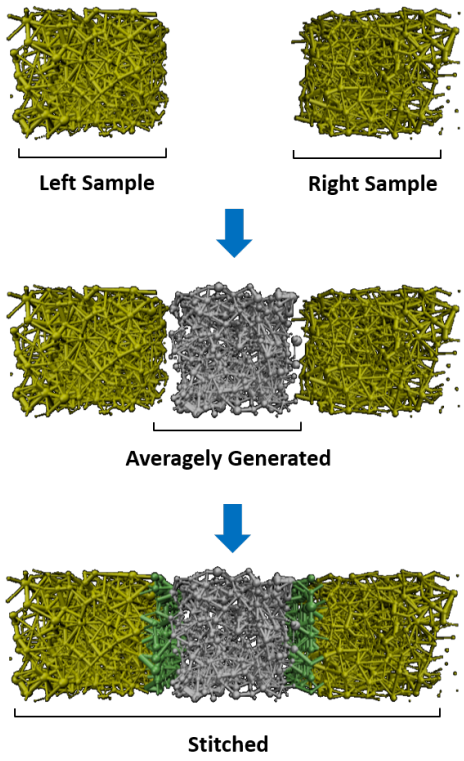

Figure 3.18: Stitching of pore-networks of two distant Mt. Simon sandstone samples by generating an average pore-network in the middle.

The resulting stitched PN is compared with the extracted PN from the entire core by taking the mean over 50 realizations. Figs. 3.19 and 3.20 show drainage relative permeability of CO_2 and brine, respectively, for 50 realizations along with their mean. Regardless of the variation across realizations, the comparison shows good agreement between the mean of the stitched PN curves and the reference PN curve for each phase.

3.4.2 Modeling a large heterogeneous sample

In order to apply the developed PNSM on a core-scale problem, we have constructed a large heterogeneous sample (6.4 mm^3) by extending a Berea sandstone sample in all directions and altering its pore structure in random locations. To do so, we chose random boxes with arbitrary sizes on the

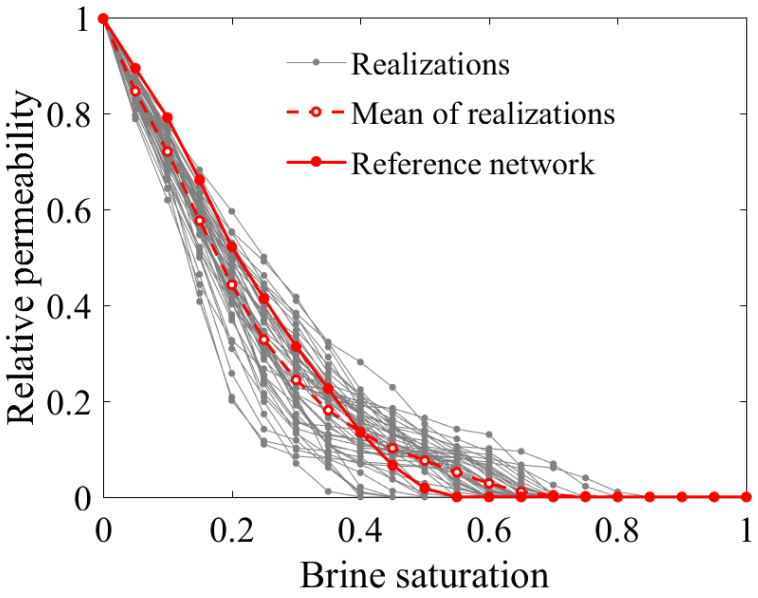

Figure 3.19: Comparison of drainage relative permeability of CO_2 from a long Mt. Simon sample with 50 realizations of stitched pore-networks and their mean.

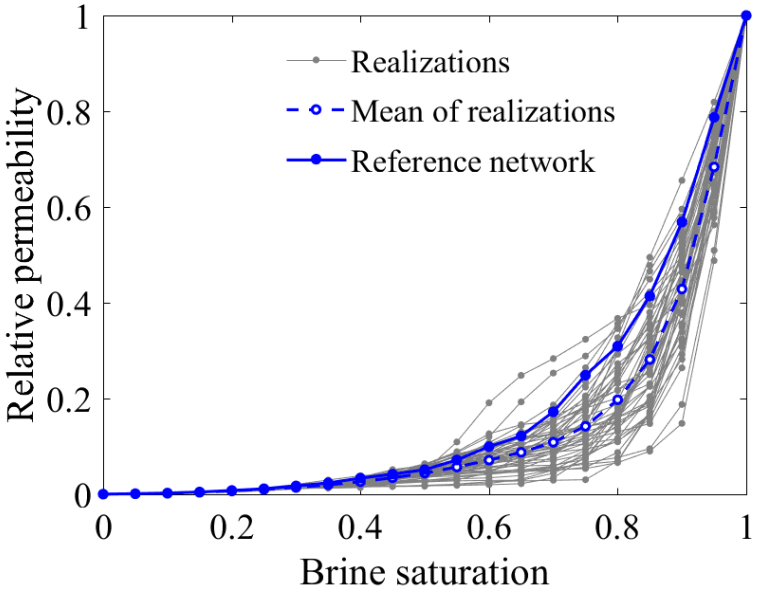

Figure 3.20: Comparison of drainage relative permeability of brine from a long Mt. Simon sample with 50 realizations of stitched pore-networks and their mean.

3D image of the extended sample and utilized noise addition or removal functions in Fiji (Schindelin et al. 2012) on the pore space of these boxes to expand or shrink the pore structure. The outcome is a wide range of variations in pore structure and a large heterogeneous sample. A stochastic approach is also implemented to quantify the heterogeneity of this sample where 1000 calculation boxes are chosen randomly and the statistics of their weighted average connectivity are calculated. The coefficient of variation of the statistics on the heterogeneous sample is 0.053 due to the randomized alteration of the pore structure while it is 0.018 (about one-third) on the homogeneous Berea sandstone and 0.007 on an equal-size uniform regular PN. The conclusion is that this sample is heterogeneous enough to be used for the actual application of the PNSM.

Fig. 3.21 shows a PN representation of this sample and how it is divided into 12 equal-size pieces. We labeled them from 1 to 12, starting from bottom left corner as depicted in Fig. 3.21, and marked three signature parts (pieces 3, 5, and 10) out of it based on the calculated range of porosity (from 0.152 to 0.221) and absolute permeability (from 219 mD to 1972 mD) across all pieces reported in 3.3. We have defined a problem where three signature parts are selected to start with and the rest of pieces are removed. The goal of the PNSM on this problem is to fill the empty space with pore elements and stitch them together and to the three signature parts to come up with a large stitched PN covering the entire domain. This PN is compared with a PN extracted from the original heterogeneous sample, as the reference PN, based on flow properties. We look into absolute permeability and drainage relative permeability curves of CO_2-brine flow across 50 realizations.

Fig. 3.22 shows the variation of absolute permeability over 50 realizations of stitched PNs having an arithmetic mean equal to 1389 mD, which shows excellent agreement with the reference PN, 1400 mD. This shows that the first three signature pieces could provide enough statistical information about the pore structure to construct a representative PN of the larger sample, and therefore, an accurate prediction of connectivity and permeability is resulted. It is also important to note that we are not seeking a single PN for this purpose but a mean over enough number of realizations due to the stochastic approach in generating pore elements in the initial empty space.

Figs. 3.23 and 3.24 show the comparative drainage relative permeability results between reference PN and realizations of stitched PN and their mean

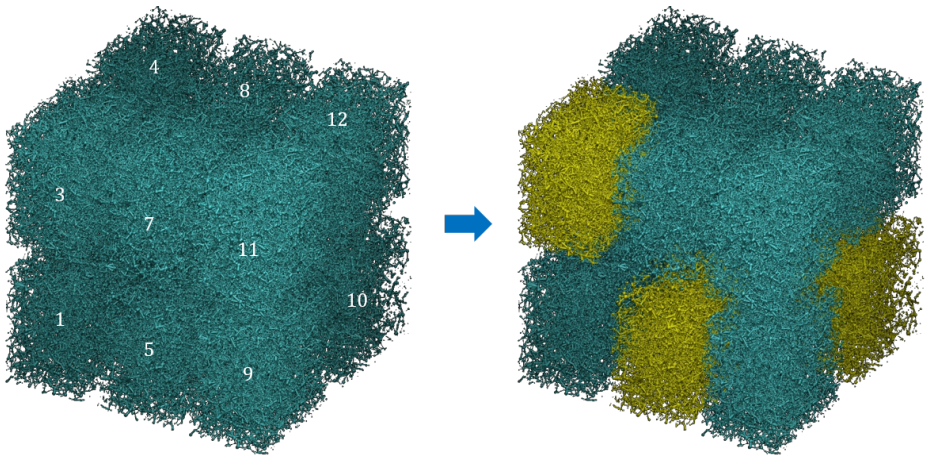

Figure 3.21: A pore-network representation of a constructed heterogeneous sample with its 12 equal-size pieces. Pieces 3, 5, and 10 are selected as signature parts.

Table 3.3: Absolute permeability of 12 pieces of the constructed heterogeneous sample

Pieces	Porosity	Permeability (mD)
1	0.170	803
2	0.221	3387
3	0.199	1608
4	0.182	972
5	0.170	926
6	0.201	1972
7	0.163	670
8	0.153	624
9	0.185	1075
10	0.152	219
11	0.202	1720
12	0.175	762

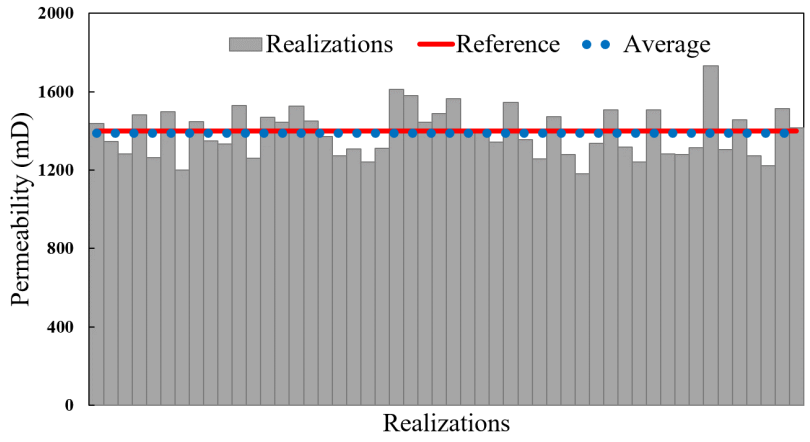

Figure 3.22: Absolute permeability over 50 realizations of stitched pore-networks from the heterogeneous sample.

for CO_2 and brine, respectively, as a function of brine saturation. The agreement for both phases is quite good when we compare the mean of realizations curves with the reference PN curves. Therefore, the PNSM could also provide a representative large PN with respect to two-phase flow properties when it is fed with signature parts.

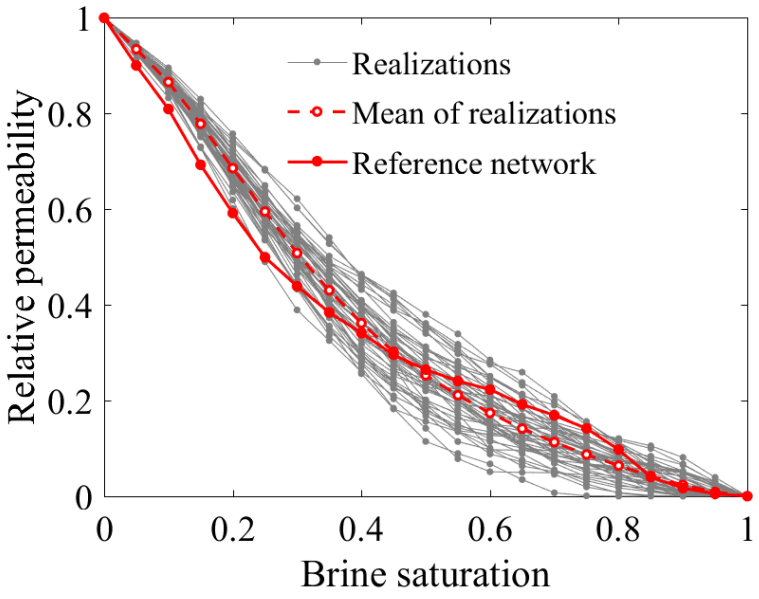

Figure 3.23: Comparison of drainage relative permeability of CO_2 from the large heterogeneous sample with 50 realizations of stitched pore-networks and their mean.

It is important to emphasize that we have deliberately use a constructed

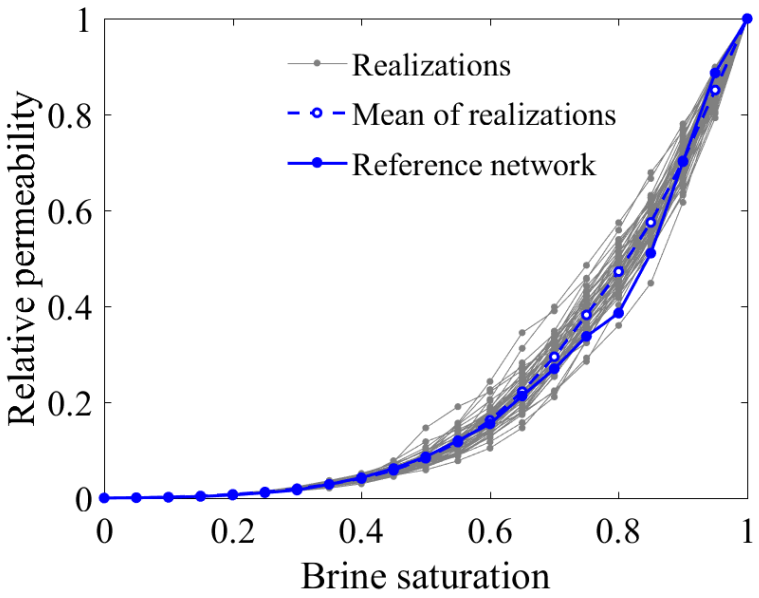

Figure 3.24: Comparison of drainage relative permeability of brine from the large heterogeneous sample with 50 realizations of stitched pore-networks and their mean.

large heterogeneous sample that is still small enough so that we are able to extract its PN in order to have a valid reference sample. However in practice, a reference PN of an entire core cannot be available in a real practical problem due to limitations as discussed in Section 3.1 and experimental measurements of rock flow properties can be used as a reference. In addition, this defined problem helped us to have properties of all different pieces of the sample in a way that we could readily choose three distinct ones as signature parts and use them as inputs of the developed PNSM. However, this step may not be as easy if we cannot capture properties of pieces of the entire core, and other methods such as fast pore size distribution evaluation on 2D industrial-scale images can be used to find those signature parts, and then, take micro-CT scans of them to get to signature PNs.

3.5 Summary and conclusions

We developed a pore-network stitching method (PNSM) to extend existing PN extraction and modeling capabilities to incorporate core-scale heterogeneity. The novel PNSM workflow takes a few signature parts representative

of different heterogeneous parts of the core as inputs and use their extracted PNs and statistics of their geometrical and topological information to generate and stitch new pore elements in the empty space of the domain. The PNSM gives multiple realizations of a large PN with non-stationary statistical properties that vary in the volume generated between the signature PNs. We carried out validation studies on all steps of the workflow including layered stitching (in longitudinal and lateral directions) and volumetric stitching for different types of rock samples to demonstrate that the developed method is robust and independent of the morphology of the pore space. Then, we applied the method to two large domain heterogeneous problems and computed absolute permeability and drainage relative permeability curves of CO_2-brine flow; this demonstrates that the method can construct a large representative PN for a heterogeneous porous medium and predict single-phase and two-phase flow properties successfully. Additional future work is necessary to apply the method on comprehensive multi-scale CT scans from a heterogeneous core and compare the predicted flow properties against core-scale experimental measurements.

3.6 Pore-network stitching method software

The source code of the introduced pore-network stitching method (PNSM) are available at: github.com/amirkohanpur/pn-stitcher. The instructions about compiling and running the code are provided in this address. The code is written in Fortran language (.f90 files) and compiled via GFortran (GNU Fortran compiler). The format of input and output pore-network files is in StatOil format, a commonly used data structure of pore-network files. More details about this format can be found in Sochi (2007).

In addition to the source code, the executable file and an example of input pore-network files with their stitched pore-network files are provided. The two-phase flow simulation files of the example using quasi-static pore-network solver (Valvatne and Blunt 2004) can also be found. Some post-processing files for visualizing the pore-network and plotting relative permeability and capillary pressure curves are also included.

Chapter 4

Modification

Improving pore-level flow models in residual trapping of CO_2 via direct numerical simulation

The physics of two-phase flow of CO_2 and brine in natural rocks plays an important role in geological storage of CO_2 captured from coal-fired power plants in deep saline reservoirs. It is well-known that macroscopic behavior of two-phase flow depends upon pore-scale physics due to the complexity of pore space of natural rock and because the wettability properties of the rock will affect the flow paths of the two fluids. Therefore, pore-scale modeling is necessary to understand fundamental behavior of CO_2-brine flow through the pores and obtain essential flow properties in field-scale simulation where prediction of amount and fate of trapped CO_2 is desired. Direct numerical simulation methods and pore-network modeling are common approaches to study such flow systems in natural rocks because experimental methodologies are difficult to implement, time-consuming, and expensive.

Although pore-network modeling is more computationally efficient compared with direct methods due to simplifications of the pore structure and governing flow equations, it does not accurately predict the full drainage-imbibition cycle in terms of residual trapped CO_2 and characteristic curves of CO_2-brine flow. In a quasi-static pore-network simulation on a Mt. Simon sandstone sample from a pilot CO_2 injection study, the saturation of trapped CO_2 at the end of imbibition process was approximately 70%, which is far greater than typical experimental results on sandstones (about 30–40%) reported in the literature. Such discrepancy becomes even greater when the contact angle is relatively small and the rock is highly heterogeneous. This error can also lead to inaccuracy in the resulting relative permeability and capillary pressure curves which are important inputs of field-scale simulators, and thus, it impacts the predicted fate and distribution of the CO_2 plume in

the reservoir. Since the residual trapping of CO_2 is mainly due to the movement of interfaces in pore elements and the order of pore-level events in the pore-network, the source of inaccuracy of trapped CO_2 due to shortcomings in simplifying assumptions used in quasi-static pore-network model, namely the pre-solved equations of local capillary pressure and flow of phases during piston-type displacement, pore-body filling, and snap-off events. These pore-level events have different contributions to the resulting trapped CO_2 after a drainage-imbibition cycle.

In this chapter, snap-off and pore-body filling events are the focus of lattice-Boltzmann simulations of CO_2-brine flow on pore-network configurations which are small collections of connected pore-bodies and pore-throats. A range of shape factors are chosen to define the geometry of pore-network configurations. The shape and evolution of the interface through pore elements are captured and associated to the threshold local capillary pressure. Based on the results from lattice-Boltzmann simulations, a new set of equations for different pore-body filling scenarios and snap-off on different triangular pore elements are proposed, and then, incorporated into a quasi-static pore-network solver. This modified model results a new pattern of invasion during imbibition process due to a different order of competing pore-level events. This modified pore-network model is applied on extracted pore-networks of Berea and Mt. Simon sandstone samples to predict residual trapped CO_2 and compare with data from experiment and direct numerical simulation. The modified model predicts smaller number of snap-off in pore-throats and higher number of pore-body fillings. As a result, it predicts residual trapped CO_2 less than the original model and is in better agreement with the available experimental data. The resulting CO_2-brine relative permeabilities are also calculated based on the modified model for both Berea sandstone and Mt. Simon sandstone samples.

4.1 Introduction

Physics of two-phase flows in natural rocks plays an important role in addressing many current issues in water, energy, and climate. In particular, capture and geological storage of carbon dioxide (CO_2) in deep saline reservoirs are being studied widely as a potential technology to reduce emission of green-

house gases from conventional power plants. Pore-scale modeling is necessary to understand fundamental behavior of CO_2-brine flow and obtain rock-flow properties needed for field-scale studies such as reservoir simulation. Direct numerical simulation (DNS) methods and pore-network (PN) modeling are common approaches to study such flow systems in natural rocks because experimental methodologies are difficult to implement, time-consuming, and expensive. On one hand, DNS solves directly the Navier-Stokes equations from images of rock. On the other hand, PN modeling extracts a simplified network of pore elements from the real geometry of pore spaces and solves Navier-Stokes equations in the simplified geometry.

Although PN modeling is more computationally efficient compared with DNS due to simplifications of the pore structure and governing flow equations, PN modeling has inaccuracies in predicting the full drainage-imbibition cycle curves and residual trapped non-wetting phase in CO_2-brine flow system. This is important for assessing the long-term storage capacity and safety of geological sequestration. As an example, quasi-static PN simulations on a Mt. Simon sandstone sample from a pilot CO_2 injection site shows approximately 70% trapped CO_2 at the end of imbibition cycle, which is far greater than typical counterpart experimental and DNS results on sandstones (about 30–40%). Such discrepancy becomes even greater when the contact angle is relatively small and the rock is highly heterogeneous, which is the case in the studied Mt. Simon sandstone sample. This error also leads to inaccuracy in the resulting relative permeability and capillary pressure curves which are important inputs of field-scale simulators, and thus, it impacts the predicted fate and distribution of the CO_2 plume in the reservoir.

The CO_2-brine flow is usually considered as a capillary-dominated flow system. Therefore, capillary forces determine the interface movement, flow, and trapping through the pore space. These are described as local capillary pressure of pore-level events in PN modeling which their competition determines the invasion pattern of phases, and thus, residual trapping of CO_2. Therefore, the source of inaccuracies in residual trapping is back to the defined pore-level flow models and pre-solved equations of threshold local capillary pressure of PN events — piston-type displacement, pore-body filling, and snap-off — in pore elements. These pore-level events have different contributions to the resulting trapped CO_2. Their flow models can be studied and revised using DNS to improve their accuracy. DNS meth-

ods can generally predict the shape and evolution of interface, flow rate and distribution of each phase, and incorporate viscous and capillary forces. We apply lattice-Boltzmann (LB) simulation as a DNS method on various geometric PN configurations, that encompass a small collection of connected pore-bodies and pore-throats, to evaluate local capillary pressure during imbibition process. Then, we propose a modified model of imbibition events with new parameters and factors, accordingly. The modified model is then incorporated into a quasi-static PN flow solver that can be applied on extracted PNs from natural rocks (Dong and Blunt 2009; Raeini et al. 2018) or on larger PNs from upscaling approaches (Aghaei and Piri 2015; Kohanpur and Valocchi 2020a) thereby resulting in more realistic macroscopic characteristic curves.

The organization of the rest of this chapter is as follows. A detailed literature review is presented in the next section. Section 4.3 explains the physics of pore-level events in a two-phase flow system in PN modeling. Section 4.4 discusses the defined PN configurations and the used simulation methods. In Section 4.5, the main results from LB simulations of pore-body filling and snap-off in pore-throat are discussed (Section 4.5.1). Then, the modified model is presented and incorporated into the quasi-static PN flow model, and applied on real rock samples (Section 4.5.2). Finally, the conclusions are summarized in Section 4.6.

4.2 Literature

Ever since the early generation of two-phase flow PN models, there have been attempts to improve pore-level flow models during drainage and imbibition cycles for better understanding and prediction of core-scale macroscopic constitutive relations, including relative permeability functions and residual trapping of non-wetting phase. This is important during CO_2 injection into deep saline aquifer or depleted oil reservoirs where the physics of flow can be modeled by immiscible two-phase flow of supercritical CO_2 and brine. We categorize the relevant studies to this research objective into three categories:

Category 1 includes classic PN modeling studies where detailed description of drainage and imbibition flow with corresponding pore-level events are presented and validated in a PN flow solver (Blunt 2001; Valvatne and Blunt

2004; Raeini et al. 2018). Lenormand et al. (1983) first described pore-scale displacement mechanisms during drainage and imbibition from a 2D micromodel experiment. These displacements mechanisms are piston-type, snap-off, and pore-body filling that are widely used in PN flow solvers. For example, the commonly used quasi-static PN flow solver developed by Valvatne and Blunt (2004) includes pore-level displacement events in pore-bodies and pore-throats during drainage and imbibition cycles in a capillary-dominated flow system where capillary number (Ca) is less than 10^{-4} and viscous pressure drop can be neglected. Raeini et al. (2018) presented a newer version of this capillary-dominated PN flow model that includes the concept of half-throats, several corners in pore elements, and new formulations of pore-level events. This solver was verified experimentally by Bultreys et al. (2020) using measured contact angle and based on the evolution of fluid distributions and flow paths during imbibition cycle. The source code of both of these PN flow solvers are available for any potential modifications. In both models, the definition of cross section of pore elements based on the concept of shape factor and flow conductance of phases come from the studies done by Patzek and Silin (2000) and Patzek and Kristensen (2001).

Category 2 includes studies that focus on pore-level events of PN modeling and using DNS for improvement, such as proposing new cross sections of pore elements, flow properties in pore-throats, local capillary pressure relations, corner flow behavior, and so on (Ruspini et al. 2017; Xie et al. 2017; Zhao et al. 2020). Among studies using LB on pore elements of PN, Xie et al. (2017) implemented LB simulation inside individual pores with triangular cross section to describe viscous coupling in oil-water flow as empirical terms. They incorporated these terms into a quasi-static PN solver that resulted a more accurate prediction of relative permeability curves. In another study, Zhao et al. (2020) coupled LB and PN methods to simulate drainage through sandstones and obtain higher accuracy of flow properties. They applied multi-relaxation-time color gradient LB model on real pore-throat cross sections to obtain properties, namely, threshold local capillary pressure, macroscopic capillary pressure curve, absolute permeability, and relative permeability.

There are also studies using other DNS approaches on pore elements of PN to improve the current models. Miao et al. (2017) proposed a novel description of PN elements to avoid geometry simplifications of conventional

PN models by using circularity, convexity, and elongation of voxelized pores. They carried out finite element simulations to obtain single-phase flow conductance and approximate the relationship between pore shape parameters and hydraulic conductance. Shams et al. (2018) incorporated viscous coupling effect into flow conductance of triangular tubes in different wettability conditions with the aid of finite volume simulation. They investigated the flow in the center and corners of a capillary tube and sandwiched layers with different boundary conditions at the interface and proposed viscous coupling effect as a function of geometry, viscosity ratio, wetting phase saturation, and wettability in the flow conductance term. Tang et al. (2018) carried out volume of fluid two-phase flow simulations via Fluent software on various cross sections (circle, square, equilateral triangle, and regular hexagon shapes) of tube to investigate the effect of contact angle on meniscus behavior and local capillary pressure in individual pores. They proposed a correlation to quantify the resulting stabilized meniscus geometry and calculate equivalent radius of a polygonal channel in order to compute local capillary pressure based on Young-Laplace equation.

On the other hand, some studies are conducted purely based on geometrical features of the pore elements to improve the current models. Ruspini et al. (2017) introduced a new model of pore-body filling to investigate capillary trapping of non-wetting phase in water-wet rocks. The model incorporated geometrical characteristics of the pore-body, spatial location of connecting filled pore-throats, and wetting properties. They validated their model based on residual trapping, imbibition relative permeability, and capillary pressure curves from PN modeling of different sandstone samples. Suh et al. (2017) conducted a morphological analysis technique along with LB simulation on different irregular pore-throat cross sections to establish a correlation between effective shape factor and local capillary pressure. They validated their method by comparing macroscopic capillary pressure with experimental data of water retention curve.

Category 3 includes studies on the physics of CO_2 and brine flow at pore-scale to understand the evolution of interfaces, displacement dynamics, capillarity, and trapping mechanisms such as residual trapping of CO_2 (Jiang and Tsuji 2015; Chen et al. 2018; Mahabadi et al. 2020). In a pioneering work, Land et al. (1968) introduced an empirical relation of residual trapping of non-wetting phase of a two-phase flow system that relates initial and resid-

ual saturations known as Land's initial-residual trapping model. Jiang and Tsuji (2015) studied the effect of interfacial tension on residual CO_2 clusters using LB simulation on Berea sandstone. They quantified capillary trapping mechanism and its stability by characterizing residual CO_2 cluster distribution in terms size distribution, major length, interfacial area, and sphericity. Some studies have reported the residual trapped CO_2 by experimental approaches. Perrin and Benson (2010) measured relative permeability of CO_2 and brine on a heterogeneous core from an actual storage reservoir and obtained a drainage end point of $S_{nw} = 0.56$ while the capillary number is 2.5×10^{-5}. Levine et al. (2014) conducted experiment of CO_2 injection (in liquid and supercritical conditions) into brine-saturated synthetic and natural porous media to measure drainage end point relative permeability and saturation. Most of reported saturation values of this study are in range $S_{nw} = 0.60 - 0.70$ for drainage end point.

There are also some PN modeling studies focused on residual trapping in CO_2-brine flow through real rock samples. Mahabadi et al. (2020) studied immiscible displacement patterns during drainage cycle in a dynamic PN model by varying capillary number (Ca) and viscosity ratio (M). They also examined the effect of pore-throat size distribution and PN connectivity on a sandy sediment for different sets of Ca and M. Matching their findings with properties of a typical CO_2-brine flow system ($Ca \simeq 10^{-5}$ and $M \simeq 10 - 15$), the dominant displacement pattern is capillary fingering and the end point of drainage is about $S_{nw} = 0.50 - 0.60$. On the other hand, Rasmusson et al. (2018) used a quasi-static PN model of CO_2-brine flow on Heletz sandstone to investigate the sensitivity of residual trapping of CO_2 to several parameters such as advancing contact angle and average connection number. They also obtained the initial-residual saturation curves of CO_2 in different drainage-imbibition scenarios. In addition, Hefny et al. (2020) applied quasi-static PN modeling on a highly permeable sandstone from a depleted oil field to study residual trapping of CO_2 and obtain characteristic curves during drainage and imbibition cycles. They investigated the effect of initial brine saturation at the reversal point from drainage to imbibition on residual trapping and relative permeabilities. They also found that smaller contact angle values (more brine-wet rock) lead to higher trapped amount of CO_2 at the end of imbibition cycle.

In this chapter, we use the available codes of quasi-static PN flow solver

(Category 1) and apply LB simulations to develop new local capillary pressure relations for pore-body filling and snap-off events as a function of shape factor which was not proposed in other models in the literature (Category 2). Then, we apply the modified PN model on two sandstones to evaluate the residual trapping and relative permeabilities in a drainage-imbibition cycle of CO_2-brine flow (Category 3).

4.3 Pore-level processes and events

4.3.1 Drainage and imbibition

Drainage process happens when the non-wetting phase displaces the wetting phase and imbibition process is vice versa. Both processes can occur in individual pores locally or across the porous medium averagely based on the direction of saturation change. In the application of geological storage of CO_2, the pore space of a saline aquifer is initially filled with brine, as the wetting phase. Injection of CO_2, as the non-wetting phase, into the pore space is a drainage process where the macroscopic capillary pressure and overall saturation of CO_2 increase. At the end of the drainage process, the saturation of CO_2 is maximum. If the macroscopic capillary pressure drops, brine fills the pore space gradually which is the imbibition process. Due to wettability, the entire CO_2 will not be displaced by the brine and some gets trapped across the pore space at the end of imbibition. This phenomenon is called residual trapping of CO_2 which is in favor of storage of CO_2 due to the capillary forces between phases.

As mentioned before, capillary forces drive flow in a CO_2-brine system which results in low flow rate in both drainage and imbibition processes. In PN modeling of these process, one should gradually change the macroscopic capillary pressure and control the direction of invasion. On one hand, capillary pressure is increasing incrementally during drainage which allows CO_2 to displace the brine in the center of pores through piston-type displacement while brine resides in the corners and crevices. Based on Young-Laplace equation, wider pores (pore-bodies) are invaded first in drainage followed by invasion of narrower pores (pore-throats).

On the other hand, imbibition process occurs after the drainage process

that has left a residual brine in the corners due to wettability. Capillary pressure decrease incrementally by increasing brine pressure which allows brine to displace CO_2 through different displacement events, namely, piston-type displacement, pore-body filling, and snap-off (Lenormand et al. 1983). The occurrence and frequency of these events depend on the local capillary pressure in pore element, the topology of brine and CO_2 (connection number and filling), wettability (contact angle), pore irregularity (shape factor), and relative size of pore-body with respect to neighboring pore-throats (aspect ratio). These events can compete with one another and influence the invasion pattern and trapping of CO_2 at the end of imbibition process.

In the low capillary number condition of CO_2-brine flow, the assumption of local capillary equilibrium is valid which relates the curvature of interface in any pore at any time to the local capillary pressure based on Young-Laplace equation. This assumption is the basis of quantifying the threshold local capillary pressure of different displacement events through the shape of interface in pore elements.

4.3.2 Piston-type displacement

In piston-type displacement, the invading phase displaces the defending phase from the center of the pore element. For example in drainage, if CO_2 pressure is high enough (i.e., local capillary pressure passes the threshold) in a pore element, it displaces brine through its terminal meniscus from the center of the pore element. Fig. 4.1 shows schematically how CO_2 (in white) is advancing through the center of a rectangular tube and pushing brine (in blue). This displacement event requires an adjacent filled pore element with the invading phase. The threshold capillary pressure depends on the wettability and geometry of the pore element through the Young-Laplace equation, which for a circular tube pore element it is:

$$P_c = \frac{2\sigma\cos\theta}{r} \tag{4.1}$$

In Eq. 4.1, P_c is the threshold local capillary pressure, σ is surface tension, θ is contact angle between phases, and r is the radius of the cross section of the tube. If the capillary pressure is exceeded this threshold, then the pore is instantly invaded by CO_2. Related equations for rectangular and triangular

cross sections become different can be found in Valvatne 2004.

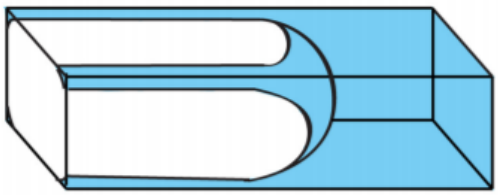

Figure 4.1: Schematic representation of piston-type displacement during drainage process in a rectangular tube. CO_2 (in white) is displacing brine (in blue) in the pore-throat (Image from Rasmusson et al. (2018)).

4.3.3 Snap-off

As mentioned earlier, the injected CO_2 (as the non-wetting phase) occupies the center of pore elements at the end of drainage process while brine (as the wetting phase) resides in the corner as connected layers throughout the PN. As the brine pressure increases and the imbibition process starts, these layers will swell and increase the CO_2 saturation slowly. If the brine layer is not connected to any adjacent brine-filled elements and the swelling continues due to increase in the pressure, at some point the brine layers from corners meet and create an unstable state. This leads to snap-off where brine spontaneously fills the center of pore element. This mechanism happens in pore-throats first during imbibition since they have smaller radius. Snap-off in a pore-throat that does not have adjacent brine-filled elements disconnects brine in adjacent pore-bodies which translates into either partial filling or trapping in following states of the PN and impacts the distribution of CO_2 throughout the PN. Fig. 4.2 shows schematically how the progress of swelling of brine layer in pore-throat can lead to snap-off. The brine phase gets disconnected between the two adjacent pore-bodies. In Fig. 4.2, brine in the right pore-body will be trapped and brine in the left pore-body is losing one order of filling.

Swelling and snap-off can also be observed at the cross section of pore-throat by the change in the area of brine in corners. A rectangular cross section of pore-throat is shown in Fig. 4.3: (a) is the beginning of imbibition

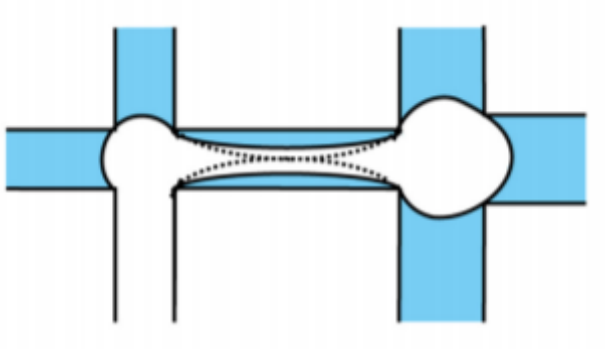

Figure 4.2: Schematic 2D representation of snap-off in pore-throat during imbibition process. Brine (in blue) starts swelling from the corners and eventually disconnects CO_2 (in white) in the center of pore-throat (Image from Rasmusson et al. (2018)).

where all brine layers are separate at their corners, (b) is when swelling has moved interfaces and increased brine saturation in the pore-throat, (c) is the unstable state on the brink of snap-off where the three-phase contact between fluid phases and solid can no longer exists, and (d) is right after snap-off where the pore-throat is spontaneously occupied by brine.

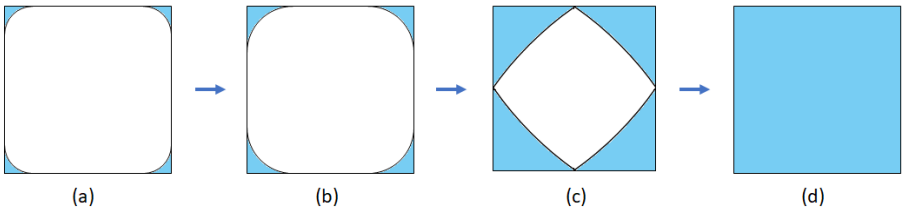

Figure 4.3: Schematic representation of progress of brine (in blue) swelling during imbibition and snap-off at the cross section of a rectangular pore-throat.

4.3.4 Pore-body filling

When the capillary pressure decreases during imbibition process through the increase of brine pressure, the invading brine starts with filling narrower pore-throats and displacing CO_2 to the available adjacent elements which are pore-bodies filled with CO_2. Depending on the connection number of the pore-body (number of pore-throats connected to it) and number of CO_2-filled adjacent pore-throats, different scenarios of pore-body filling can occur. Fig.

4.4 shows a schematic representation of two scenarios (I_1 and I_2 events) for a pore-body with connection number of 4. I_n refers to a pore-body filling where there are n connected pore-throats filled with CO_2 that allows an escape path during the invasion of brine into the pore-body. For a pore-body with connection number of z_{cn}, n can be between 0 to $z_{cn} - 1$.

The important feature of I_n events is that their entry capillary pressure can be different since the interface curvature that results during invasion is different. For example in Fig. 4.4, the I_1 event would result in larger curvature (i.e., smaller radius of curvature) than I_2 based on the drawn dash lines referring to next steps.

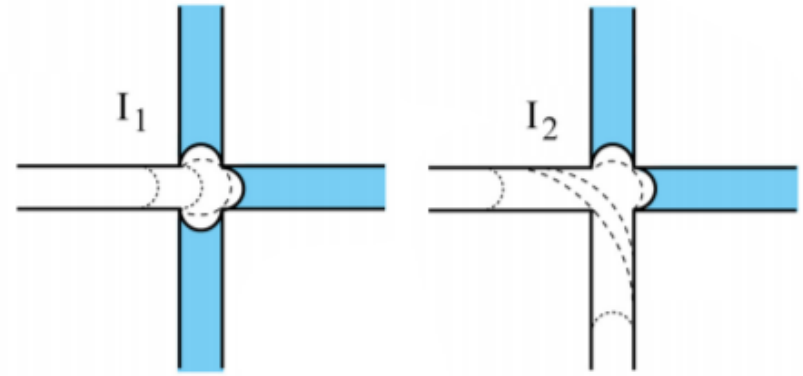

Figure 4.4: Schematic 2D representation of pore-body filling, I_1 and I_2 events, during imbibition process. Brine (in blue) is entering the pore-body from connected pore-throats and CO_2 (in white) escapes through the remaining pore-throats (Image from Rasmusson et al. (2018)).

If no connected pore-throat is filled with CO_2 (I_0 event), the CO_2 is already trapped. If only a single connected pore-throat is filled with CO_2 (I_1 event), the displacement process will be similar to piston-type displacement. The complexity of modeling is for higher order events (I_n, n from 2 to $z_{cn} - 1$) where the exact location and curvature of interface in the pore-body is not clear. There are different studies in the literature proposing different parametric models by taking into account geometry-based and statistics-based parameters in the model. Blunt (1998) proposed a model based on the generic form of P_c in piston-type displacement and reducing it with a parametric term to describe P_c of higher order I_n events:

$$P_c = \frac{2\sigma\cos\theta}{r_p} - \sigma \sum_{i=1}^{n} A_i x_i \tag{4.2}$$

In Eq. 4.2, A_i is the model parameter chosen correlated with the inverse of absolute permeability of the PN, and x_i is a random number between zero to one. Another form of this model is proposed by Hughes and Blunt (2000) as:

$$P_c = C_{I_i} \frac{\sigma \cos\theta}{r_p} \tag{4.3}$$

In Eq. 4.3, C_{I_i} is the empirical coefficient of the pore-body filling event $\mathrm{I_i}$ ($C_{I_1} = 1.7$, $C_{I_2} = 1.15$, $C_{I_3} = 0.7$, $C_{I_{4+}} = 0.5$). More details on parametric models can be found in Blunt 2017.

4.3.5 Competition of events in imbibition

The imbibition process in a PN flow model consists of a series of pore-level events (described in Sections 4.3.2, 4.3.3, 4.3.4) in pore elements based on their threshold local capillary pressure. These events compete with one another in determining the invasion pattern and distribution of phases during imbibition. Therefore, the prediction of CO_2 distribution and trapping is connected with the study of occurrences of these events. A change in the threshold local capillary pressure or the order of displacement events can lead to a different pattern of phases, relative permeability, and residual trapping.

The threshold local capillary pressure of each event determines timing and location of events. In drainage, the largest pore-bodies are invaded by CO_2 first, and then, smaller pore-bodies and narrow pore-throats are invaded while the imposed macroscopic capillary pressure increases incrementally. On the other hand, the imposed macroscopic capillary pressure decreases during imbibition process and narrower pore-throats are the first elements where brine displaces CO_2 through different pore-level events.

In imbibition, the topology of brine phase also matters to determine the type of event. If the adjacent element has brine at its center, the piston-type or pore-body filling would occur if the threshold local capillary pressure is already reached. Snap-off, however, does not require adjacent filled elements since it starts with swelling of brine at the corner which is present all over the PN. In practice, the ratio of threshold local capillary pressure of events should be checked in elements with adjacent brine-filled elements.

4.3.6 Effect of parameters in imbibition

- **Shape factor:** It summarizes the irregularities of the pores into one one parameter in pore elements. The half-angle values of a triangular pore element can be obtained based on the shape factor (Patzek and Silin 2000). These half-angle values are involved in the threshold local capillary pressure (P_c) relations of different pore events. In this study, different defined shape factors of the cross section are considered to evaluate the effect of shape factor on imbibition pore-level events.

- **Aspect ratio:** The aspect ratio of a pore-body is the ratio of its radius to the radius of its connected pore-throats ($a = r_p/r_t$). This parameter can be also expressed using average radius of multiple connected pore-throats to a pore-body. The competition of threshold P_c of pore-body filling and snap-off events is correlated with aspect ratio. This competition can be quantified by the ratio of their threshold P_c (Blunt 2017). Generally, higher aspect ratio values results in more snap-off events compared to pore-body filling events. In this study, typical aspect ratio values from extracted PNs of natural rocks are used to define PN configurations.

- **Connection number:** The number of connected pore-throats to a pore-body is its connection number. It can be averaged across all pore-bodies of the PN as average connection number (z_{cn}) that represents the connectivity. Although z_{cn} is not explicitly used in threshold P_c relations, it is correlated with trapping of CO_2. The higher values of z_{cn} means more potential pore-throats for the CO_2 to escape from the invaded pore-bodies during imbibition process.

- **Contact angle:** Wettability is an important factor in the brine invasion pattern during imbibition process. It is described by contact angle (θ) between phases and can vary in different locations of the core. The threshold local capillary pressure in pore elements is usually proportional to $cos\theta$. Due to contact angle hysteresis, a successful model should incorporate receding and advancing contact angles (θ_r and θ_a) during drainage and imbibition processes, respectively. More detail on using contact angle hysteresis in PN modeling can be found in Valvatne

(2004). In this study, measured CO_2-brine flow contact angle values from an experimental study by (Dalton et al. 2018) are used.

4.4 Methodology

4.4.1 Pore-network configurations

We aim to apply DNS of two-phase flow via the LB code developed by Chen et al. (2018) on pore elements of PNs from natural rocks to assess the physical assumptions used for pore-level events. Therefore, the geometry of simulations consists of typical pore-bodies and pore-throats of extracted PNs with enough resolution to capture the interface and corner flow. We define a PN configuration as a small number of interconnected pore-throats and pore-bodies that is designed for investigation of pore-level events during imbibition in the pore element of interest. Two types of PN configurations are studied here:

- **PTP configuration:** This refers to a pore-throat connecting two pore-bodies, as shown in Fig. 4.5(a) with triangular elements. The pore-throat is the focus of this configuration to investigate corner flow, piston-type displacement, or snap-off. The pore-bodies can be connected to inlet and outlet reservoirs of non-wetting and wetting fluids or additional pore elements. We study the PTP configuration to capture the interface in the cross section of the pore-throat and find the threshold P_c right before snap-off occurs.

- **TPT configuration:** This refers to a pore-body defined between two or more connecting pore-throats, as shown in Fig. 4.5(b) with triangular elements. The pore-throats can be directly connected to the inlet and outlet reservoirs or other pore-bodies. The pore-body is the focus of this configuration to investigate the filling process via different number of pore-throats and simulate pore-body filling during imbibition process.

Conventional quasi-static PN models can use pore elements with different cross sections; triangle, square, circle are considered here as they are commonly used. The shape factor (G) is a dimensionless geometric parameter

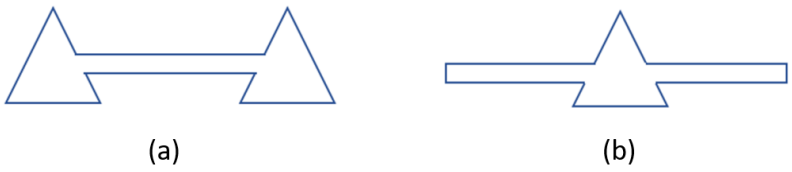

Figure 4.5: Two types of PN configurations with triangular cross section: (a) PTP configuration where the focus is on the pore-throat and (b) TPT configuration where the focus is on the pore-body.

that quantifies irregularities of a pore element. It is a key parameter in assigning familiar geometries to the cross section of a tube-shape pore element (Patzek and Silin 2000). It is defined as:

$$G = \frac{VL}{A^2} \tag{4.4}$$

In Eq. 4.4, A is the cross-sectional area, V is the volume, and L is the length of the tube-shape pore element with an arbitrary cross section. In practice, the triangular cross section comprises the majority of pore elements of PNs from different rock types. Shape factor of triangular elements can vary in a range from 0 (slit-shape) to 0.0481 (equilateral). In this study, we select three shape factor values equal to 0.020, 0.030, 0.040 for the designed PN configurations to represent a reasonable range while limiting the number of required LB simulations. The corresponding cross section of these shape factors are illustrated in Fig. 4.6. The corner half-angle values (β's defined as $\beta_1 < \beta_2 < \beta_3$) based on the algorithm by Patzek and Silin (2000) are listed in Table 4.1.

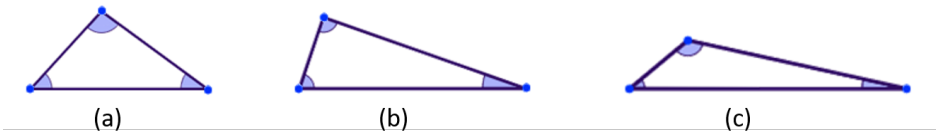

Figure 4.6: Three selected triangular cross sections of pore element for including shape factors of (a) $G = 0.040$, (b) $G = 0.030$, (a) $G = 0.020$ in studied pore-network configurations.

As discussed in Section 4.3.4, pore-body filling process can occur in different scenarios depending on the number of adjacent CO_2-filled pore elements. These scenarios can be defined with different TPT configurations based on

Table 4.1: Corresponding corner half-angle values of the chosen shape factors of based on Patzek and Silin (2000) algorithm. All β's are in degrees.

Shape factor	β_1	β_2	β_3
G=0.020	6.20	19.7	64.1
G=0.030	9.6	35.6	44.8
G=0.040	18.0	23.7	48.3

the number of connecting pore-throats to the pore-body of configuration, which will be addressed in Section 4.5.1.1.

4.4.2 Lattice-Boltzmann method

The lattice-Boltzmann (LB) method will be used for DNS for the idealized pore element geometry noted above. Use of LB for DNS on voxelized pore geometry is now well established, and its popularity is due to its favorable computational features (Tölke 2002; Chen et al. 2018). The LB is a so-called mesoscopic method that can simulate fluid mass and momentum balance. The fluid is represented by particles with probability of moving in different directions along a predefined lattice. It is described based on streaming, collision and relaxation of a set of fluid particle distribution functions (PDF) on a lattice. The no-slip boundary conditions on solid surfaces are implemented by simply switching the directions of the particles on the surface nodes, the so-called bounce-back scheme. Among several LB schemes for simulating multiphase flows, the color-fluid model (Gunstensen et al. 1991; Grunau et al. 1993) is capable of producing a relatively sharp interface between immiscible phases and capturing their interface evolution. The color-fluid model is also able to incorporate high viscosity ratios due to its independent control of the surface tension and viscosity which makes it quite relevant to CO_2-brine flow system where viscosity ratio is about 10–15. On the other hand, it has limitations on the density ratio and a large absolute value of color gradient may produce numerical instabilities (Ramstad et al. 2019).

We use a variant of the multiple relaxation time (MRT) color-fluid LB simulator (Tölke 2002; Tölke et al. 2006; Chen et al. 2018). In this model, each phase has its own set of PDFs and the discrete Boltzmann's equation is solved for each phase. We consider two sets of the D3Q19 PDFs, i.e., a 3D

model with 19 velocities, representing the two fluid phases, referred to as the fluids r (CO_2) and b (brine), which follow the collision-streaming procedure for the PDF:

$$f_i^s\left(x+e_i\Delta t, t+\Delta t\right) = f_i^s\left(x,t\right) + \Omega_i^{s(3)}\left\{\Omega_i^{s(1)} + \Omega_i^{s(2)}\right\}, s = r, b \qquad (4.5)$$

In Eq. 4.5, $\Omega_i^{s(1)}$ is the standard LB collision operator, $\Omega_i^{s(2)}$ is the perturbation step that generates the surface tension effect, and $\Omega_i^{s(3)}$ is the recoloring step that separates the two fluids. The collision operators $\Omega_i^{s(1)}$ and $\Omega_i^{s(2)}$ are constructed under the MRT framework that increases stability and accuracy of the model (d'Humieres 2002; Tölke et al. 2006). The macroscopic quantities of flow, such as fluid velocity and pressure, are computed by calculating the moments of the PDFs. More details of our in-house code are given by Chen et al. (2018).

In the present work, we carry out LB flow simulations of CO_2-brine flow system on PN configurations. The fluid properties and flow conditions are listed in Table 4.2, which are similar parameters used in Kohanpur et al. (2020) except the contact angle comes from an experimental study by Dalton et al. (2018). We simulate the drainage process followed by the imbibition process with inlet velocity and outlet pressure boundary conditions. The capillary number of 5×10^{-5} is fairly small that guarantees a capillary-dominated flow observed in CO_2-brine flow experiments. However, smaller values of capillary number can be computationally expensive with potential numerical instabilities.

Table 4.2: Properties of CO_2-brine flow system.

Properties	Value
Contact angle (°)	56 (brine-wet)
Interfacial tension (mN/m)	30.0
Brine density (Kg/m^3)	1100
CO_2 density (Kg/m^3)	1100
Brine kin. viscosity (m^2/s)	1×10^{-6}
CO_2 kin. viscosity (m^2/s)	1×10^{-7}
Capillary number	5×10^{-5}
Viscosity ratio	10

4.4.3 Quasi-static pore-network model

The quasi-static PN flow simulation is an efficient tool to characterize single-phase and CO_2-brine flow properties. The capillary number of this two-phase flow system is relatively small (less than 10^{-5}) which justifies the assumption of capillary-dominated flow and is also the case in practice for large scale CCS. In this work, we carry out drainage and imbibition simulations via the publicly available PN flow codes of Valvatne and Blunt (2004) and Raeini et al. (2018). We incorporate modified equations imbibition pore-level events (which are discussed in Sections 4.5.1.1 and 4.5.1.2) into the solver and apply it on extracted PNs from real rock images to obtain residual trapping of CO_2 and relative permeability curves. The detailed procedure of the PN flow solver is described in Valvatne (2004) and Raeini (2013).

4.5 Results

4.5.1 Lattice-Boltzmann flow simulation

The PN configurations in Section 4.4.1 are used as the input geometry of LB simulation where each voxel of the image is converted to a lattice unit. It is a normal practice in LB simulations to use dimensionless parameters and normalize with lattice units and then convert to physical units when needed. A lattice unit can be as pore (0-value) or as wall (1-value), and the set of PDFs of each phase is solved in lattice units. The phase saturation and the interface can be distinguished with the order parameter (ϕ) in the color gradient LB model:

$$\phi = \frac{\rho_r - \rho_b}{\rho_r + \rho_b} \tag{4.6}$$

In Eq. 4.6, ρ_r and ρ_b are fluid densities of red and blue fluids in lattice unit, respectively. The density of each phase is computed by the zeroth moment of the PDFs. Therefore, $\phi \approx 1$ refers to the presence of red fluid while $\phi \approx -1$ represents the presence of blue fluid. The location of interface is where $\phi \approx 0$. This is because the fluid interface is diffuse and spread over several lattice units, but if we use fine grids, then we can have a relatively sharp interface. In practice, we use the cut-off of 5% for ϕ to specify the location of each

fluid.

In order to evaluate local capillary pressure in pore elements, one can use the relation between density and pressure based on the distribution of order parameter in the lattice unit. This calculation procedure of local capillary pressure is validated on a simple piston-type displacement in a cylindrical tube, as illustrated in Fig. 4.7. We use the resulting density of fluids to obtain the pressure distribution in each fluid to calculate their pressure difference and relate it to the local capillary pressure during the filling process. In the color-fluid LB method, a simple ideal equation of state is assumed which allows calculation of fluid pressure from the density. The order parameter is used to detect the location of phases and the interface. The calculation of phases pressure should be far enough from where the order parameter is about zero in order to compute the pressure of the pure red and blue fluid phases. The pressure of the red and blue fluids can be averaged based on the total density of mixture fluid in lattice units of a calculation box (e.g., pore-body).

$$\bar{P}_r = \frac{\sum 1/3\rho_{r_i}}{n_r} \tag{4.7}$$

$$\bar{P}_b = \frac{\sum 1/3\rho_{b_i}}{n_b} \tag{4.8}$$

In Eqs. 4.7 and 4.8, the summation is over the lattice units of a defined calculation box, respectively, and n_r and n_b are the number of lattice units of red and blue fluids in the calculation box, respectively. Thus, the local capillary pressure (P_c) in the calculation box can be obtained using the difference in the pressure of red and blue fluids in this LB color-fluid model. In Fig. 4.7 (left), the calculation box is marked with two blue planes.

$$P_c = \bar{P}_r - \bar{P}_b \tag{4.9}$$

In Eq. 4.9, P_c is the calculated average local capillary pressure within the calculation box of interest. Fig. 4.7 (right) shows a cross-sectional view through the center of tube in this simple piston-type displacement simulation. The radius of interface (r') can be captured and used in the Young-Laplace equation to evaluate local capillary pressure, which is denoted the cross-sectional approach. Using the interface from LB simulation on the tube radius of $r = 10$ (in lattice units) in cross-sectional and LB density-based approaches,

the predicted P_c is within 7% and 18%, respectively, of the theoretical value coming from Young-Laplace equation. Thus, the cross-sectional approach is preferred wherever the radius of interface can be captured. However, this is not always the case in 3D LB simulation on PN configurations such as pore-body filling events in triangular elements.

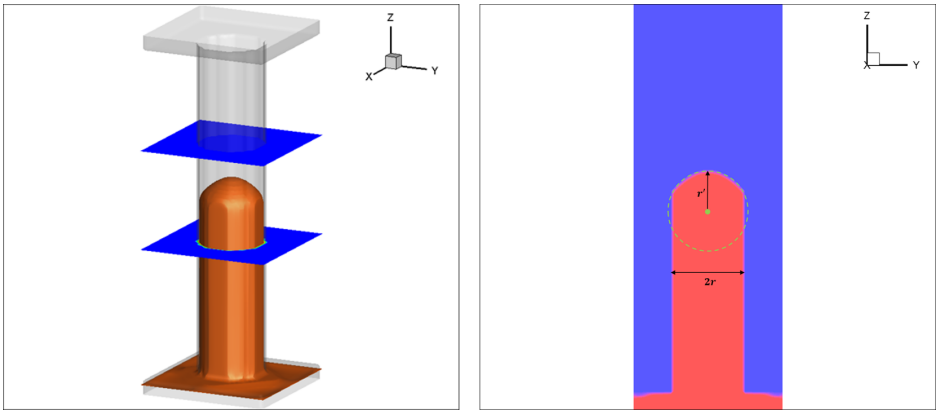

Figure 4.7: A validation of LB simulation on a simple piston-type displacement in a cylindrical tube for calculation of local capillary pressure: (left) CO_2 is in red, brine is transparent, and the blue planes define the bounds of calculation box, (right) cross-sectional view parallel to yz-plane through the center of tube to capture the radius of interface.

In Fig. 4.8, the resulting P_c from LB simulation of the simple piston-type displacement in a cylindrical tube is calculated and compared with the theoretical values based on Young-Laplace equation for different radii ($r = 5$, $r = 10$, $r = 15$, $r = 20$ in lattice units). The results show a good agreement, thereby giving us confidence in the procedure for calculation of P_c based on the order parameter and densities in lattice unit is feasible in 3D LB simulations.

Moreover, the described procedure is straightforward to implement and can be used in cases where the resulting interface has a 3D complex shape and it is not feasible to identify the interface in a cross-sectional approach. In following Sections 4.5.1.1 and 4.5.1.2, we present the LB simulation results on PN configurations plus the modified models of pore-body filling and snap-off events during imbibition that will be used in the quasi-static PN flow solver.

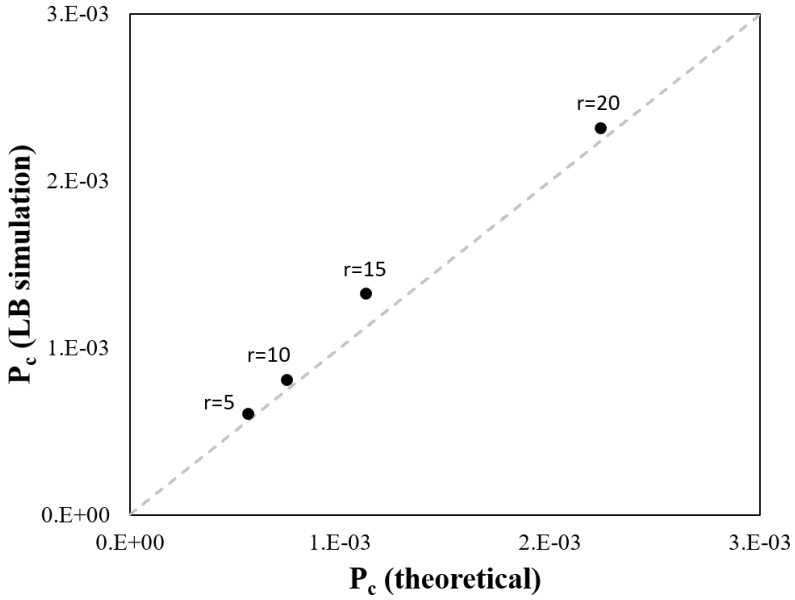

Figure 4.8: Comparison of calculated P_c from LB simulation and theoretical P_c on different radii of a cylindrical tube.

4.5.1.1 Simulation of pore-body filling

Three different TPT configurations with different shape factors but equal radius of inscribed circle and the connection number of 4, shown in Fig. 4.9, are studied to model the I_1, I_2, I_3 events during imbibition process. The average connection number of PNs from various rock samples is usually within the range of 3–5. Therefore, the choice of connection number of 4 is close to a realistic average value. In addition, having 4 connecting pore-throats allows to include pore-body filling events up to order 3. As explained in Section 4.3.4, lower orders of pore-body filling have higher threshold P_c and are more favorable than higher orders pore-body filling (I_{4+}). The higher orders of pore-body filling usually have a small number of occurrences and less important with respect to trapping. Thus, we focus on lower orders of pore-body filling in the LB simulations. This would help in avoiding geometric complexity in PN configurations and focusing on key factors in the filling process such as shape factor and corner half-angles.

The cross section of pore-body is defined as a triangle with three different shape factors with their corresponding corner half-angles, as listed in Table 4.1. The cross section of pore-throats in all cases are defined as square-shape to reduce the complexity and ensure a simultaneous invasion from different

connecting pore-throat across different configurations. This is achieved by designing configurations in a way that all pore-throats have the same cross section and path length from the inlet or outlet reservoirs to the pore-body, as depicted in Figs. 4.9 and 4.10. The inscribed radii of all pore-throats are equal and the geometric aspect ratio between pore-body and pore-throat is 5.

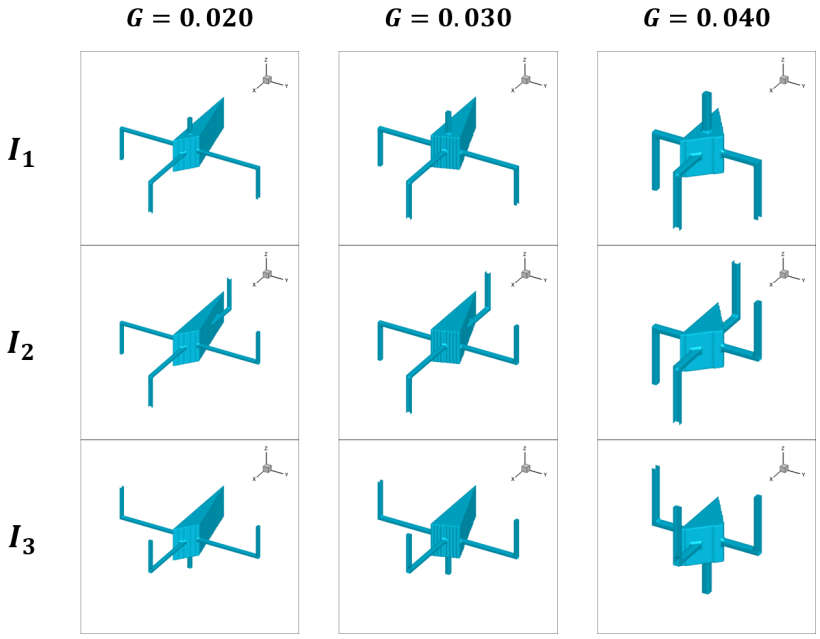

Figure 4.9: Pore-body filling configurations for the three studied shape factors $G = 0.020$, $G = 0.030$, $G = 0.040$ during I_1, I_2, I_3 events.

In LB flow simulation on all of these configurations, the inlet reservoir is connected to bottom pore-throats and the outlet reservoir is connected to top pore-throats, and the flow is always in +z (upward) direction. Initially, drainage simulation is implemented that results in CO_2 occupying the center of pore elements. Then, brine is injected from the same inlet reservoir to displace the CO_2 from the pore-body. The boundary conditions in both drainage and imbibition cycles are velocity inlet and pressure outlet that allow a faster flow simulation through the configuration. Fig. 4.11 shows an example of LB simulation of pore-body filling during drainage and imbibition processes on a triangular TPT configuration, shown in Fig. 4.10, with the shape factor of $G = 0.040$ during I_1 event. While the pore-body filling event is a dynamic process, we can track the saturation of CO_2 in the pore body in order to specify the relevant time step for the evaluation of threshold P_c.

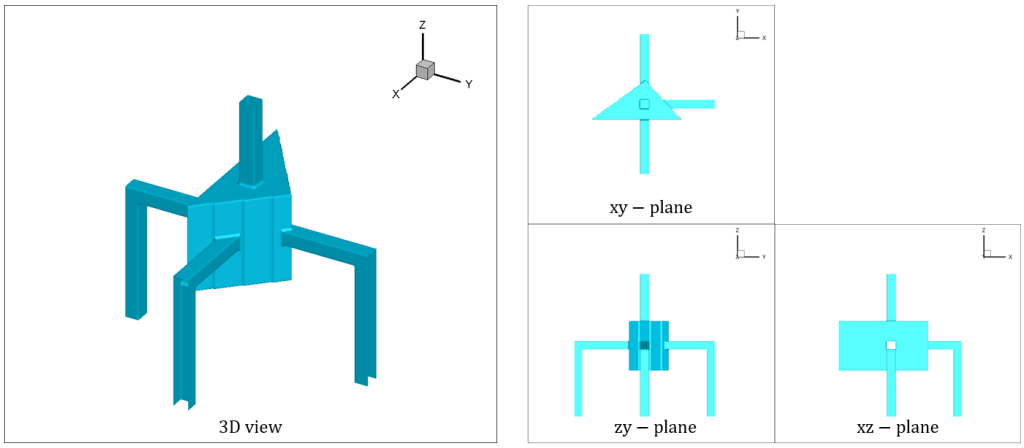

Figure 4.10: Pore-body filling configuration for the shape factor of $G = 0.040$ designed for modeling I_1 events from different angles. The equal length and cross section of pore-throats provide a desired simultaneous invasion.

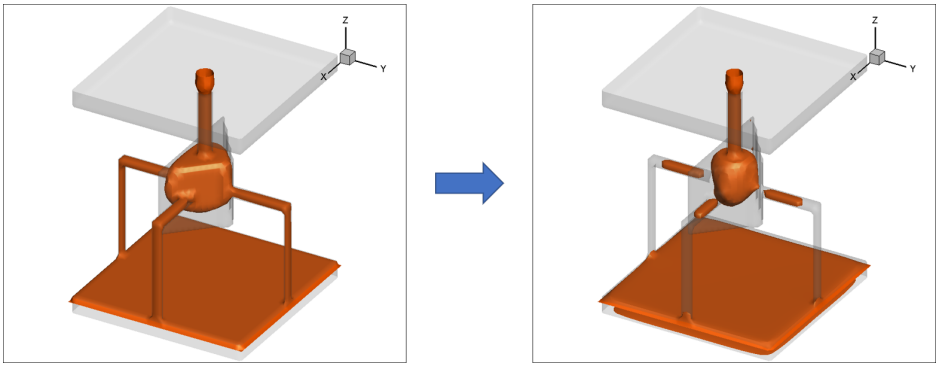

Figure 4.11: Pore-body filling during drainage (left) and imbibition (right) processes on a triangular TPT configuration with the shape factor of $G = 0.040$ during I_1 event.

We choose the saturation of 0.50, when half of the CO_2 is displaced, as the time step of calculation threshold P_c as described earlier. The described procedure is applied on all configuration of Fig. 4.9 and the corresponding P_c is computed. The dimensionless capillary pressure in pore-body ($\hat{P}_c$) is defined as:

$$\hat{P}_c = P_c \frac{r_p}{\sigma} \tag{4.10}$$

In Eq. 4.10, r_p is the inscribed radius of pore-body and σ is the surface tension. This definition makes the analysis more straightforward since the conversion from lattice unit to physical unit is not necessary.

We propose the threshold local capillary pressure of pore-body filling event in a similar format to conventional models (e.g., Valvatne and Blunt (2004)) but with some new parameters as:

$$\hat{P}_{c_i} = 2cos(\theta) - \left(\frac{r_p}{G\bar{r}_t} \times a'_i \times C_{f_i} \right) \tag{4.11}$$

In Eq. 4.11, the subscript i refers to the order of pore-body filling event. C_{f_i} is defined as filling factor that comes from the analysis of LB simulations of PN configurations. a'_i is defined as effective aspect ratio of the pore-body which is similar to classic definition of geometric aspect ratio but it considers just the invading pore-throats rather than all connecting ones. Therefore, a'_i can be a function of filling event and it involves the radius of invading pore-throat during the pore-body filling event.

In order to use this model, one needs to know C_{f_i} for different orders of filling on different shape factors of pore-body. We consider $C_{f_1} = 1$ the same as conventional models. In order to evaluate C_{f_2} and C_{f_3}, we define the ratio of $\hat{P}_{c_i}$ of events with respect to $\hat{P}_{c1}$ as:

$$f_{21} = \frac{\hat{P}_{c_2}}{\hat{P}_{c_1}} \tag{4.12}$$

$$f_{31} = \frac{\hat{P}_{c_3}}{\hat{P}_{c_1}} \tag{4.13}$$

If we combine Eqs. 4.11-4.13, the filling factors can be described as:

$$C_{f_2} = \frac{2G\bar{r}_t cos(\theta)(1 - f_{21})}{r_p a'_2} \tag{4.14}$$

$$C_{f_3} = \frac{2G\bar{r}_t cos(\theta)(1 - f_{31})}{r_p a_3'} \tag{4.15}$$

Therefore, by having $\hat{P_{c_i}}$ of different events from LB simulation, one can compute the corresponding f_{i1} and use Eqs. 4.14-4.15 to obtain the filling factors of the modified model.

Table 4.3 presents the resulting dimensionless local capillary pressure of pore-body filling events (I_1, I_2, I_3) for the studied shape factors. The $\hat{P_{c_i}}$ are used to calculate the capillary pressure ratios (f_{i1}) and the filling factors (C_{f_i}) next, as listed in Table 4.4.

Table 4.3: The resulting dimensionless local capillary pressure ($\hat{P_{c_i}}$) of pore-body filling events from LB simulations on PN configurations.

Shape factor	$\hat{P_{c_1}}$	$\hat{P_{c_2}}$	$\hat{P_{c_3}}$
G=0.020	2.020	1.514	0.984
G=0.030	1.884	1.362	0.859
G=0.040	1.433	0.994	0.614

Table 4.4: The resulting filling capillary pressure ratios (f_{i1}) defined in the modified pore-body filling model from LB simulations on PN configurations.

Shape factor	I_2 filling	I_3 filling
G=0.020	$f_{21} = 0.750$	$f_{31} = 0.487$
G=0.030	$f_{21} = 0.723$	$f_{31} = 0.456$
G=0.040	$f_{21} = 0.694$	$f_{31} = 0.428$
Conventional	$f_{21} = 0.676$	$f_{31} = 0.412$

The results in Table 4.4 are used to describe the filling factor as a function of shape factor and incorporate it into a quasi-static PN flow solver where pore-body filling events of I_1 and I_2 are modified with Eq. 4.11, accordingly

4.5.1.2 Simulation of snap-off

The three different shape factors of $G = 0.020$, $G = 0.030$, $G = 0.040$ on triangular cross sections in a PTP configuration, shown in Fig. 4.12, are studied to investigate the threshold capillary pressure during snap-off event. The focus is the cross section of the center of the pore-throat. We first implement drainage simulation with receding contact angle (10°) followed by imbibition simulation with with advancing contact angle (60°). These values

are based on Morrow's contact angle hysteresis model (Morrow et al. 1975) for intrinsic contact angle of 56°. The model relates the intrinsic contact angle to receding and advancing ones. The boundaries are connected to bounding pore-bodies and a pressure-driven flow is implemented in the LB simulation.

We propose the threshold capillary pressure of snap-off event in a similar format to the conventional snap-off models but with having a new correction factor:

$$\hat{P}_c = cos(\theta) - C_i sin(\theta) \tag{4.16}$$

In Eq. 4.16, C_i is defined as the snap-off factor and $\hat{P}_c$ is defined similar to Eq. 4.10 (r_p replaced with r_t). In conventional models, C_i can be described in terms corner half-angles:

$$C_i = \frac{2}{cot(\beta_1) + cot(\beta_2)} \tag{4.17}$$

However, we carry out LB simulation for different shape factors, depicted in Fig. 4.12, to find C_i as a function of G coming from two-phase flow simulation of CO_2 and brine with appropriate contact angle. The drainage invasion of CO_2 into the PTP configurations are implemented first. Then, the gradual imbibition of brine is implemented via an incremental increase of the imposed pressure difference. This would allow the brine in corners to expand gradually prior to snap-off in the pore-throat, as shown in the cross section of pore-throat in Fig. 4.13.

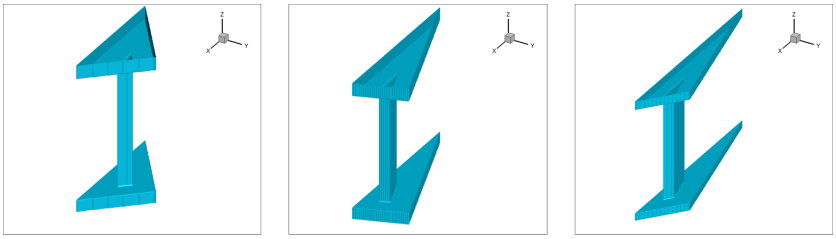

Figure 4.12: PTP configurations with different shape factors defined for assessing the snap-off event in the pore-throat: (a) $G = 0.040$ (b) $G = 0.030$ (c) $G = 0.020$.

A cross-sectional analysis is applied on the results from LB simulation to obtain the radius of curvature in each corner, as illustrated in Fig. 4.14, during the snap-off event. The minimum radius among three is used in the

form of Young-Laplace equation ($P_c = 2\sigma cos(\theta)/r'$) to evaluate the threshold local capillary pressure of the pore-throat:

$$r' = min\left\{r'_1, r'_2, r'_3\right\} \tag{4.18}$$

In Eq. 4.18, r'_i refers to the calculated radius of curvature in each corner of the pore-throat, as shown in Fig. 4.14. On the other hand, by defining the local capillary pressure of snap-off in the form of Eq. 4.16, one can relate the correction factor of C_i to the radius of curvature r' from LB simulation results:

$$C_i = \frac{1 - 2r_t/r'}{tan(\theta)} \tag{4.19}$$

In Eq. 4.19, r_t refers to the inscribed radius of the pore-throat (a purely geometric parameter) while r' refers to the minimum radius of curvature of the interface right before snap-off event in the pore-throat (coming from LB simulation results).

Table 4.5 presents the resulting snap-off factors from LB simulation on PTP configurations for the three studied shape factors. Although only three shape factors are evaluated, it covers a range from 0.020 to 0.040 using linear interpolation. This range of shape factor is sufficient to include the majority of both pore-bodies and pore-throats across various pore-networks of different samples.

Table 4.5: The resulting snap-off factor (C_i) as a function of shape factor from LB simulations on PTP configurations compared with the conventional model.

Shape factor	Conventional model	Modified model
G=0.020	$C_i = 0.167$	$C_i = 0.163$
G=0.030	$C_i = 0.274$	$C_i = 0.213$
G=0.040	$C_i = 0.373$	$C_i = 0.337$

4.5.2 Pore-network flow simulation

4.5.2.1 Rock samples and extracted pore-networks

In this study, two natural rock samples of Berea sandstone and Mt. Simon sandstone are selected to investigate residual trapping of CO_2. The former

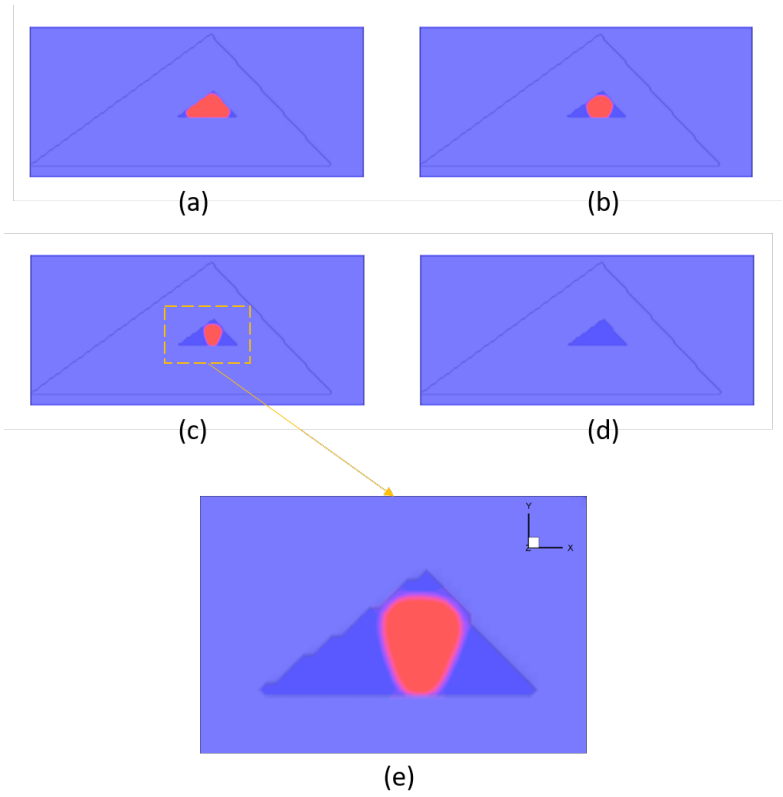

Figure 4.13: Cross section of a pore-throat with $G = 0.040$ during snap-off event: (a) beginning of imbibition (b) moving the interface toward the center (c) before snap-off (d) after snap-off (e) higher resolution of pore-throat cross section.

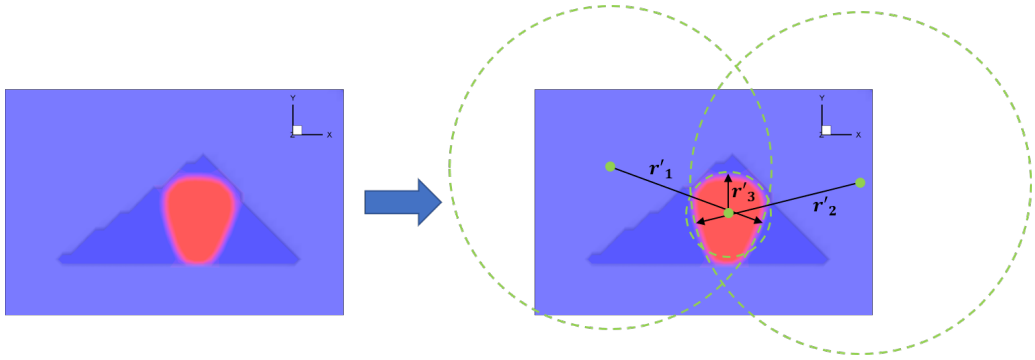

Figure 4.14: Cross-sectional approach in evaluation of capillary pressure of snap-off event based on the radius of curvature of three corners of a triangular pore-throat with $G = 0.040$.

sample was the focus of an experimental study of measurement of contact angle between CO_2 and brine by Dalton et al. (2018). The latter sample was the focus of a rock characterization study and CO_2-brine flow simulation with different approaches by Kohanpur et al. (2020) and covered in Chapter 2. The core plugs of both samples were scanned by micro-CT imaging technique at the National Energy Technology Laboratory (NETL) which produced a series of grayscale scans. These scan are processed through several steps of image processing in Fiji (Schindelin et al. 2012) to filter and smooth images in order to distinguish existing image phases (solid, pores, CO_2, brine) from each other via thresholding algorithms. Table 4.6 presents the information of the studied sandstone samples.

Table 4.6: Studied samples for pore-network CO_2-brine flow simulation of drainage-imbibition cycle.

Sample	Porosity	Res. (μm)	Size (mm^3)	Study
Berea sandstone	0.202	2.36	$1.89 \times 1.89 \times 1.42$	Dalton et al. (2018)
Mt. Simon sandstone	0.263	2.80	$1.40 \times 1.40 \times 1.40$	Kohanpur et al. (2020)

The micro-CT images of the Berea sandstone sample also included post-imbibition scans with residual CO_2 and the distribution of contact angle. Table 4.7 describes the experimental measurements from this sample. The contact angle average (55.9°) and standard deviation (15.5°) come from measurement on 40 slices of micro-CT images. The distribution of these measured contact angles from different locations of the sample are represented in Fig. 4.15. More details can be found in Dalton et al. (2018).

Fig. 4.16 shows an example of post-imbibition grayscale image (left figure) and its corresponding segmented image (right figure) which is consist of three image phases: solid in white, CO_2 in black, brine in gray. It is obtained via a ternary segmentation implemented in Fiji, which is the result of two sequential binary segmentation on dry scans and post-imbibition scans in order to obtain their differences and extract the distribution of CO_2. Fig. 4.17 shows the 3D representation of the pore structure (left figure) and residual trapping CO_2 after imbibition (right figure) in the Berea sandstone sample.

Here, we use the PN extraction code based on Maximal Ball (MB) algorithm from Dong and Blunt (2009) and Raeini et al. (2017) to obtain cor-

Table 4.7: Experimental data of the Berea sandstone sample.

Property	Value
Residual CO_2 saturation after imbibition	0.339
Contact angle, average*	55.9° (brine-wet)
Contact angle, standard deviation*	15.5°

* Measurement on 40 micro-CT images

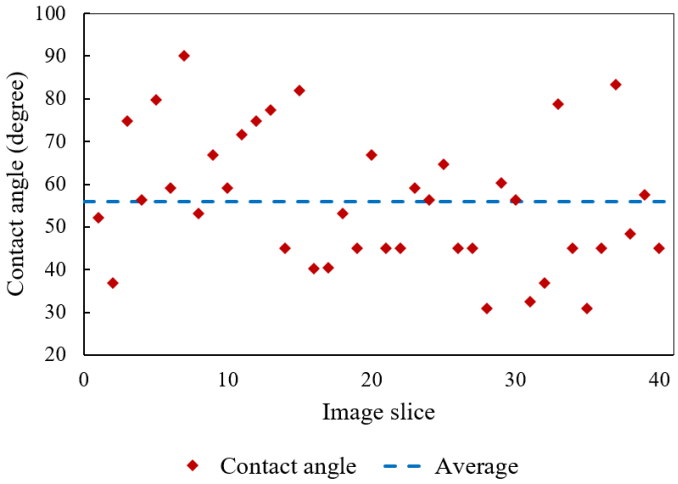

Figure 4.15: The distribution of measured contact angles from different locations of the sample based on 40 slices of micro-CT images. The dash line is the average value.

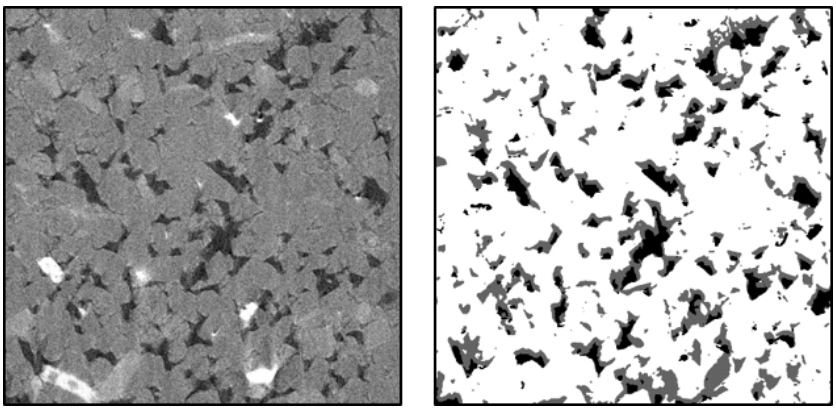

Figure 4.16: A slice of micro-CT images of the Berea sandstone sample with residual CO_2. The left figure is the raw grayscale slice. The right figure is the ternary segmented slice where solid part is in white, CO_2 is in black, and brine is in gray.

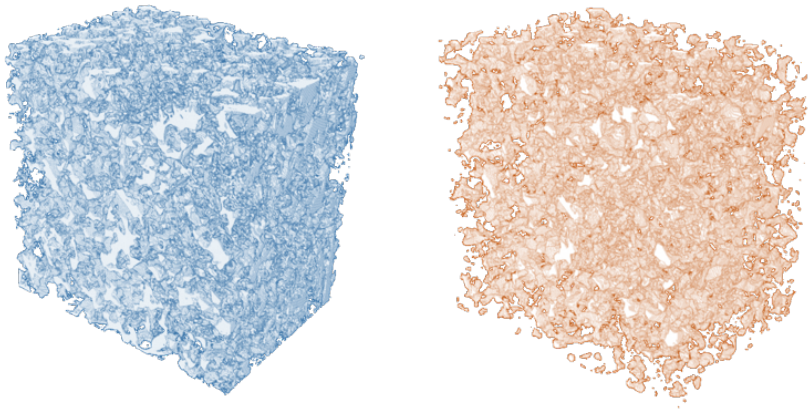

Figure 4.17: Comparison 3D representation of the pore structure (left) and residual trapping CO_2 after imbibition (right) in the Berea sandstone sample

responding PNs of rock images. The algorithm was originally introduced by Silin and Patzek (2006) where the entire 3D voxelized pore space is searched to find the largest possible voxelized spheres, known as MBs. This PN extraction tool can provide the inherit randomness of pore structure in real rocks with a wide range of connection number for pore-bodies. More details of this PN extraction tool can be found in Dong and Blunt (2009). The output of this tool is geometrical and topological information of pore-bodies and pore-throats including the location, radius, volume, length, total length, and shape factor. Fig. 4.18 shows the 3D representation of the Berea sandstone sample (left figure) and its extracted PN (right figure) via MB algorithm. Table 4.8 lists the properties of extracted PNs of the studied samples. The reported absolute permeabilities come from using the Valvatne and Blunt (2004) PN flow solver.

Table 4.8: Extracted pore-network information of the studied sandstone samples.

Sample	Berea	Mt. Simon
Number of pore-bodies	6207	2566
Number of pore-throats	10160	6349
Average connection number	3.18	4.85
Absolute permeability	455 mD	4201 mD

As mentioned earlier, the shape factor (Eq. 4.4) in PN models is a metric of irregularities of the pore space in pore elements. Fig. 4.19 shows the shape

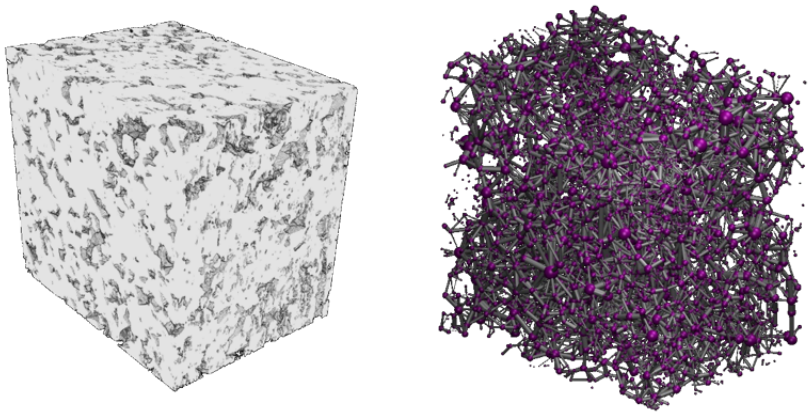

Figure 4.18: 3D representation of the Berea sandstone sample (left) and its extracted pore-network from maximal-ball algorithm (right).

factor distribution of pore-bodies (left plot) and pore-throats (right plot) in the extracted PN of the Berea sandstone sample. The distribution in both follows approximately a normal distribution with the average of 0.0298 and 0.0312 and standard deviation of 0.0078 and 0.0064 for pore-bodies and pore-throats, respectively. Therefore, these distributions justify the selected values of shape factors (Table 4.1) in PN configurations studied in Section 4.4.1.

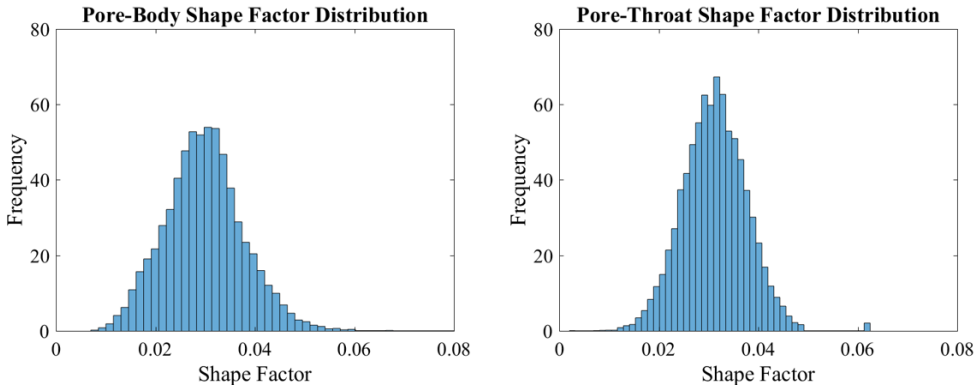

Figure 4.19: Shape factor distribution of pore elements in the extracted pore-network of the Berea sandstone sample: (left) pore-body shape factor distribution, (right) pore-throat shape factor distribution.

Here, we present detailed results from the CO_2-brine flow simulation on both sandstone samples with properties listed in Table 4.2. We use a modified PN flow solver that includes the new pore-level models described in Sections 4.5.1.1 and 4.5.1.2 and compare its outputs with results from the original PN flow solver in conventional models.

In order to incorporate the measured contact angles, shown in Fig. 4.15, in the quasi-static PN flow model, one can use the arithmetic average of data distributed uniformly in pore elements or fit a distribution function and assign values randomly in pore elements. We fit a Weibull distribution function on the available contact angle data in the range of 30–90° and use it as the equilibrium contact angle in the input data of PN flow model. We compare it with the PN flow model with a uniform contact angle of 55.9° (the average value). Table 4.9 shows the resulting residual trapped CO_2 after a drainage-imbibition cycle on the Berea sandstone sample. While in both distributions, the modified model predicts closer to the experimental saturation, the uniform average value of contact angle results a better agreement compare to the Weibull distribution. Therefore, we present the PN flow results based on the uniform average value of contact angle in next sections on both samples.

Table 4.9: Comparison of uniform average and Weibull distribution of contact angle in terms of residual trapped CO_2 after a drainage-imbibition cycle on the Berea sandstone sample.

CO_2 saturation	Uniform average value	Weibull distribution
Original model	0.437	0.542
Modified model	0.375	0.482
Experimental	0.339	

Since no measured experimental data of residual trapped is available on the Mt. Simon sandstone sample, introduced in Table 4.6, we carry out LB simulations of drainage and imbibition processes (as explained in Chapter 2) on the rescaled 3D rock images with contact angle of 55.9° and capillary number of 5×10^{-5} to obtain the saturation at the end of drainage and residual trapped CO_2 at the end of imbibition. Fig. 4.20 shows the resulting distribution of CO_2 at the end of drainage and imbibition processes on the Mt. Simon sandstone sample. The corresponding saturations of CO_2 at these points are $S_{nw}^{drain.} = 0.60$ and $S_{nw}^{imbib.} = 0.14$, respectively. Thus, we use this $S_{nw}^{drain.}$ (i.e., $S_{w}^{init.} = 0.40$) as the end point of drainage simulation in the PN flow solver, and we compare the $S_{nw}^{imbib.}$ with the resulting residual saturation at the end of imbibition from PN flow simulation.

In the following, the statistics of pore-level events during imbibition on both samples are investigated in Section 4.5.2.2. Then, results of residual trapping of CO_2 and relative permeability curves during drainage and imbi-

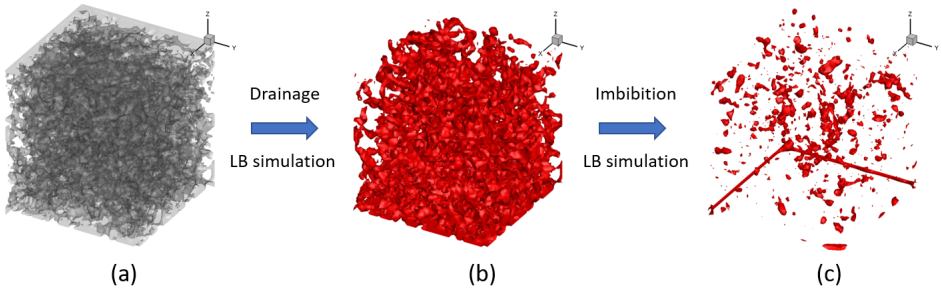

Figure 4.20: LB simulations of drainage and imbibition processes on the Mt. Simon sandstone sample to obtain end point saturations. (a) pore space of the sample (b) end of drainage process (c) end of imbibition process. CO_2 is shown in red. Brine and rock are not rendered.

bition processes are discussed in Sections 4.5.2.3 and 4.5.2.4, respectively.

4.5.2.2 Statistics of pore-level events

We carried out drainage and imbibition cycles via quasi-static PN flow simulation that incorporates the modified models introduced in Sections and 4.5.1.1 and 4.5.1.2. In each step of imbibition process, piston-type displacement, pore-body filling, and snap-off occur across the PN. The cumulative statistics of these events during imbibition PN steps on the Berea and Mt. Simon sandstone samples are presented in Figs. 4.21 and 4.22, respectively. These statistics are compared for the results from the original PN model and the modified model.

In the Berea sandstone sample, the modified model predicts higher number of piston-body filling events (6.3% more) and piston-type displacement in pore-throats (15.6% more). On the hand, it predicts smaller number of snap-off events compare to the original model (7.3% less). Therefore, we expect to see a more frontal invasion pattern in the modified model which can translate into less chance of trapping CO_2. This is also in agreement with reported residual saturation in Table 4.10.

In the Mt. Simon sandstone sample, a similar pattern with a slight change between the modified and original models is also resulted. The modified model predicts higher number of piston-body filling events (9.4% more) and piston-type displacement in pore-throats (10.7% more) while smaller number of snap-off events are predicted compare to the original model (7.2% less).

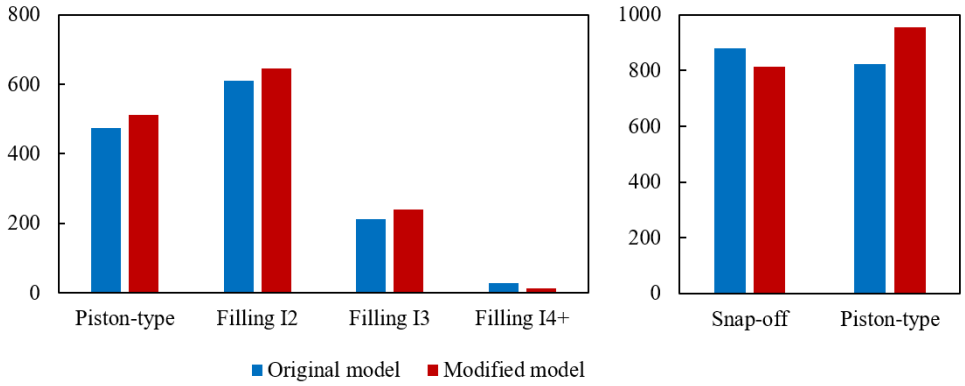

Figure 4.21: Statistics of number of pore-level events in pore-bodies (left) pore-throats (right) of the Berea sandstone sample.

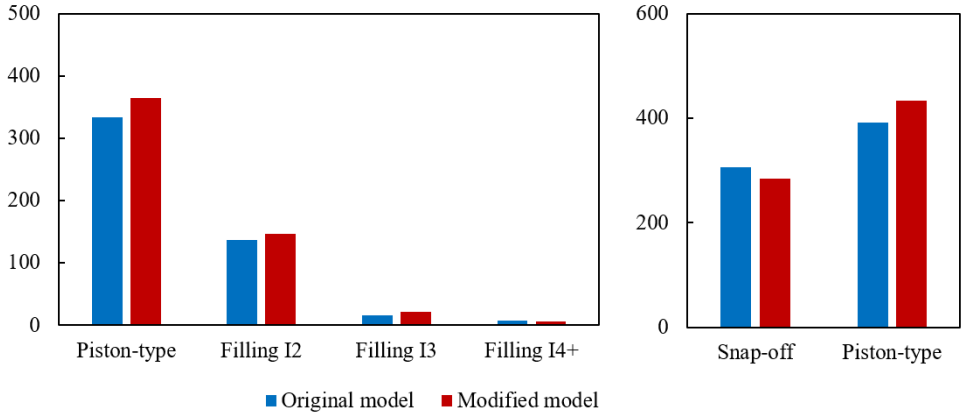

Figure 4.22: Statistics of number of pore-level events in pore-bodies (left) pore-throats (right) of the Mt. Simon sandstone sample.

4.5.2.3 Residual trapping

In PN simulation of drainage-imbibition cycle, the end point of drainage process corresponds to maximum macroscopic capillary pressure which is also the starting point of imbibition process. This drainage end point can be a control parameter in terms of trapped wetting phase saturation in the quasi-static PN flow model. The resulting saturation of trapped non-wetting phase at the end of imbibition follows a hysteresis behavior based on the initial saturation in the imbibition process. Therefore, a trapping curve can be produced via the PN flow solver similar to Land's initial-residual trapping model (Land et al. 1968) where initial and residual saturations are related.

In Fig. 4.23, the residual trapping curve of CO_2-brine flow in the Berea sandstone sample is compared between the original and modified PN models. For the original PN model, the resulting residual saturation of brine is about 0.56 (that is, 0.44 for CO_2) when the initial brine saturation is small (for about $S_w^{init.} < 0.40$). For the modified PN model, the resulting residual saturation of brine is about 0.63 (that is, 0.37 for CO_2) when the initial brine saturation is small (for about $S_w^{init.} < 0.40$). Both models refer to a drainage process with displacements and invaded elements that leaves a relatively small saturation of brine in the PN, mainly in corners and small or isolated pore elements. Fig. 4.23 implies that such a drainage process will be followed by an imbibition process with higher trapped CO_2. On the other hand, for values of $S_w^{init.} > 0.40$ the residual saturation of brine increases which means less trapped CO_2.

For the Berea sandstone sample, we chose $S_w^{init.} = 0.20$ (mid-point of the beginning of the trapping curve) as the start point of imbibition process in the quasi-static PN flow solver since no experimental value is available. The reported statistics of events in Section 4.5.2.2 were also based on the $S_w^{init.} = 0.20$. The resulting residual trapping of CO_2 after imbibition is presented in Table 4.10 where the modified model is compared with the original model. The residual saturation of CO_2 is also compared with an experimental value based on analysis of volume ratio of CO_2 in X-ray micro-CT scans rendered in Fig. 4.17. The modified model predicts residual saturation of trapped CO_2 within 10% of the experimental values while the error from the original model is about 29%. The number of trapped pore elements and regions in the PN is also reported in Table 4.10 for each model which is correlated with

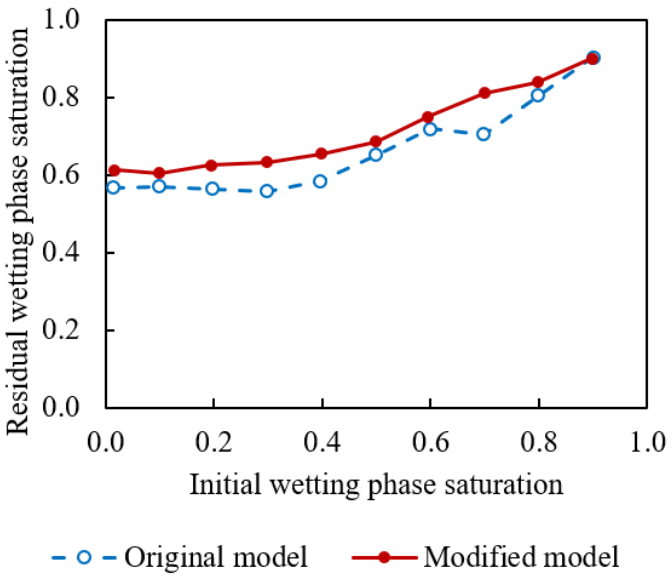

Figure 4.23: Residual trapping curve from pore-network modeling of CO_2-brine flow in the Berea sandstone sample.

the residual saturation of CO_2.

Table 4.10: Comparison of the original and modified pore-network flow models on the Berea sandstone sample based on predicted residual trapping of CO_2 after imbibition.

Residual trapping	CO_2 saturation	No. of regions	No. of elements
Original model	0.437	588	2754
Modified model	0.375	539	2627
Experimental CO_2 saturation		0.339	

For the Mt. Simon sandstone sample, we chose $S_w^{init.} = 0.40$ based on the LB simulations shown Fig. 4.20. The resulting residual trapping of CO_2 after imbibition is also presented in Table 4.11 and compared with the residual saturation from LB simulation. The overall prediction error is higher on the Mt. Simon sandstone sample compare to the Berea sandstone sample that can be due to numerical errors in both LB imbibition simulation and PN flow models.

In both studied samples, the modified model outperforms the original model and predicts the residual trapping in better agreement with the experimental or LB simulation value since it predicts less number of snap-off events in pore-throats, as shown in Figs. 4.21 and 4.22.

Table 4.11: Comparison of the original and modified pore-network flow models on the Mt. Simon sandstone sample based on predicted residual trapping of CO_2 after imbibition.

Residual trapping	CO_2 saturation	No. of regions	No. of elements
Original model	0.282	110	744
Modified model	0.248	98	612
LB simulation CO_2 saturation		0.141	

4.5.2.4 Relative permeability curves

The relative permeabilities of the CO_2-brine flow during drainage and imbibition processes on the Berea sandstone sample are presented in Figs. 4.24 using original and modified PN flow models. The different statistics of pore-level events results in a different invasion pattern that corresponds to a different average flow rates across the PN which translates into different relative permeability values at each saturation point. In these plots, the difference in resulting residual saturation is also clearly seen as the point where no flow occurs and by definition, the relative permeability is zero.

A similar procedure is applied on the Mt. Simon sandstone sample using original and modified PN flow models and its resulting relative permeabilities are shown in Fig. 4.25. The change in the imbibition relative permeability curves of the Mt. Simon sandstone sample is less noticeable than the Berea sandstone sample. This is because the connectivity of the Mt. Simon sandstone sample is higher (average connection number 3.18 vs. 4.85) and the CO_2 trapping is smaller compared to the Berea sandstone sample. Recall that more connections and pore-throats for each pore-body results in higher chance of escaping during filling events of imbibition process. Therefore, the CO_2 trapping is less sensitive to the implemented modifications into the model.

In both studied samples, the CO_2 relative permeability is higher in the modified model compare to the original model. This can be justified by the reduction in snap-off events and trapped CO_2 that results a more frontal displacement during imbibition process with higher macroscopic flow rate of CO_2 across the PN.

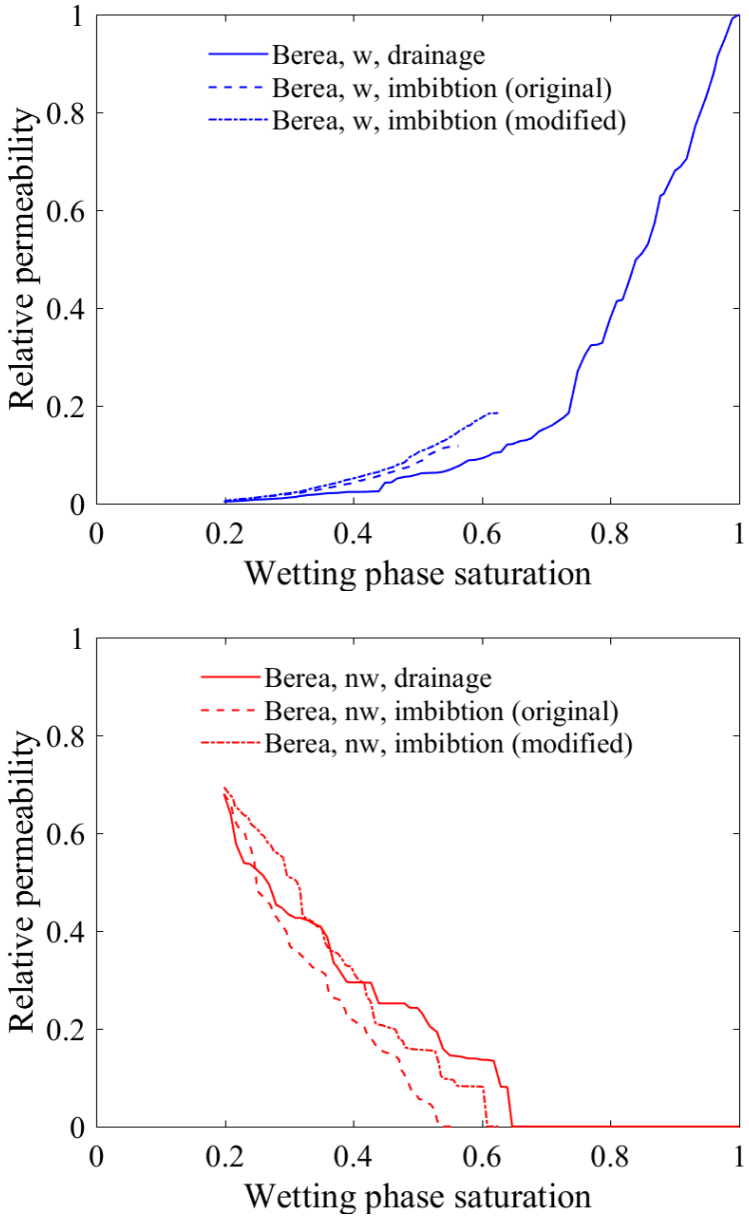

Figure 4.24: Relative permeability curves of CO_2-brine flow in the Berea sandstone sample using original and modified imbibition models: (top) brine curves as the wetting phase, (bottom) CO_2 curves as the non-wetting phase.

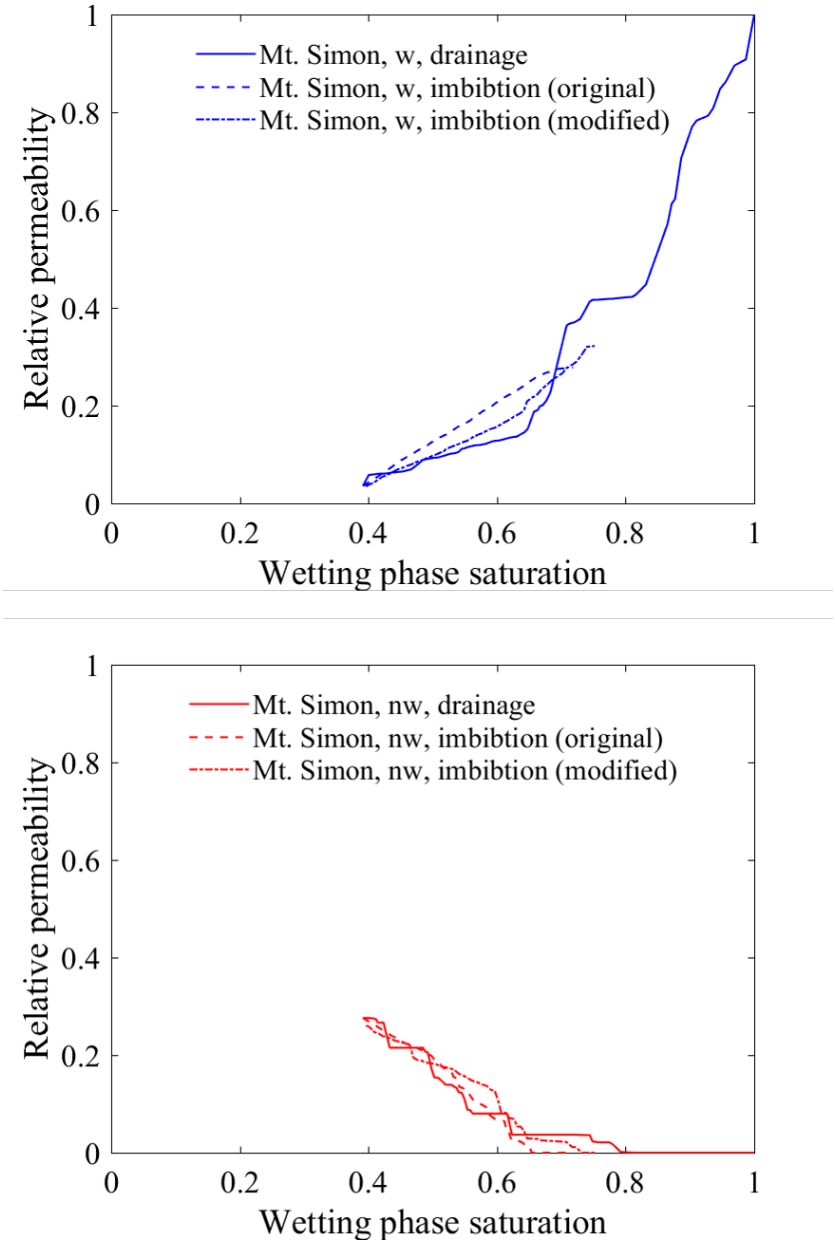

Figure 4.25: Relative permeability curves of CO_2-brine flow in the Mt. Simon sandstone sample using original and modified imbibition models: (top) brine curves as the wetting phase, (bottom) CO_2 curves as the non-wetting phase.

4.6 Summary and conclusions

The physics of CO_2-brine flow at pore-scale is a key part of prediction of amount and fate of residual trapped CO_2 in geological storage of CO_2 in deep saline reservoirs. The description of this flow system in the form of pore-level flow models through pore-bodies and pore-throats of an extracted PN from micro-CT images of real rock is a practical approach to obtain important characteristic curves during a drainage-imbibition cycle. However, this description can be improved by more specific and accurate relations for CO_2-brine flow that can come from DNS methods. This study presented a new set of pore-level flow models during pore-body filling and snap-off events of imbibition process in PN modeling of CO_2-brine flow. LB simulations were carried out on several designed PN configurations and the thresold local capillary pressure was evaluated to develop modified equations of threshold capillary pressure as a function of shape factor, which was not proposed in other models in the literature. We also defined effective aspect ratio of pore-body filling as a new parameter in the modified model.

The modified equations of local capillary was incorporated in a quasi-static PN solver. This modified model resulted a new pattern of invasion during imbibition process due to a different order of competing pore-level events compare to the original model. We applied the modified model on extracted PNs of a two sandstone samples (Berea and Mt. Simon) to obtain relative permeabilities and saturation of residual trapped CO_2 after a drainage-imbibition cycle. The statistics of pore-level imbibition events changed by replacing the original model with the modified model. The occurrence of snap-off in pore-throats was reduced by about 10% which means more frontal displacement pattern across the sample. As a result, our modified model was in closer agreement than the original model based on the comparison of the residual trapped CO_2 with experimental and DNS data. The relative permeabilities were also computed based on the modified model for both sandstone samples. The higher connectivity of pore structure in the Mt. Simon sandstone sample resulted less difference in relative permeabilities due to model modification.

Additional future work can be performed by comparing predicted relative permeabilities with experimental or high resolution DNS measurements. Also, the effect of lattice resolution and capillary number in LB simulations

can be studied. This can lead to some changes in the results and the proposed modified model. A preliminary study is discussed in Appendix B on one shape factor and can be extended to more shape factors and other PN configurations.

Chapter 5

Epilogue

5.1 Conclusions

This dissertation presents a computational modeling framework to address current challenges in pore-scale modeling of two-phase flow with applications to sequestration of carbon dioxide (CO_2) in deep saline geological formations. These formations are widely available and have relatively high storage capacity to host injected CO_2 for long-term as a practical solution to reduce CO_2 emissions from fossil fuel power plants. Due to the expense and complexity of experimental investigations, computational approaches have been developed to understand the physics of CO_2-brine flow at the pore-scale. The dissertation considers both direct numerical simulation on real rock geometry measured by X-ray scans, as well as PN models which simplify the geometry as a connection of pore-bodies and pore-throats with idealized shapes. Both approaches are challenged in applications to large heterogeneous core plugs.

In Chapter 2, a heterogeneous Mt. Simon sandstone sample from a pilot CO_2 injection project was extensively studied in terms of characterization of morphology and simulation of single-phase and two-phase flow of CO_2 and brine. 3D rock images coming from X-ray micro-CT scans were investigated to assess the size of the REV and sample heterogeneity. Three distinct simulation approaches were applied to simulate the drainage process: PN modeling on a PN extracted from the scans, and two different methods for direct numerical simulation on the rock geometry, namely the LB method, and the finite-volume method using OpenFOAM. The relative permeabilities during displacement of brine by CO_2 were computed and compared using different measurement choices for the direct numerical simulations, i.e., the steady-state approach for LB and unsteady approach for OpenFOAM. They

were also compared with the prediction from computationally more efficient quasi-static PN flow model. All approaches were in close agreement with one another for low capillary number. The accuracy, computational efficiency, and the effect of the resolution of the computational grids were also compared for low and relatively high capillary numbers.

In Chapter 3, a novel pore-network stitching method (PNSM) was developed that combines the inherent simplicity of PN modeling with statistical PN generation to characterize the heterogeneity of rock cores. The method overcomes technical limits on sample size to discern void space during X-ray scanning and computational limits on PN extraction algorithms by using the information from a few signature parts of the core and their extracted PNs. The workflow was validated on various types of natural rock samples and applied on large domain problems based on pore structure and flow properties including relative permeabilities of CO_2-brine flow. In each sample, multiple realizations were generated and the average results were compared with properties from defined reference PNs.

In Chapter 4, a new set of pore-level flow models during imbibition process in PN modeling were proposed to improve the prediction of residual trapping of the non-wetting CO_2 phase. This is important for assessing the long-term storage capacity and safety of geological sequestration. LB simulations were carried out on several PN configurations to investigate pore-body filling and snap-off events that are simplified in PN modeling. The local capillary pressure of these events was evaluated and modified equations of threshold capillary pressure were defined. The modified model was incorporated into an existing quasi-static PN flow solver and applied to a Berea sandstone sample to obtain relative permeabilities and saturation of residual trapped CO_2 after a drainage-imbibition cycle. The modified model was in closer agreement than the conventional model based on the comparison of the residual trapped CO_2 with the available experimental data. The modified model was also applied to the same Mt. Simon sandstone sample studied in Chapter 2. In this case, no experimental measurements of trapped CO_2 were available, unlike the Berea sandstone sample. A comparison with trapped CO_2 simulated by DNS again shows improved results for the modified PN model, though the results are not as good as for the Berea sandstone sample.

These studies together enable straightforward modifications to the current generation of PN models to improve accuracy and be more applicable in

practice. The PNSM enables study of large heterogeneous rock cores. The use of DNS to study multiphase flow physics in PN configurations enables modification of rules implemented in conventional PN models to improve accuracy of capturing trapping of CO_2 during imbibition process.

5.2 Future directions

5.2.1 Pore-network stitching method

In terms of inputs, the workflow can also include a robust method of detecting the signature parts of a heterogeneous core. It should be capable of addressing some possible challenges in its inputs as well, such as missing data in rock images or artifacts in coarse resolution scans. Recent advances in machine learning approaches in both image processing and integrating multi-scale images (Mohaghegh 2018; Karimpouli and Tahmasebi 2019; Tahmasebi et al. 2020) can be used in identification of signature parts of a large domain. Moreover, high-resolution thin-section images of cores can be used as inputs of 2D-to-3D reconstruction techniques (Tahmasebi and Sahimi 2012) to generate 3D images of signature parts as an alternative when micro-CT scanning of all signature parts is not feasible.

In terms of procedure, there were assumptions in various steps of the developed PNSM, such as averaging the PN parameters between two PNs or used distribution functions, that could be replaced with alternative averaging approaches and functions. The stochastic PN generator can be replaced with newer generations of PN generators based on deep learning approaches.

In terms of performance, the accuracy of PNSM can be assessed on a full core dataset including comprehensive multiscale CT scans with different resolutions and core-scale experimental measurements on relative permeabilities and other flow properties. The PNSM can also be tested in other applications of porous media, e.g., based on reactive transport properties or mechanical properties of the rock where the PN geometry should be updated with the simulation time to mimic the structural evolution of pore space.

5.2.2 Pore-level flow models

The PN configurations studied in Chapter 4 can be designed to be more complex and realistic by adding some geometric variabilities. Pore-body filling configurations can be assessed based on different connection numbers. Their connecting pore-throats can have a non-uniform distribution of aspect ratio. Also, the orientation of connecting pore-throats can be involved as a factor to be investigated in the modified model. The cross section of pore elements can be defined with more diverse shapes that still incorporates corner flow such as star-shape or higher order polygons. The analysis was done on just three selected shape factors due to computational limitations to obtain relations as a function of shape factor. However, this can be extended to more shape factors to obtain more accurate relations.

Moreover, the modified models were limited to new relations and factors with an experimentally measured contact angle in just threshold local capillary pressure of events. The flow relations of phases in different parts of PN configurations can also be studied and added to this framework including a wide range of contact angles. Such modifications can certainly have an impact on the predicted relative permeabilities.

Finally, we used LB as the DNS method to study the physics of CO_2-brine flow in PN configurations. It is also possible to do the analysis with another DNS method, e.g., finite-volume method, to assess the validity of findings. This can specifically be focused on areas where the color-fluid LB model has limitation, e.g., studying high density ratio problems. In addition, the effect of grid resolution and capillary number on results from DNS can be investigated further. A preliminary sensitivity analysis of LB simulation on PN configurations is discussed in Appendix B.

References

Aghaei, A. and Piri, M. (2015). Direct pore-to-core up-scaling of displacement processes: Dynamic pore network modeling and experimentation. *Journal of hydrology*, 522:488–509.

Ahrenholz, B., Tölke, J., Lehmann, P., Peters, A., Kaestner, A., Krafczyk, M., and Durner, W. (2008). Prediction of capillary hysteresis in a porous material using lattice-boltzmann methods and comparison to experimental data and a morphological pore network model. *Advances in Water Resources*, 31(9):1151–1173.

Al-Kharusi, A. S. and Blunt, M. J. (2007). Network extraction from sandstone and carbonate pore space images. *Journal of petroleum science and engineering*, 56(4):219–231.

Aljasmi, A. and Sahimi, M. (2020). Efficient image-based simulation of flow and transport in heterogeneous porous media: Application of curvelet transforms. *Geophysical Research Letters*, 47(2):e2019GL085671.

Andrä, H., Combaret, N., Dvorkin, J., Glatt, E., Han, J., Kabel, M., Keehm, Y., Krzikalla, F., Lee, M., Madonna, C., et al. (2013a). Digital rock physics benchmarks—part i: Imaging and segmentation. *Computers & Geosciences*, 50:25–32.

Andrä, H., Combaret, N., Dvorkin, J., Glatt, E., Han, J., Kabel, M., Keehm, Y., Krzikalla, F., Lee, M., Madonna, C., et al. (2013b). Digital rock physics benchmarks—part ii: Computing effective properties. *Computers & Geosciences*, 50:33–43.

Andrew, M., Bijeljic, B., and Blunt, M. J. (2014). Pore-scale imaging of trapped supercritical carbon dioxide in sandstones and carbonates. *International Journal of Greenhouse Gas Control*, 22:1–14.

Arand, F. and Hesser, J. (2017). Accurate and efficient maximal ball algorithm for pore network extraction. *Computers & Geosciences*, 101:28–37.

Arns, C. H., Knackstedt, M. A., Pinczewski, W. V., and Garboczi, E. J. (2002). Computation of linear elastic properties from microtomographic

images: Methodology and agreement between theory and experiment. *Geophysics*, 67(5):1396–1405.

Bakhshian, S., Shi, Z., Sahimi, M., Tsotsis, T., and Jessen, K. (2018). Image-based modeling of gas adsorption and swelling in high-pressure porous formations. *Sci. Rep*, 8:8249.

Balhoff, M. T., Thomas, S. G., and Wheeler, M. F. (2008). Mortar coupling and upscaling of pore-scale models. *Computational Geosciences*, 12(1):15–27.

Balhoff, M. T., Thompson, K. E., and Hjortsø, M. (2007). Coupling pore-scale networks to continuum-scale models of porous media. *Computers & Geosciences*, 33(3):393–410.

Blunt, M. J. (1998). Physically-based network modeling of multiphase flow in intermediate-wet porous media. *Journal of Petroleum Science and Engineering*, 20(3-4):117–125.

Blunt, M. J. (2001). Flow in porous media—pore-network models and multiphase flow. *Current opinion in colloid & interface science*, 6(3):197–207.

Blunt, M. J. (2017). *Multiphase flow in permeable media: A pore-scale perspective*. Cambridge University Press.

Blunt, M. J., Bijeljic, B., Dong, H., Gharbi, O., Iglauer, S., Mostaghimi, P., Paluszny, A., and Pentland, C. (2013). Pore-scale imaging and modelling. *Advances in Water resources*, 51:197–216.

Boek, E. S. and Venturoli, M. (2010). Lattice-boltzmann studies of fluid flow in porous media with realistic rock geometries. *Computers & Mathematics with Applications*, 59(7):2305–2314.

Bultreys, T., Singh, K., Raeini, A. Q., Ruspini, L. C., Øren, P.-E., Berg, S., Rücker, M., Bijeljic, B., and Blunt, M. J. (2020). Verifying pore network models of imbibition in rocks using time-resolved synchrotron imaging. *Water Resources Research*, 56(6):e2019WR026587.

Bultreys, T., Van Hoorebeke, L., and Cnudde, V. (2015). Multi-scale, micro-computed tomography-based pore network models to simulate drainage in heterogeneous rocks. *Advances in Water Resources*, 78:36–49.

Celia, M. A., Reeves, P. C., and Ferrand, L. A. (1995). Recent advances in pore scale models for multiphase flow in porous media. *Reviews of Geophysics*, 33(S2):1049–1057.

Chen, Y., Li, Y., Valocchi, A. J., and Christensen, K. T. (2018). Lattice boltzmann simulations of liquid co2 displacing water in a 2d heterogeneous micromodel at reservoir pressure conditions. *Journal of contaminant hydrology*, 212:14–27.

Chu, J., Engquist, B., Prodanović, M., and Tsai, R. (2013). A multiscale method coupling network and continuum models in porous media ii—single-and two-phase flows. In *Advances in Applied Mathematics, Modeling, and Computational Science*, pages 161–185. Springer.

Da Wang, Y., Chung, T., Armstrong, R. T., McClure, J. E., and Mostaghimi, P. (2019). Computations of permeability of large rock images by dual grid domain decomposition. *Advances in water resources*, 126:1–14.

Dalton, L. E., Klise, K. A., Fuchs, S., Crandall, D., and Goodman, A. (2018). Methods to measure contact angles in scco2-brine-sandstone systems. *Advances in water resources*, 122:278–290.

d'Humieres, D. (2002). Multiple–relaxation–time lattice boltzmann models in three dimensions. *Philosophical Transactions of the Royal Society of London. Series A: Mathematical, Physical and Engineering Sciences*, 360(1792):437–451.

Dong, H. (2008). *Micro-CT imaging and pore network extraction*. PhD thesis, Department of Earth Science and Engineering, Imperial College London.

Dong, H. and Blunt, M. J. (2009). Pore-network extraction from micro-computerized-tomography images. *Physical review E*, 80(3):036307.

Dunsmuir, J. H., Ferguson, S., D'Amico, K., Stokes, J., et al. (1991). X-ray microtomography: a new tool for the characterization of porous media. In *SPE annual technical conference and exhibition*. Society of Petroleum Engineers.

Fatt, I. et al. (1956). The network model of porous media. *Transactions of the AIME*, 207(01):144–181.

Fenwick, D. H. and Blunt, M. J. (1998). Three-dimensional modeling of three phase imbibition and drainage. *Advances in water resources*, 21(2):121–143.

Ferrari, A. and Lunati, I. (2013). Direct numerical simulations of interface dynamics to link capillary pressure and total surface energy. *Advances in water resources*, 57:19–31.

Ferreol, B. and Rothman, D. H. (1995). Lattice-boltzmann simulations of flow through fontainebleau sandstone. In *Multiphase flow in porous media*, pages 3–20. Springer.

Finley, R. J. (2014). An overview of the illinois basin–decatur project. *Greenhouse Gases: Science and Technology*, 4(5):571–579.

Flannery, B. P., Deckman, H. W., Roberge, W. G., and D'AMICO, K. L. (1987). Three-dimensional x-ray microtomography. *Science*, 237(4821):1439–1444.

Francois, M. M., Cummins, S. J., Dendy, E. D., Kothe, D. B., Sicilian, J. M., and Williams, M. W. (2006). A balanced-force algorithm for continuous and sharp interfacial surface tension models within a volume tracking framework. *Journal of Computational Physics*, 213(1):141–173.

Friedlingstein, P. and Solomon, S. (2005). Contributions of past and present human generations to committed warming caused by carbon dioxide. *Proceedings of the National Academy of Sciences*, 102(31):10832–10836.

Gershenzon, N. I., Ritzi Jr, R. W., Dominic, D. F., Mehnert, E., and Okwen, R. T. (2017). Capillary trapping of co2 in heterogeneous reservoirs during the injection period. *International Journal of greenhouse gas control*, 59:13–23.

Gostick, J. T. (2017). Versatile and efficient pore network extraction method using marker-based watershed segmentation. *Physical Review E*, 96(2):023307.

Grunau, D., Chen, S., and Eggert, K. (1993). A lattice boltzmann model for multiphase fluid flows. *Physics of Fluids A: Fluid Dynamics*, 5(10):2557–2562.

Gueyffier, D., Li, J., Nadim, A., Scardovelli, R., and Zaleski, S. (1999). Volume-of-fluid interface tracking with smoothed surface stress methods for three-dimensional flows. *Journal of Computational physics*, 152(2):423–456.

Gunstensen, A. K., Rothman, D. H., Zaleski, S., and Zanetti, G. (1991). Lattice boltzmann model of immiscible fluids. *Physical Review A*, 43(8):4320.

Harrigan, T. and Mann, R. (1984). Characterization of microstructural anisotropy in orthotropic materials using a second rank tensor. *Journal of Materials Science*, 19(3):761–767.

Hefny, M., Qin, C., Saar, M. O., and Ebigbo, A. (2020). Synchrotron-based pore-network modeling of two-phase flow in nubian sandstone and implications for capillary trapping of carbon dioxide. *arXiv preprint arXiv:2004.06792*.

Herring, A. L., Andersson, L., and Wildenschild, D. (2016). Enhancing residual trapping of supercritical co2 via cyclic injections. *Geophysical Research Letters*, 43(18):9677–9685.

Honarpour, M. M., Koederitz, F., and Herbert, A. (1986). *Relative permeability of petroleum reservoirs*. CRC press.

Huang, H., Meakin, P., and Liu, M. (2005). Computer simulation of two-phase immiscible fluid motion in unsaturated complex fractures using a volume of fluid method. *Water resources research*, 41(12).

Huang, H., Sukop, M., and Lu, X. (2015). *Multiphase lattice Boltzmann methods: Theory and application*. John Wiley & Sons.

Hughes, R. G. and Blunt, M. J. (2000). Pore scale modeling of rate effects in imbibition. *Transport in Porous Media*, 40(3):295–322.

Idowu, N. A. and Blunt, M. J. (2010). Pore-scale modelling of rate effects in waterflooding. *Transport in porous media*, 83(1):151–169.

Jackson, S. J., Lin, Q., and Krevor, S. (2019). Representative elementary volumes, hysteresis and heterogeneity in multiphase flow from the pore to continuum scale. *Water Resources Research*, page e2019WR026396.

Jiang, F. and Tsuji, T. (2014). Changes in pore geometry and relative permeability caused by carbonate precipitation in porous media. *Physical Review E*, 90(5):053306.

Jiang, F. and Tsuji, T. (2015). Impact of interfacial tension on residual co2 clusters in porous sandstone. *Water Resources Research*, 51(3):1710–1722.

Jiang, F. and Tsuji, T. (2017). Estimation of three-phase relative permeability by simulating fluid dynamics directly on rock-microstructure images. *Water Resources Research*, 53(1):11–32.

Jiang, Z., Van Dijke, M., Sorbie, K. S., and Couples, G. D. (2013). Representation of multiscale heterogeneity via multiscale pore networks. *Water resources research*, 49(9):5437–5449.

Joekar-Niasar, V. and Hassanizadeh, S. (2012). Analysis of fundamentals of two-phase flow in porous media using dynamic pore-network models: A review. *Critical reviews in environmental science and technology*, 42(18):1895–1976.

Juanes, R., Spiteri, E., Orr Jr, F., and Blunt, M. (2006). Impact of relative permeability hysteresis on geological co2 storage. *Water resources research*, 42(12).

Karimpouli, S. and Tahmasebi, P. (2019). Segmentation of digital rock images using deep convolutional autoencoder networks. *Computers & geosciences*, 126:142–150.

Knackstedt, M. A., Sahimi, M., and Sheppard, A. P. (2000). Invasion percolation with long-range correlations: first-order phase transition and nonuniversal scaling properties. *Physical Review E*, 61(5):4920.

Kohanpur, A., Chen, Y., Valocchi, A., Tudek, J., and Crandall, D. (2016). Comparison of pore-network and lattice boltzmann models for pore-scale modeling of geological storage of co2 in natural reservoir rocks. *AGUFM*, 2016:H51B–1466.

Kohanpur, A. H., Rahromostaqim, M., Valocchi, A. J., and Sahimi, M. (2020). Two-phase flow of co2-brine in a heterogeneous sandstone: Characterization of the rock and comparison of the lattice-boltzmann, pore-network, and direct numerical simulation methods. *Advances in Water Resources*, 135:103469.

Kohanpur, A. H., Valocchi, A., and Crandall, D. (2019). Micro-ct images of a heterogeneous mt. simon sandstone sample. `http://www.digitalrocksportal.org/projects/247`.

Kohanpur, A. H. and Valocchi, A. J. (2018). Pore network stitching for pore-to-core upscaling of two-phase flow in heterogeneous rocks. *AGUFM*, 2018:H44F–07.

Kohanpur, A. H. and Valocchi, A. J. (2019). Stochastic pore network stitching for pore-to-core upscaling of two-phase flow in heterogeneous rocks. *AGUFM*, 2019:H13R–2024.

Kohanpur, A. H. and Valocchi, A. J. (2020a). Pore-network stitching method: A pore-to-core upscaling approach for multiphase flow. *Transport in porous media*, 135(3):659–685.

Kohanpur, A. H. and Valocchi, A. J. (2020b). Pore-network stitching method: A pore-to-core upscaling approach for multiphase flow. *arXiv preprint arXiv:2004.01523*.

Krevor, S. C., Pini, R., Zuo, L., and Benson, S. M. (2012). Relative permeability and trapping of co2 and water in sandstone rocks at reservoir conditions. *Water resources research*, 48(2).

Lallemand, P. and Luo, L.-S. (2000). Theory of the lattice boltzmann method: Dispersion, dissipation, isotropy, galilean invariance, and stability. *Physical Review E*, 61(6):6546.

Land, C. S. et al. (1968). Calculation of imbibition relative permeability for two-and three-phase flow from rock properties. *Society of Petroleum Engineers Journal*, 8(02):149–156.

Lenormand, R., Zarcone, C., and Sarr, A. (1983). Mechanisms of the displacement of one fluid by another in a network of capillary ducts. *Journal of Fluid Mechanics*, 135:337–353.

Levine, J. S., Goldberg, D. S., Lackner, K. S., Matter, J. M., Supp, M. G., and Ramakrishnan, T. (2014). Relative permeability experiments of carbon dioxide displacing brine and their implications for carbon sequestration. *Environmental science & technology*, 48(1):811–818.

Lindquist, W. B., Lee, S.-M., Coker, D. A., Jones, K. W., and Spanne, P. (1996). Medial axis analysis of void structure in three-dimensional tomographic images of porous media. *Journal of Geophysical Research: Solid Earth*, 101(B4):8297–8310.

Liu, H., Kang, Q., Leonardi, C. R., Schmieschek, S., Narváez, A., Jones, B. D., Williams, J. R., Valocchi, A. J., and Harting, J. (2016). Multiphase lattice boltzmann simulations for porous media applications. *Computational Geosciences*, 20(4):777–805.

Long, H., Nardi, C., Idowu, N., Carnerup, A., Øren, P., Knackstedt, M., and Lithicon, A. (2013). Multi-scale imaging and modeling workflow to capture and characterize microporosity in sandstone. In *International Symposium of the Society of Core Analysts, Napa Valley, California, USA*, volume 13.

Mahabadi, N., van Paassen, L., Battiato, I., Yun, T. S., Choo, H., and Jang, J. (2020). Impact of pore-scale characteristics on immiscible fluid displacement. *Geofluids*, 2020.

Mehmani, Y. and Balhoff, M. T. (2014). Bridging from pore to continuum: A hybrid mortar domain decomposition framework for subsurface flow and transport. *Multiscale Modeling & Simulation*, 12(2):667–693.

Metz, B., Davidson, O., De Coninck, H., et al. (2005). *Carbon dioxide capture and storage: special report of the intergovernmental panel on climate change*. Cambridge University Press.

Miao, X., Gerke, K. M., and Sizonenko, T. O. (2017). A new way to parameterize hydraulic conductances of pore elements: A step towards creating pore-networks without pore shape simplifications. *Advances in water resources*, 105:162–172.

Mohaghegh, S. (2018). *Data-Driven Analytics for the Geological Storage of CO2*. CRC Press.

Morrow, N. R. et al. (1975). The effects of surface roughness on contact: angle with special reference to petroleum recovery. *Journal of Canadian Petroleum Technology*, 14(04).

Münch, B. and Holzer, L. (2008). Contradicting geometrical concepts in pore size analysis attained with electron microscopy and mercury intrusion. *Journal of the American Ceramic Society*, 91(12):4059–4067.

Nordbotten, J. M. and Celia, M. A. (2011). *Geological storage of CO2: modeling approaches for large-scale simulation*. John Wiley & Sons.

Oak, M., Baker, L., Thomas, D., et al. (1990). Three-phase relative permeability of berea sandstone. *Journal of Petroleum Technology*, 42(08):1–054.

Odgaard, A. (1997). Three-dimensional methods for quantification of cancellous bone architecture. *Bone*, 20(4):315–328.

Odgaard, A. and Gundersen, H. (1993). Quantification of connectivity in cancellous bone, with special emphasis on 3-d reconstructions. *Bone*, 14(2):173–182.

Øren, P.-E. and Bakke, S. (2002). Process based reconstruction of sandstones and prediction of transport properties. *Transport in porous media*, 46(2-3):311–343.

Pak, T., Butler, I. B., Geiger, S., van Dijke, M. I., Jiang, Z., and Surmas, R. (2016). Multiscale pore-network representation of heterogeneous carbonate rocks. *Water Resources Research*, 52(7):5433–5441.

Pan, C., Hilpert, M., and Miller, C. (2004). Lattice-boltzmann simulation of two-phase flow in porous media. *Water Resources Research*, 40(1).

Patzek, T. W. and Kristensen, J. (2001). Shape factor correlations of hydraulic conductance in noncircular capillaries: Ii. two-phase creeping flow. *Journal of colloid and interface science*, 236(2):305–317.

Patzek, T. W. and Silin, D. B. (2000). Shape factor and hydraulic conductance in noncircular capillaries. i. one-phase creeping flow. *Journal of colloid and interface science*, 236(2).

Perrin, J.-C. and Benson, S. (2010). An experimental study on the influence of sub-core scale heterogeneities on co 2 distribution in reservoir rocks. *Transport in porous media*, 82(1):93–109.

Porter, M. L., Schaap, M. G., and Wildenschild, D. (2009). Lattice-boltzmann simulations of the capillary pressure–saturation–interfacial area relationship for porous media. *Advances in Water Resources*, 32(11):1632–1640.

Prodanović, M. and Bryant, S. L. (2006). A level set method for determining critical curvatures for drainage and imbibition. *Journal of colloid and interface science*, 304(2):442–458.

Pruess, K. and Garcia, J. (2002). Multiphase flow dynamics during co 2 disposal into saline aquifers. *Environmental Geology*, 42(2-3):282–295.

Qi, R., LaForce, T. C., and Blunt, M. J. (2009). Design of carbon dioxide storage in aquifers. *International Journal of Greenhouse Gas Control*, 3(2):195–205.

Rabbani, A., Mostaghimi, P., and Armstrong, R. T. (2019). Pore network extraction using geometrical domain decomposition. *Advances in water resources*, 123:70–83.

Rabbani, H. S., Joekar-Niasar, V., Pak, T., and Shokri, N. (2017). New insights on the complex dynamics of two-phase flow in porous media under intermediate-wet conditions. *Scientific reports*, 7(1):1–7.

Raeini, A. Q. (2013). *Modelling multiphase flow through micro-CT images of the pore space*. PhD thesis, Imperial College London.

Raeini, A. Q., Bijeljic, B., and Blunt, M. J. (2017). Generalized network modeling: Network extraction as a coarse-scale discretization of the void space of porous media. *Physical Review E*, 96(1):013312.

Raeini, A. Q., Bijeljic, B., and Blunt, M. J. (2018). Generalized network modeling of capillary-dominated two-phase flow. *Physical Review E*, 97(2):023308.

Raeini, A. Q., Blunt, M. J., and Bijeljic, B. (2012). Modelling two-phase flow in porous media at the pore scale using the volume-of-fluid method. *Journal of Computational Physics*, 231(17):5653–5668.

Raeini, A. Q., Blunt, M. J., and Bijeljic, B. (2014). Direct simulations of two-phase flow on micro-ct images of porous media and upscaling of pore-scale forces. *Advances in water resources*, 74:116–126.

Rahromostaqim, M. and Sahimi, M. (2018). Molecular dynamics simulation of hydration and swelling of mixed-layer clays. *The Journal of Physical Chemistry C*, 122(26):14631–14639.

Rahromostaqim, M. and Sahimi, M. (2019). Molecular dynamics simulation of hydration and swelling of mixed-layer clays in the presence of carbon dioxide. *The Journal of Physical Chemistry C*, 123(7):4243–4255.

Ramstad, T., Berg, C. F., and Thompson, K. (2019). Pore-scale simulations of single-and two-phase flow in porous media: approaches and applications. *Transport in Porous Media*, 130(1):77–104.

Ramstad, T., Idowu, N., Nardi, C., and Øren, P.-E. (2012). Relative permeability calculations from two-phase flow simulations directly on digital images of porous rocks. *Transport in Porous Media*, 94(2):487–504.

Ramstad, T., Øren, P.-E., Bakke, S., et al. (2010). Simulation of two-phase flow in reservoir rocks using a lattice boltzmann method. *Spe Journal*, 15(04):917–927.

Raoof, A. and Hassanizadeh, S. M. (2010). A new method for generating pore-network models of porous media. *Transport in porous media*, 81(3):391–407.

Raoof, A., Nick, H., Hassanizadeh, S. M., and Spiers, C. (2013). Poreflow: A complex pore-network model for simulation of reactive transport in variably saturated porous media. *Computers & Geosciences*, 61:160–174.

Rasmusson, K., Rasmusson, M., Tsang, Y., Benson, S., Hingerl, F., Fagerlund, F., and Niemi, A. (2018). Residual trapping of carbon dioxide during geological storage—insight gained through a pore-network modeling approach. *International Journal of Greenhouse Gas Control*, 74:62–78.

Rothman, D. H. (1990). Macroscopic laws for immiscible two-phase flow in porous media: Results from numerical experiments. *Journal of Geophysical Research: Solid Earth*, 95(B6):8663–8674.

Ruspini, L., Farokhpoor, R., and Øren, P. (2017). Pore-scale modeling of capillary trapping in water-wet porous media: A new cooperative pore-body filling model. *Advances in Water Resources*, 108:1–14.

Sahimi, M. (2011). *Flow and transport in porous media and fractured rock: from classical methods to modern approaches*. John Wiley & Sons.

Schindelin, J., Arganda-Carreras, I., Frise, E., Kaynig, V., Longair, M., Pietzsch, T., Preibisch, S., Rueden, C., Saalfeld, S., Schmid, B., et al. (2012). Fiji: an open-source platform for biological-image analysis. *Nature methods*, 9(7):676–682.

Shams, M., Raeini, A. Q., Blunt, M. J., and Bijeljic, B. (2018). A study to investigate viscous coupling effects on the hydraulic conductance of fluid layers in two-phase flow at the pore level. *Journal of colloid and interface science*, 522:299–310.

Sheppard, A. P., Knackstedt, M. A., Pinczewski, W. V., and Sahimi, M. (1999). Invasion percolation: new algorithms and universality classes. *Journal of Physics A: Mathematical and General*, 32(49):L521.

Shukla, R., Ranjith, P., Haque, A., and Choi, X. (2010). A review of studies on co2 sequestration and caprock integrity. *Fuel*, 89(10):2651–2664.

Silin, D. and Patzek, T. (2006). Pore space morphology analysis using maximal inscribed spheres. *Physica A: Statistical mechanics and its applications*, 371(2):336–360.

Sochi, T. (2007). *Pore-Scale Modeling of Non-Newtonian Flow in Porous Media*. PhD thesis, Department of Earth Science and Engineering, Imperial College London.

Suh, H. S., Kang, D. H., Jang, J., Kim, K. Y., and Yun, T. S. (2017). Capillary pressure at irregularly shaped pore throats: Implications for water retention characteristics. *Advances in Water Resources*, 110:51–58.

Sukop, M. (2006). *DT Thorne, Jr. Lattice Boltzmann Modeling Lattice Boltzmann Modeling*. Springer.

Sun, T., Mehmani, Y., Bhagmane, J., and Balhoff, M. T. (2012). Pore to continuum upscaling of permeability in heterogeneous porous media using mortars. *International Journal of Oil, Gas and Coal Technology*, 5(2-3):249–266.

Tahmasebi, P. and Kamrava, S. (2018). Rapid multiscale modeling of flow in porous media. *Physical Review E*, 98(5):052901.

Tahmasebi, P., Kamrava, S., Bai, T., and Sahimi, M. (2020). Machine learning in geo-and environmental sciences: From small to large scale. *Advances in Water Resources*, page 103619.

Tahmasebi, P. and Sahimi, M. (2012). Reconstruction of three-dimensional porous media using a single thin section. *Physical Review E*, 85(6):066709.

Tahmasebi, P., Sahimi, M., Kohanpur, A. H., and Valocchi, A. (2017). Pore-scale simulation of flow of co2 and brine in reconstructed and actual 3d rock cores. *Journal of Petroleum Science and Engineering*, 155:21–33.

Tang, Y., Min, J., Zhang, X., and Liu, G. (2018). Meniscus behaviors and capillary pressures in capillary channels having various cross-sectional geometries. *Chinese Journal of Chemical Engineering*, 26(10):2014–2022.

Tölke, J. (2002). Lattice boltzmann simulations of binary fluid flow through porous media. *Philosophical Transactions of the Royal Society of London. Series A: Mathematical, Physical and Engineering Sciences*, 360(1792):535–545.

Tölke, J., Freudiger, S., and Krafczyk, M. (2006). An adaptive scheme using hierarchical grids for lattice boltzmann multi-phase flow simulations. *Computers & fluids*, 35(8-9):820–830.

Toriwaki, J. and Yonekura, T. (2002). Euler number and connectivity indexes of a three dimensional digital picture. *FORMA-TOKYO-*, 17(3):183–209.

Ubbink, O. (1997). *Numerical prediction of two fluid systems with sharp interfaces*. PhD thesis, Imperial College London.

Valvatne, P. H. (2003). Predictive pore-scale modelling of multiphase flow. *PhD Disseration. Imperial College*.

Valvatne, P. H. (2004). *Predictive pore-scale modelling of multiphase flow*. PhD thesis, Department of Earth Science and Engineering, Imperial College London London.

Valvatne, P. H. and Blunt, M. J. (2004). Predictive pore-scale modeling of two-phase flow in mixed wet media. *Water resources research*, 40(7).

Varloteaux, C., Békri, S., and Adler, P. M. (2013). Pore network modelling to determine the transport properties in presence of a reactive fluid: From pore to reservoir scale. *Advances in Water Resources*, 53:87–100.

Wildenschild, D. and Sheppard, A. P. (2013). X-ray imaging and analysis techniques for quantifying pore-scale structure and processes in subsurface porous medium systems. *Advances in Water Resources*, 51:217–246.

Wilkinson, D. and Willemsen, J. F. (1983). Invasion percolation: a new form of percolation theory. *Journal of Physics A: Mathematical and General*, 16(14):3365.

Xie, C., Raeini, A. Q., Wang, Y., Blunt, M. J., and Wang, M. (2017). An improved pore-network model including viscous coupling effects using direct simulation by the lattice boltzmann method. *Advances in water resources*, 100:26–34.

Zahasky, C., Jackson, S. J., Lin, Q., and Krevor, S. (2019). Pore network model predictions of darcy-scale multiphase flow heterogeneity validated by experiments. *Water Resources Research*, page e2019WR026708.

Zhao, B., MacMinn, C. W., Primkulov, B. K., Chen, Y., Valocchi, A. J., Zhao, J., Kang, Q., Bruning, K., McClure, J. E., Miller, C. T., et al. (2019). Comprehensive comparison of pore-scale models for multiphase flow in porous media. *Proceedings of the National Academy of Sciences*, 116(28):13799–13806.

Zhao, J., Qin, F., Derome, D., and Carmeliet, J. (2020). Simulation of quasi-static drainage displacement in porous media on pore-scale: Coupling lattice boltzmann method and pore network model. *Journal of Hydrology*, page 125080.

Appendix A

Validation

Validation of the pore-network stitching method on more rock samples

In this appendix, more validation results of the developed PNSM, introduced in Chapter 3 , are presented. Two-phase flow pore-network simulation on the introduced samples in Chapter 3 are carried out. The samples are Berea sandstone (BR), Bentheimer sandstone (BN), Mt. Simon sandstone (ML), C1 carbonate (C1), C2 carbonate (C2). Basic information of their 3D images and properties are reported in Chapter 3.

For each sample, the 3D reconstructed geometry of the rock and the segmented image of one slice of the stack are presented. Then, drainage relative permeability curves of CO_2 and brine together for longitudinal and lateral layered stitching studies are reported, respectively. Finally, validation of volumetric stitching are presented where relative permeability curves of 10 realizations and their mean are reported for CO_2 and brine phases, respectively. In all cases, the reference pore-network is obtained as discussed in Chapter 3.

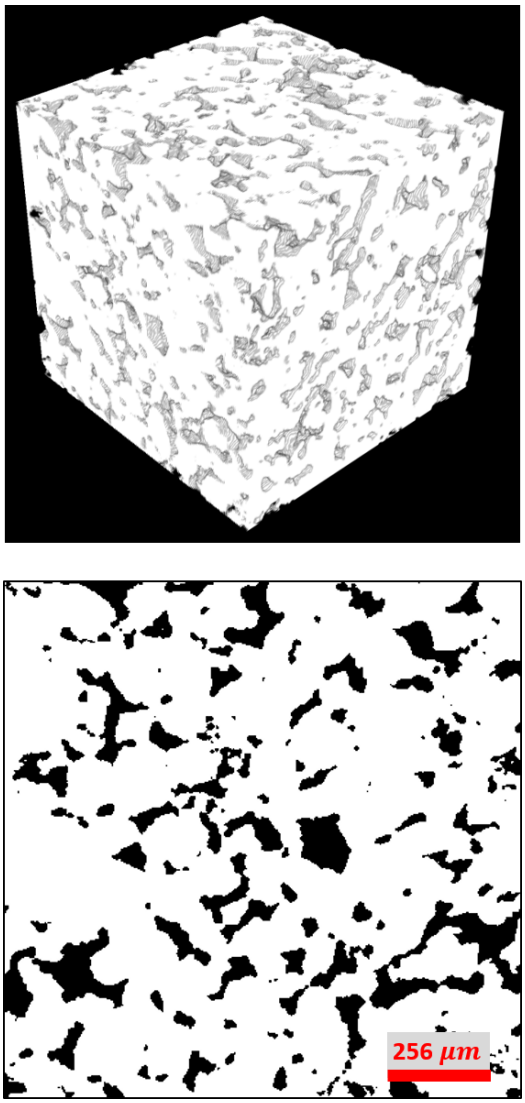

Figure A.1: The sample **BR**: (top) the 3D reconstructed geometry of the rock and (bottom) the segmented image of one slice of the stack.

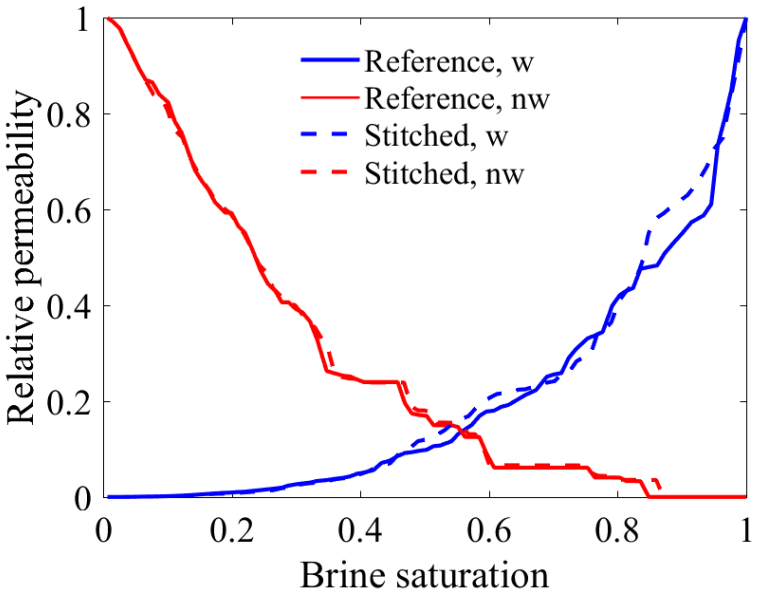

Figure A.2: Comparison of relative permeability curves of the stitched pore-network from sample **BR** via longitudinal layered stitching with its reference pore-network.

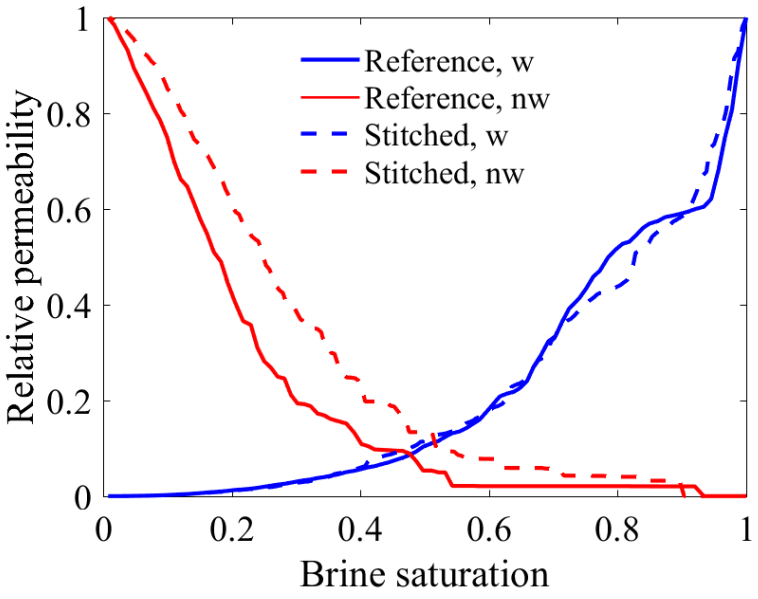

Figure A.3: Comparison of relative permeability curves of the stitched pore-network from sample **BR** via lateral layered stitching with its reference pore-network.

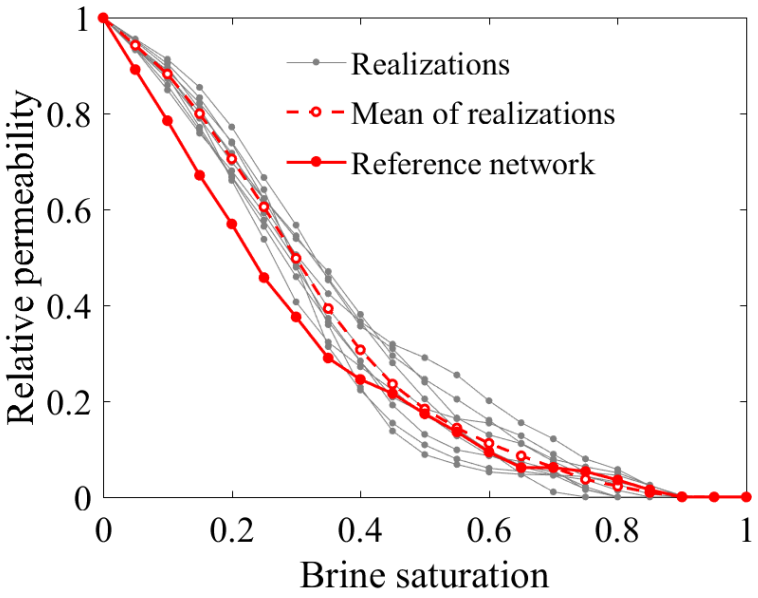

Figure A.4: Comparison of CO_2 relative permeability of 10 realizations of stitched pore-networks from sample **BR** via volumetric stitching with their reference pore-network.

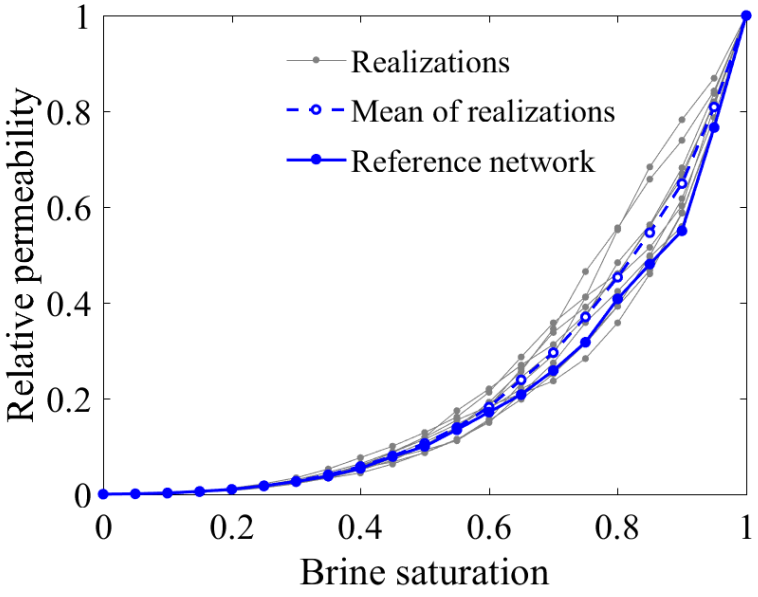

Figure A.5: Comparison of brine relative permeability of 10 realizations of stitched pore-networks from sample **BR** via volumetric stitching with their reference pore-network.

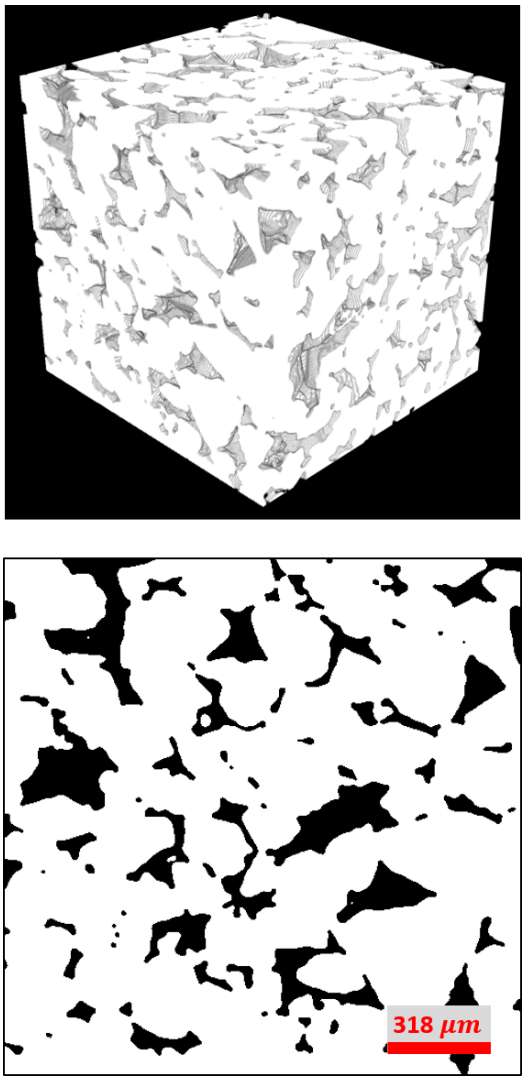

Figure A.6: The sample **BN**: (top) the 3D reconstructed geometry of the rock and (bottom) the segmented image of one slice of the stack.

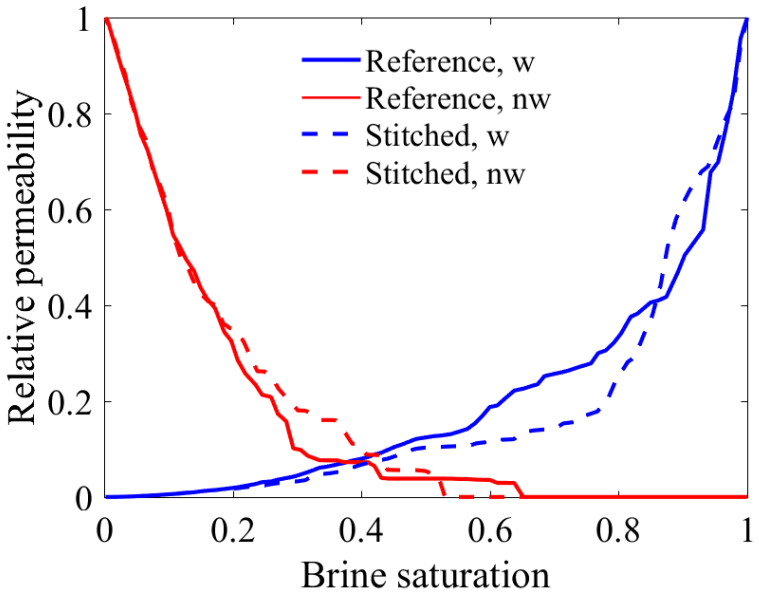

Figure A.7: Comparison of relative permeability curves of the stitched pore-network from sample **BN** via longitudinal layered stitching with its reference pore-network.

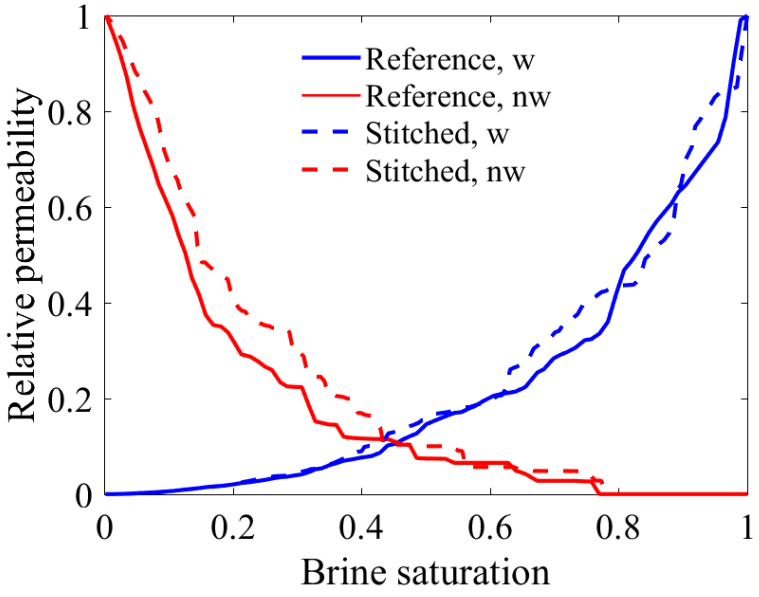

Figure A.8: Comparison of relative permeability curves of the stitched pore-network from sample **BN** via lateral layered stitching with its reference pore-network.

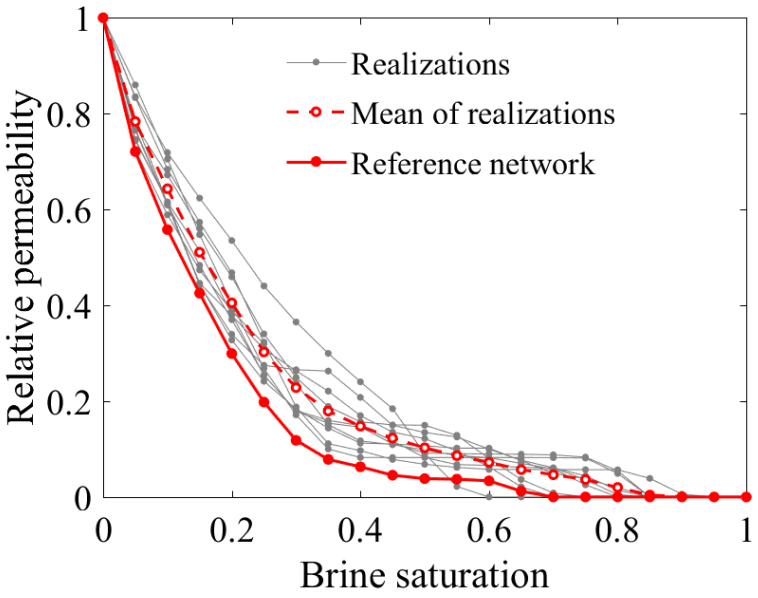

Figure A.9: Comparison of CO_2 relative permeability of 10 realizations of stitched pore-networks from sample **BN** via volumetric stitching with their reference pore-network.

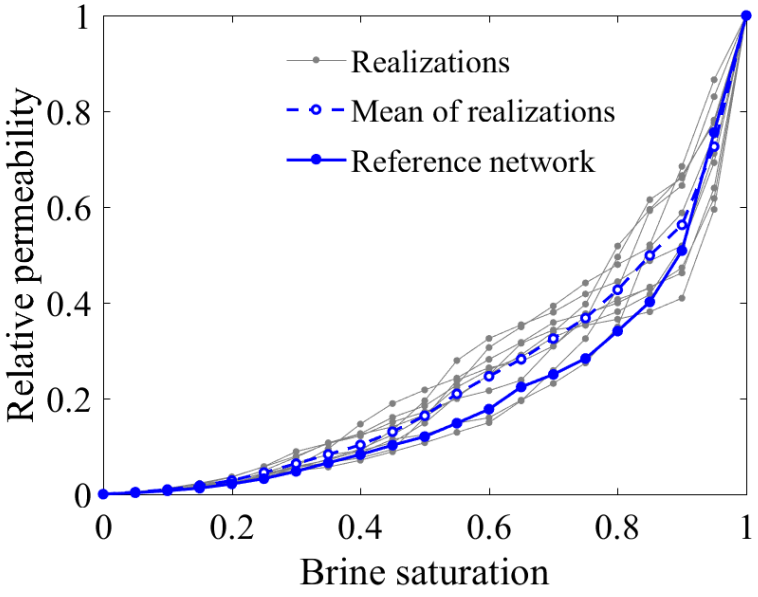

Figure A.10: Comparison of brine relative permeability of 10 realizations of stitched pore-networks from sample **BN** via volumetric stitching with their reference pore-network.

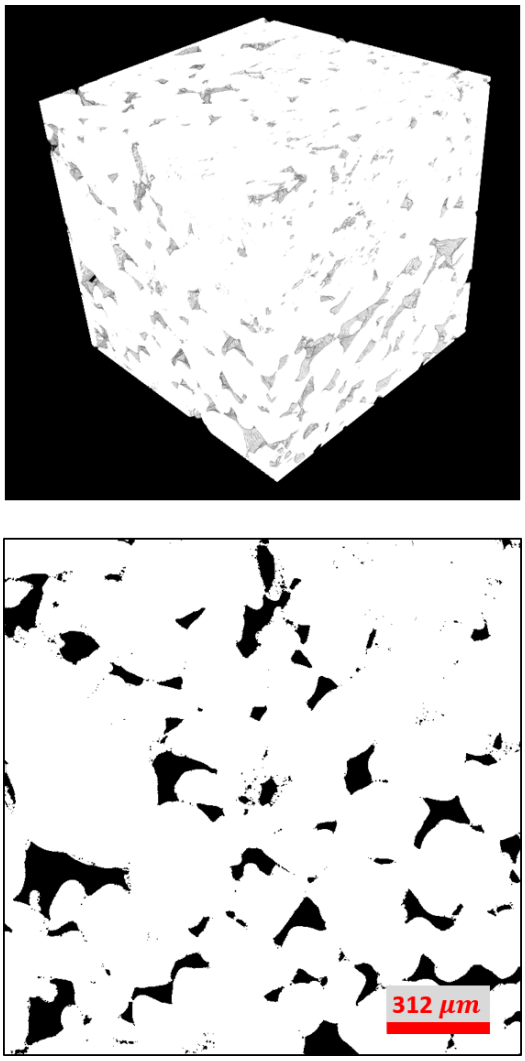

Figure A.11: The sample **ML**: (top) the 3D reconstructed geometry of the rock and (bottom) the segmented image of one slice of the stack.

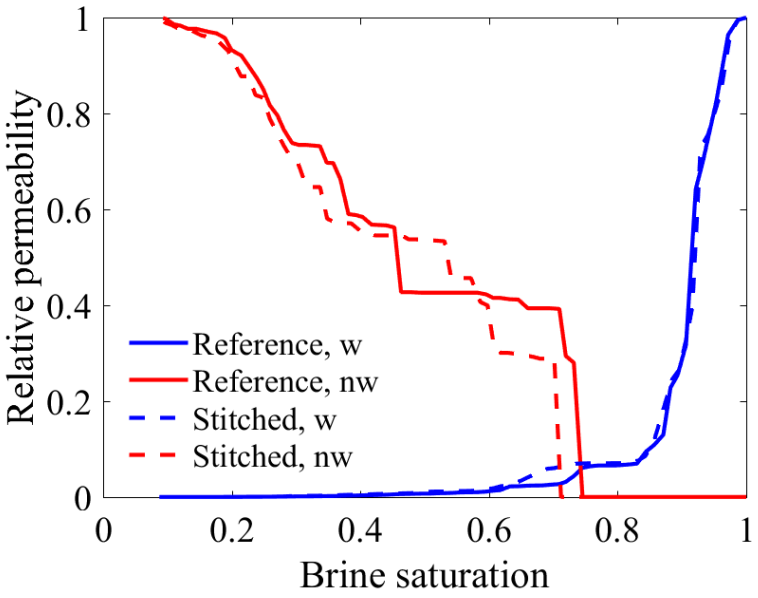

Figure A.12: Comparison of relative permeability curves of the stitched pore-network from sample **ML** via longitudinal layered stitching with its reference pore-network.

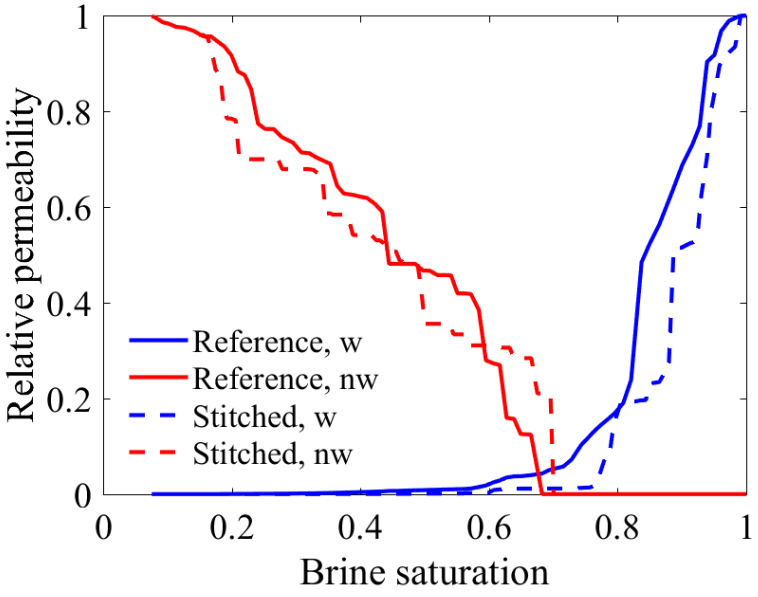

Figure A.13: Comparison of relative permeability curves of the stitched pore-network from sample **ML** via lateral layered stitching with its reference pore-network.

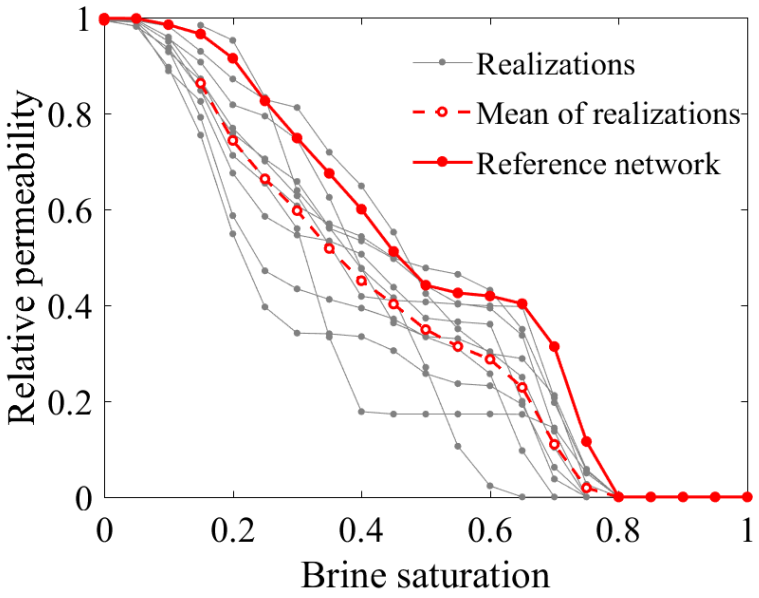

Figure A.14: Comparison of CO_2 relative permeability of 10 realizations of stitched pore-networks from sample **ML** via volumetric stitching with their reference pore-network.

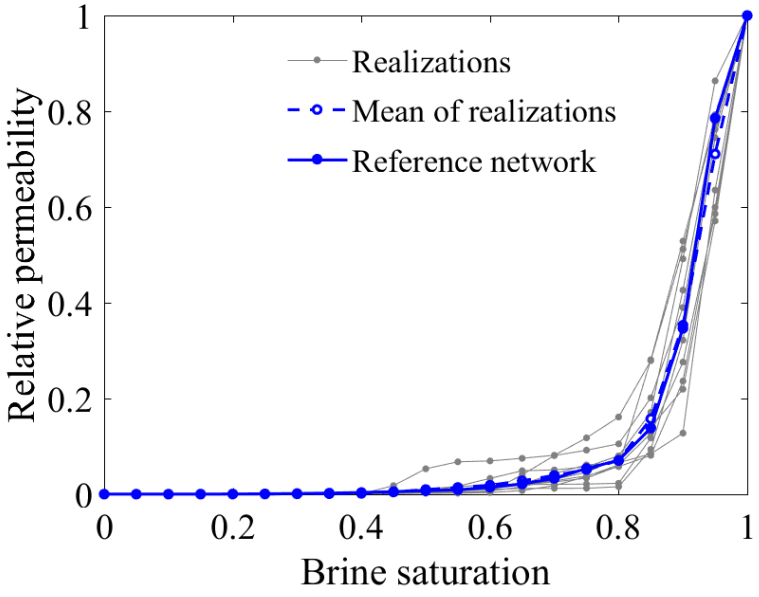

Figure A.15: Comparison of brine relative permeability of 10 realizations of stitched pore-networks from sample **ML** via volumetric stitching with their reference pore-network.

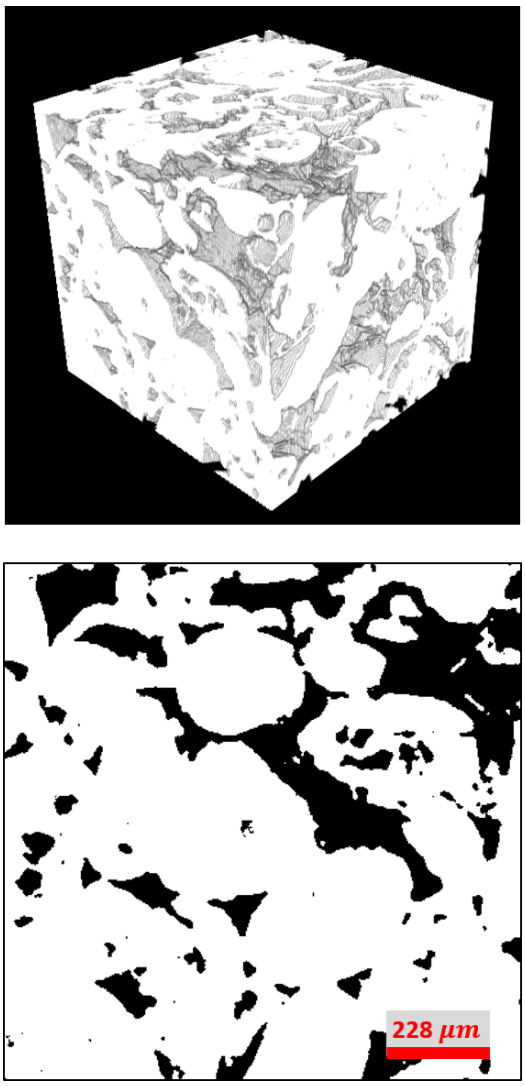

Figure A.16: The sample **C1**: (top) the 3D reconstructed geometry of the rock and (bottom) the segmented image of one slice of the stack.

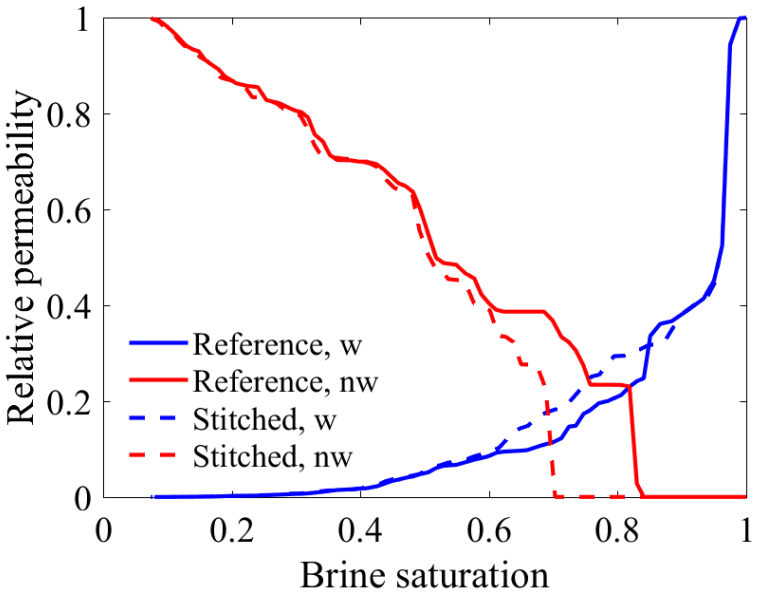

Figure A.17: Comparison of relative permeability curves of the stitched pore-network from sample **C1** via longitudinal layered stitching with its reference pore-network.

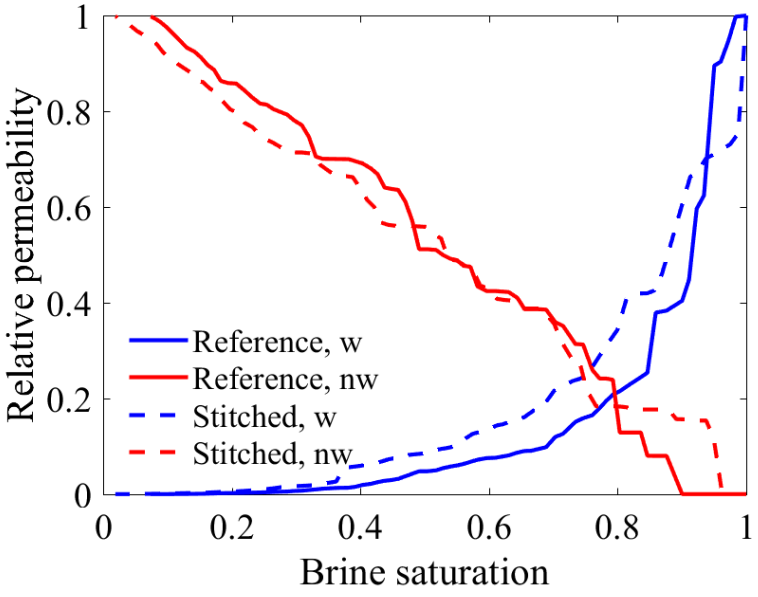

Figure A.18: Comparison of relative permeability curves of the stitched pore-network from sample **C1** via lateral layered stitching with its reference pore-network.

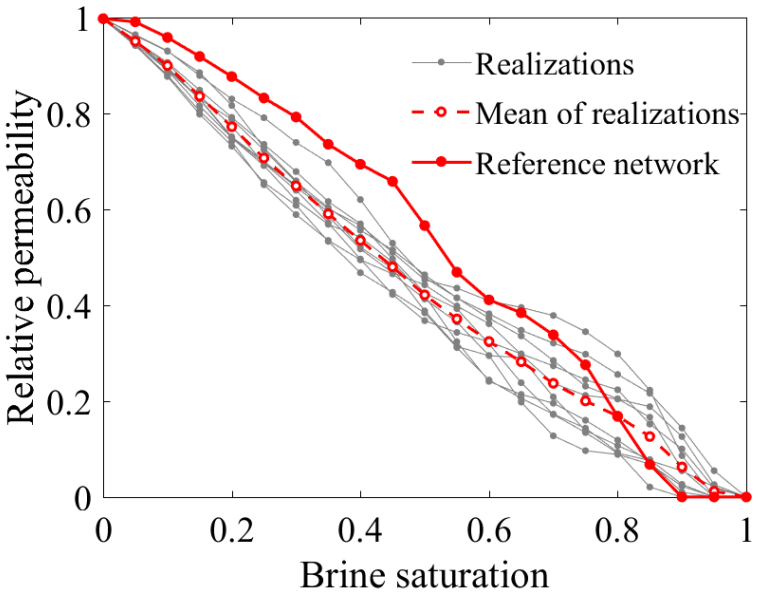

Figure A.19: Comparison of CO_2 relative permeability of 10 realizations of stitched pore-networks from sample **C1** via volumetric stitching with their reference pore-network.

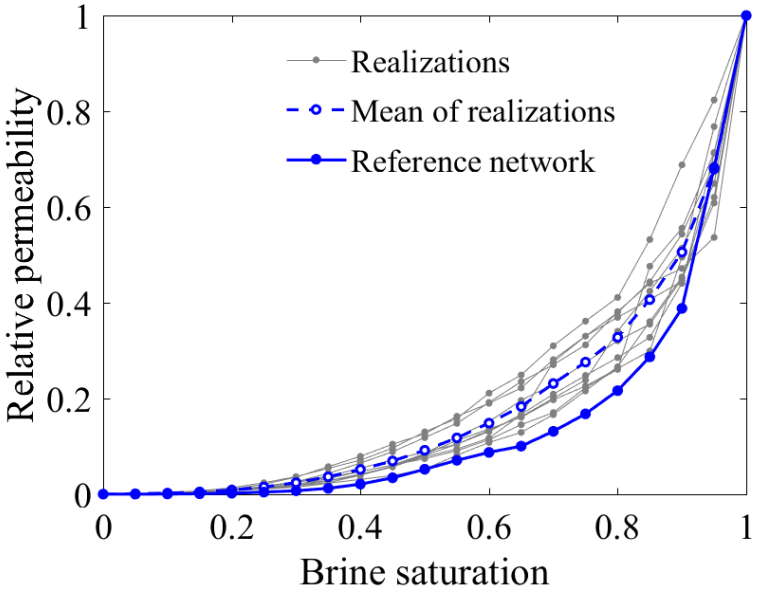

Figure A.20: Comparison of brine relative permeability of 10 realizations of stitched pore-networks from sample **C1** via volumetric stitching with their reference pore-network.

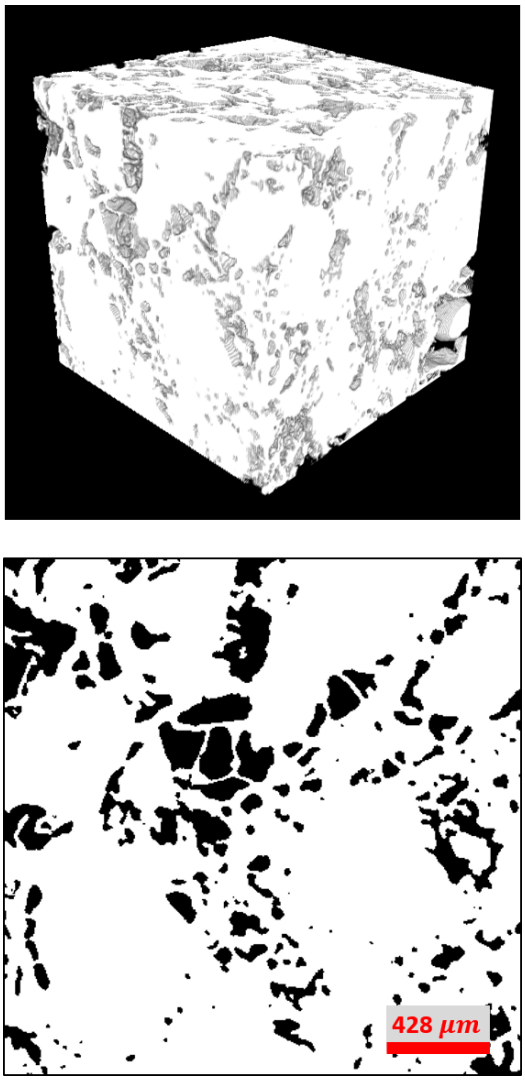

Figure A.21: The sample **C2**: (top) the 3D reconstructed geometry of the rock and (bottom) the segmented image of one slice of the stack.

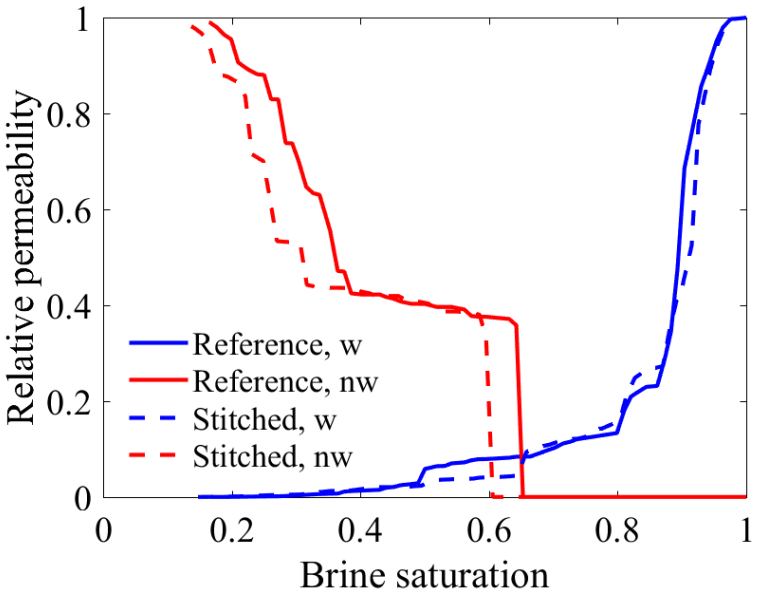

Figure A.22: Comparison of relative permeability curves of the stitched pore-network from sample **C2** via longitudinal layered stitching with its reference pore-network.

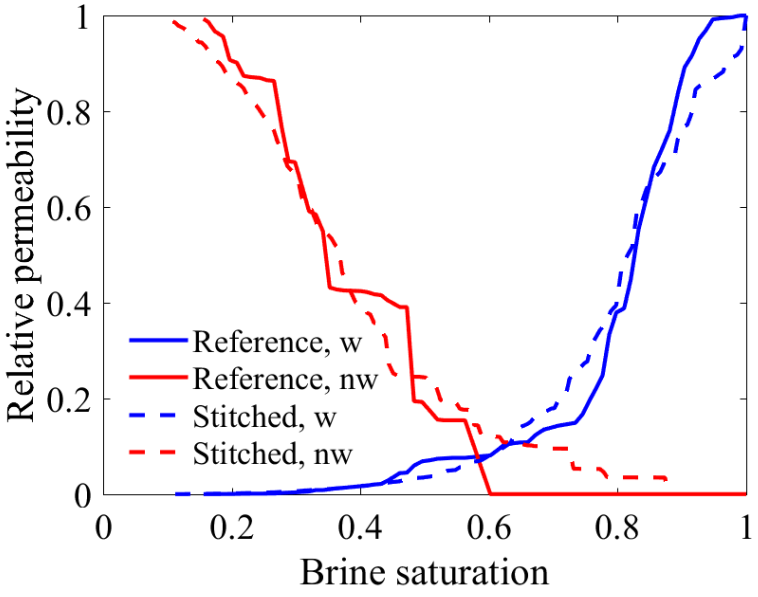

Figure A.23: Comparison of relative permeability curves of the stitched pore-network from sample **C2** via lateral layered stitching with its reference pore-network.

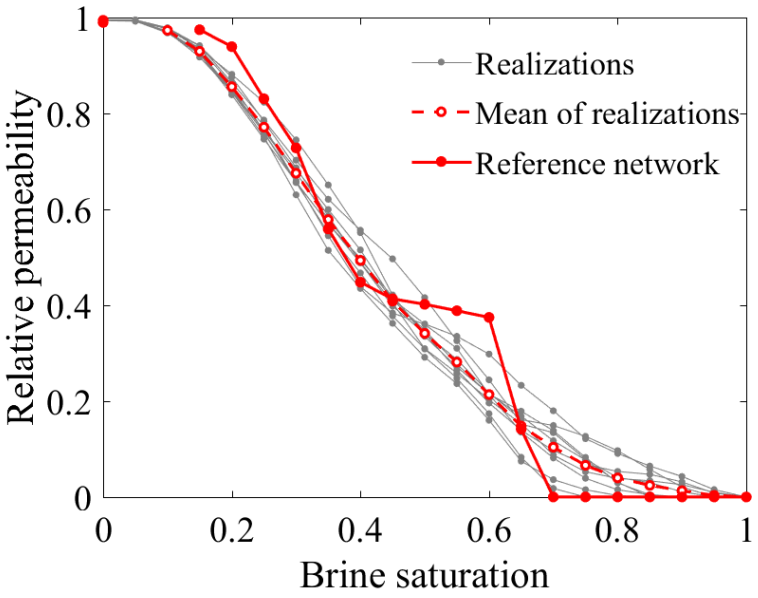

Figure A.24: Comparison of CO_2 relative permeability of 10 realizations of stitched pore-networks from sample **C2** via volumetric stitching with their reference pore-network.

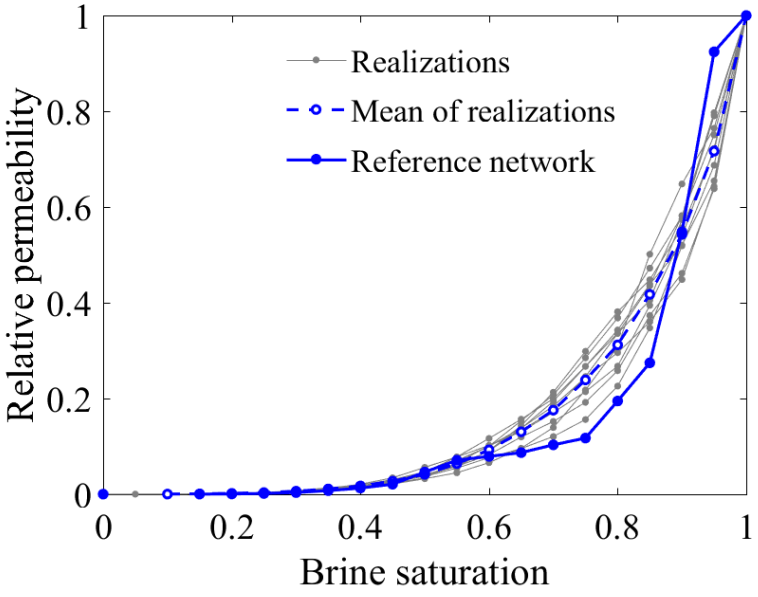

Figure A.25: Comparison of brine relative permeability of 10 realizations of stitched pore-networks from sample **C2** via volumetric stitching with their reference pore-network.

Appendix B

Sensitivity analysis

Sensitivity analysis of parameters of lattice-Boltzmann simulations on pore-network configurations

In this appendix, sensitivity analysis of lattice resolution and capillary number of LB simulations in PN configurations studied in Chapter 4 are explored. The TPT configuration associated with pore-body filling of I_1 event with the shape factor of $G = 0.040$ is selected to investigate the effect of lattice resolution (using two resolutions) and capillary number (using three values) on the resulting threshold local capillary pressure and its corresponding parameters in the modified model which were explained in Section 4.5.1.1. In each case, the $\hat{P_{c_1}}$ of I_1 event is obtained from LB simulation, and then, f_{21} and f_{31} are computed based on Eqs. 4.12 and 4.13, respectively.

In order to investigate the effect of lattice resolution, two simulation sizes of $47\times47\times50$ and $92\times92\times105$ are chosen. Table B.1 includes the information of the two studied resolutions (low and high) for pore-body filling of I_1 event with $G = 0.040$. All values reported in the table are in lattice units. Fig. B.1 shows the two different resolutions of TPT configuration for pore-body filling of I_1 event. The radius of pore-body and pore-throat in the high resolution configuration is twice larger than the low resolution configuration. Fig. B.2 shows the LB simulation of pore-body filling during imbibition process on the high resolution configuration.

Table B.1: The information of studied resolutions for TPT configuration of pore-body filling of I_1 event with $G = 0.040$. All values are reported in lattice units.

Resolution	Simulation size	Pore-body radius	Pore-throat radius
Low	$47 \times 47 \times 50$	25	5
High	$92 \times 92 \times 105$	50	10

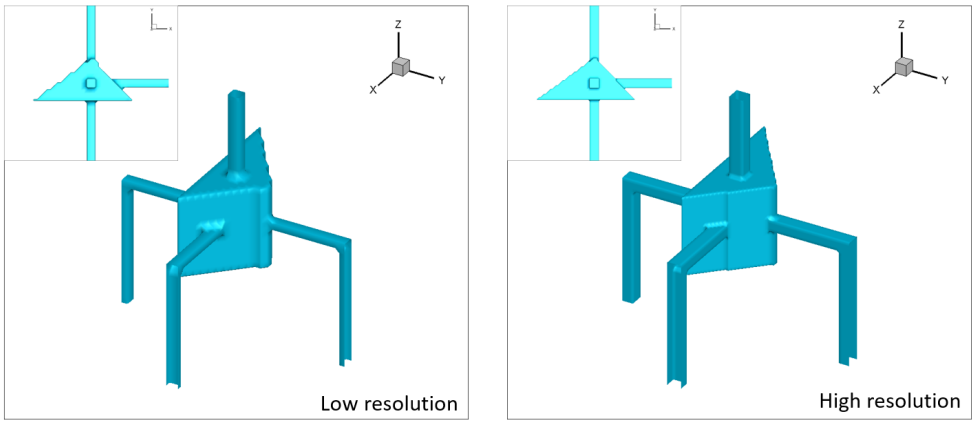

Figure B.1: The studied resolutions of TPT configuration for pore-body filling of I_1 event with $G = 0.040$: (left) low resolution configuration, (right) high resolution configuration.

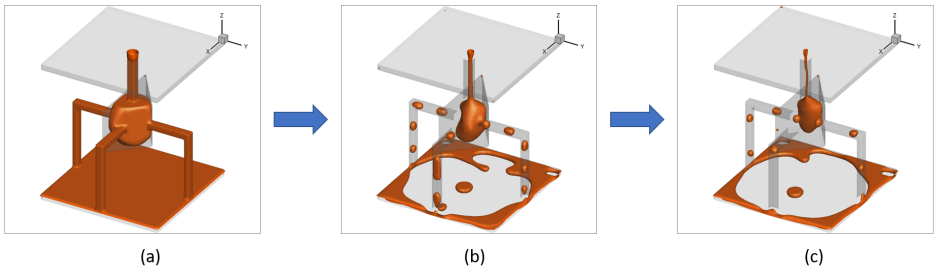

Figure B.2: Pore-body filling of I_1 event during imbibition process on a high resolution TPT configuration with $G = 0.040$: (a) beginning of imbibition (b) prior to pore-body filling (c) during pore-body filling.

The resulting filling factors of these two resolutions from LB simulation are listed in Table B.2. The difference between factors of the two resolutions is not significant which implies that the used low resolution was sufficient to simulate pore-level events with the LB model which comes with less computational costs.

Table B.2: The resulting filling factors for two studied lattice resolutions from LB simulation of pore-body filling of I_1 event with $G = 0.040$.

Shape factor	f_{21}	f_{31}
Modified (low res.)	0.694	0.428
Modified (high res.)	0.660	0.407
Conventional	0.676	0.412

In order to investigate the effect of capillary number, three values of Ca=5×10^{-5}, Ca=1×10^{-5}, and Ca=5×10^{-6} are chosen. Fig. B.3 shows the LB imbibition simulation of I_1 event during filling with the three studied capillary numbers on TPT configuration with the shape factor of $G = 0.040$.

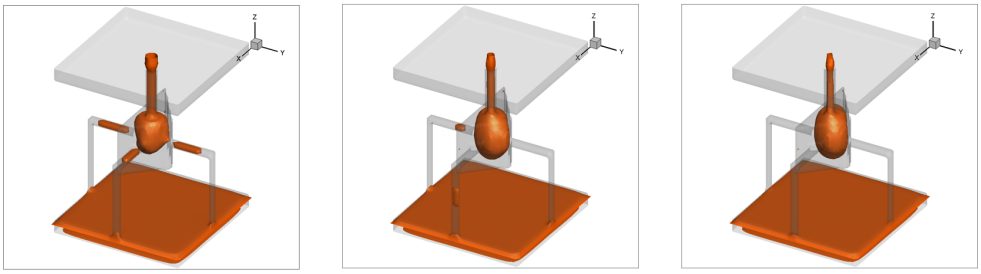

Figure B.3: Pore-body filling of I_1 event during imbibition process with different capillary numbers on TPT configuration with $G = 0.040$: (a) Ca=5×10^{-5} (b) Ca=1×10^{-5} (c) Ca=5×10^{-6}.

The resulting filling factors of these three capillary numbers from LB simulation are listed in Table B.3. While the difference between factors of Ca=1×10^{-5} and Ca=5×10^{-6} is negligible, they are slightly different from the factors of Ca=5×10^{-5} (used in Chapter 4). This implies that a lower capillary number is a safer choice to model a CO_2-brine flow which is a highly capillary-dominated flow system. It also shows that a very low capillary number is not necessarily needed to obtain an acceptable accuracy since the factors from Ca=1×10^{-5} and Ca=5×10^{-6} are very close. Thus, one should

choose an optimal capillary number to reduce computational costs while it is able to result an acceptable accuracy. Among the three studied capillary numbers, Ca=1×10^{-5} is the optimal capillary number to apply on other configurations and shape factors.

Table B.3: The resulting filling factors for three different capillary numbers from LB simulation of pore-body filling of I_1 event with $G = 0.040$.

Shape factor	f_{21}	f_{31}
Modified (Ca=5×10^{-5})	0.694	0.428
Modified (Ca=1×10^{-5})	0.632	0.390
Modified (Ca=5×10^{-6})	0.626	0.386
Conventional	0.676	0.412